Numerical Modelling of Multi-Phase Multi-Component Reactive Transport in the Earth's interior

Beñat Oliveira[1], Juan Carlos Afonso[1], Sergio Zlotnik[2], Pedro Diez[2],

[1] *Australian Research Council Centre of Excellence for Core to Crust Fluid Systems/GEMOC, Department of Earth and Planetary*

Macquarie University, Sydney, Australia

[2] *Laboratori de Càlcul Numèric, Escola Tècnica Superior d'Enginyers de Camins, Canals i Ports, Universitat Politècnica de Catal*

SUMMARY

We present a conceptual and numerical approach to model processes in the Earth's interior that involve multiple phases that simultaneously interact thermally, mechanically and chemically. The approach is truly multiphase in the sense that each dynamic phase is explicitly modelled with an individual set of mass, momentum, energy and chemical mass balance equations coupled via interfacial interaction terms. It is also truly multi-component in the sense that the compositions of the system and its constituent phases are expressed by a full set of fundamental chemical components (e.g. SiO_2, Al_2O_3, MgO, etc) rather than proxies. These chemical components evolve, react with, and partition into, different phases according to an internally-consistent thermodynamic model. We combine concepts from Ensemble Averaging and Classical Irreversible Thermodynamics to obtain sets of macroscopic balance equations that describe the evolution of systems governed by multi-phase multi-component reactive transport (MPMCRT). Equilibrium mineral assemblages, their compositions and physical properties, and closure relations for the balance equations are obtained via a "dynamic" Gibbs free-energy minimization procedure (i.e. minimizations are performed on-the-fly as needed by the simulation). Surface tension and surface energy contributions to the dynamics and energetics of the system are taken into

account. We show how complex rheologies, i.e. visco-elasto-plastic, and/or different interfacial models can be incorporated into our MPMCRT ensemble-averaged formulation. The resulting model provides a reliable platform to study the dynamics and non-linear feedbacks of MPMCRT systems of different nature and scales, as well as to make realistic comparisons with both geophysical and geochemical data sets. Several numerical examples are presented to illustrate the benefits and limitations of the model.

Key words: Multi-Phase – Multi-Component – Reactive Transport – Thermodynamics.

1 INTRODUCTION

1.1 General considerations and background

When considering geological processes, Multi-Phase Multi-Component Reactive Transport (MPMCRT), where different chemical species interact with different phases in complex ways, are the rule rather than the exception. As such, MPMCRT controls a number of important geodynamic and geochemical phenomena, such as melt generation and migration, rock metasomatism, rheological weakening, magmatic differentiation, ore emplacement and fractionation of chemical elements, to name a few. Given its fundamental importance, there has always been a strong motivation and interest for investigating the governing equations of MCMPRT, their mathematical structure and properties, and the numerical techniques necessary to obtain reliable solutions. However, due to the inherent complexity of MPMCRT, progress towards the understanding and modelling of such processes within the solid Earth community has been naturally slow and incremental.

The pioneering works were based on simple continuum formulations of two-phase viscous flow with incompressible phases (e.g. Frank, 1968; Sleep, 1974). Although these formulations start with a formal consideration of the microscopic conservation equations for each phase separately, further simplifications in regards to the mixture properties resulted in models that are akin to the so-called mixture models in the engineering literature (Ishii, 1975; Bowen, 1976; Gidaspow, 1994; Jakobsen, 2014). Thus, the resulting system of equations does not differ significantly in form from what is used in single phase systems (typically written as a system of either three or four governing equations), except for the implicit or explicit consideration of interfacial terms (see below). In this case, additional phasic balance equations need to be postulated to account for the different (relative) dynamics and energetics of the phases, as typically only one set of primitive variables (e.g. mixture or matrix velocity) is obtained from the balance equations. In this context, the most common assumptions in geodynamics are to neglect relative temperature differences (i.e. phases are in thermal equilibrium) and to assume

that the velocity difference between solid and melt is given by a Darcy's-type law (e.g. McKenzie, 1984; Scott & Stevenson, 1986; Spiegelman, 1993a,c; Iwamori, 1993; Fowler, 1985). The validity of such assumptions will be discussed later, but we mention here that they strictly imply slow percolation of small amounts of melt through a viscous, load-bearing deformable matrix. These type of models represent the work-horse of two-phase matrix-melt dynamics and have been extensively applied to study the behaviour of magma transport within the Earth's mantle (e.g. McKenzie, 1984; Scott & Stevenson, 1986; Spiegelman, 1993a,c; Iwamori, 1993; Aharonov et al., 1995; Spiegelman et al., 2001; Kelemen et al., 1997; Rabinowicz & Vigneresse, 2004; Elliott & Spiegelman, 2003, among many others). Later studies incorporated additional phenomena such as surface tension and damage (e.g. Bercovici et al., 2001; Bercovici & Ricard, 2003; Takei & Hier-Majumder, 2009), the energetics of the system (e.g. Šrámek et al., 2007; Katz, 2008; Rudge et al., 2011; Regenauer-Lieb et al., 2015), complex rheologies (e.g. Keller et al., 2013; Katz et al., 2006; Peters et al., 2015; Connolly & Podladchikov, 2007), reactive flow (e.g. Steefel et al., 2005; Mayer et al., 2002; Hesse et al., 2011; Schiemenz et al., 2011) and chemical transport (Spiegelman & Elliott, 1993; Elliott & Spiegelman, 2003; Keller & Katz, 2016), although the last two typically in a simple parameterized way. These advances add considerable complexity to the numerical modelling of multi-phase physics, yet impose additional rigor to the theoretical modelling of the Earth interior.

An alternative to mixture-type models is the so-called true multi-phase flow model or multi-fluid model (the most popular variant is the two-phase flow model, c.f. Ishii (1975); Jakobsen (2014)). In this approach, the final model is formulated by considering the different phases, and their respective conservation equations, separately and before the application of a formal averaging procedure. Thus, the final model consists of as many sets of conservation equations as phases in the multi-phase system, which makes this approach significantly more involved than the mixture approach. Moreover, since the averaged properties of each phase cannot be independent of each other, a number of interaction terms (accounting for the mechanical, chemical and energy interactions between phases) appear now explicitly in the formulation. On the upside, the multi-phase flow approach is considered more fundamental, as it allows for more general formulations (e.g. non-equilibrium interactions, different governing equations for different phases), it provides explicit and formal relations between the mixture properties and those of the local constituent phases, and offers a more consistent description of the interaction between phases (Ishii, 1975; Drew & Passman, 1999; Hassanizadeh & Gray, 1979a, 1993; Jakobsen, 2014). At least in principle, this is true. In practice, however, the choice of truly multi-phase models over simpler mixture-type models depends on the actual nature of the multi-phase problem, the goals of the simulation, and the amount of information available to model the interaction terms. It is well-known that when the dynamics of the phases are strongly coupled (i.e. phases

are always close to mechanical and thermal equilibrium), as commonly assumed in most geodynamic studies, mixture-type models are adequate. However, the range of applicability and/or reliability of such approaches can be rather limited, leaving a large number of important geological scenarios out of scope (e.g. creation of magmatic chambers, fast magma migration, dynamics of volcanic eruptions, out-of-equilibrium processes, etc).

Considering the current "big-data" and "data-assimilation" trends in Earth sciences, as well as the wide range of scales and feedback mechanisms involved in geological phenomena, we believe that next-generation numerical models of MPMCRT should be based on (at least) two main ingredients: 1) a general and scalable multi-phase approach valid over a wide spectrum of scales and problems coupled with 2) a sound chemical thermodynamic framework for the reactive and chemical transport problems. While the incorporation of reactions/phase changes and tracking of chemical species into a multi-phase model adds considerable complexity, it is strictly necessary for obtaining a meaningful coupling between mechanical and geochemical phenomena and therefore to achieve the final goal of a more complete understanding of the feedbacks between thermal, mechanical, and chemical processes in the Earth.

The above two ingredients would provide a reliable platform that can be used not only to study the dynamics and feedbacks of multi-phase systems of different nature and scales (the predictive forward problem) but also the possibility of making realistic comparisons with both geophysical and geochemical data sets. The latter is needed if we are to take advantage of geochemical and geophysical data-assimilation techniques and formal inverse methods to constrain, interpret and/or calibrate the results of MPMCRT simulations. In this context, only few studies within the geodynamic community have made progress towards a consistent coupling of the above two ingredients into a single numerical framework. In a seminal paper, Tirone et al. (2009) used a multi-phase dynamic model in conjunction with an equilibrium thermodynamic model to couple the dynamics of the system with the physical properties of the (dynamically evolving) mineral assemblages and melt in a thermodynamically-consistent manner. Tirone et al. (2009) thus used, for the first time to our knowledge, the so-called "dynamic-approach" of incorporating equilibrium thermodynamic information into a thermomechanical simulation of two-phase flow. This approach involves solving energy minimization problems "on the fly" as required by the local flow conditions (e.g. T, P, composition) under the assumption of local equilibrium. Although the advantages of the dynamic approach are many in terms of generality, thermodynamic-mechanical consistency and the richness of the information available, the need for solving a large number of minimizations at each time step of the simulation has rendered it unpopular. By contrast, the "static" approach retrieves the physical properties of the phases from precalculated tables (typically stored in memory during the simulation) obtained by prior energy

minimization computations. Examples of the latter within the context of single-phase simulations are abundant (e.g. Afonso et al., 2008; Sobolev et al., 2006; Babeyko & Sobolev, 2008; Liu et al., 2011, 2014; Chen & Gerya, 2016); examples in two-phase flow simulations are Dufek & Bachmann (2010) and Karakas & Dufek (2015). An even more popular approach involves had hoc empirically-calibrated parameterizations, which despite lacking generality and/or thermodynamic consistency, are extremely computationally efficient and circumvent the need for energy minimization computations altogether (e.g. Katz, 2008; Rudge et al., 2011; Weatherley & Katz, 2012; Keller & Katz, 2016).

The present work is an initial attempt to outline the basic conceptual and numerical frameworks of a general MPMCRT approach and some of the ways in which equilibrium and non-equilibrium chemical thermodynamics can be used in conjunction with a true multi-phase approach to model a wide variety of problems in Earth sciences. In contrast to past approaches, ours is ultimately based on the effective and accurate tracking of the system's chemical components and internal energy in a full visco-elasto-plastic formulation. With this information, the chemical thermodynamics component allows us to obtain both local equilibrium and/or non-equilibrium assemblages (i.e. thermodynamic phases and their compositions) and their relevant physical properties (e.g. density, seismic velocities, heat capacities, etc) everywhere in the system. These properties in turn are used in the solution of the governing balance equations, and therefore the mechanical and chemical problems are tightly coupled and thermodynamically consistent. We will also demonstrate that a judicious combination of the dynamic and static coupling approaches, based on phase equilibria computations, is not only desirable, but computationally efficient (see also Afonso et al., 2015).

1.2 Definitions

We begin by briefly describing some important thermodynamic and mechanical terms used throughout this work:

- A *thermodynamic phase* is defined as a homogenous body of matter having distinct physical properties, composition, and boundaries (e.g. a mineral grain); therefore it is in principle mechanically separable from adjacent phases.
- A *thermodynamic system* is any aggregate of thermodynamic phases, separated from the rest of the universe by actual or imaginary boundaries; the system is called homogeneous if composed of only one phase and heterogeneous if composed of multiple phases.
- *System components* are the minimum set of chemical formulae necessary (and arbitrarily chosen) to describe the total chemical composition of the thermodynamic system. They need to 1) be linearly independent and 2) span the entire compositional range of the system under study. The term "multi-component" in our MPMCRT formalism refers to these components. System components may or may

not exist as real chemical entities that can be observed in nature (e.g. molecules, ions, etc). The latter are referred to as *chemical species*. For instance, we typically represent the composition of a rock (our system) in terms of oxides (e.g. SiO_2, MgO, FeO, etc), but we do not imply that the rock is made up of of such oxides. Chemical species are denoted using superindex b.

- *Phase components* or *solution components* (also known as *solution end-members*) are chemical formulae specific to a thermodynamic phase, used to describe the compositional range allowed in that phase. They need to 1) be linearly independent, 2) represent a minimum set, and 3) preserve the structural integrity of the thermodynamic phase. For instance, while SiO_2, MgO and FeO can be used as system components when working with olivine (Mg_2SiO_4-Fe_2SiO_4) and orthopyroxene ($MgSiO_3$-$FeSiO_3$) solid solutions, they cannot be used as phase components, as they cannot be varied independently while preserving the structural integrity of the phases. In this case, a valid set of phase components is Mg_2SiO_4-Fe_2SiO_4-$MgSiO_3$-$FeSiO_3$.

- A *dynamic phase* is defined as a macroscopic unit of mass, composed of one or more thermodynamic phases, with a distinct dynamic behaviour (significantly different from other dynamic phases in the same system) and clear boundaries that separate it form its surroundings. The dynamic behaviour of each dynamic phase is therefore controlled by a separate (and potentially different) set of conservation equations. Dynamic phases are the fundamental entities considered in multi-phase modelling approaches. For instance, the percolating melt and the solid porous matrix in a segregation problem (1-A) are considered distinct dynamic phases. Lithologies with significantly different physical properties could be also considered different dynamic phases under some circumstances. Dynamic phases are denoted throughout the text by subindexes k, j, or l.

- A true *multi-phase* approach is here understood as any formalism based on the principles of continuum mechanics where the dynamic behaviour of the dynamic phases or system of dynamic phases are modelled with the explicit consideration of interfacial transport phenomena.

2 ENSEMBLE-AVERAGED MPMCRT PHYSICAL MODEL

In this section, the general governing equations for each dynamic phase k are derived applying the ensemble averaging technique (e.g. Drew, 1971, 1983; Hill, 1998; Drew & Passman, 1999) to the fundamental microscopic conservation equations. While most of the final equations obtained here are either similar or identical to those discussed in previous studies (e.g. McKenzie, 1984; Spiegelman, 1993a,c; Bercovici et al., 2001; Bercovici & Ricard, 2003; Šrámek et al., 2007; Tirone et al., 2009), some are new or significantly different. The averaging technique is also not-standard in the geophysical literature. Therefore, for clarity and completeness, in what follows we provide a detailed derivation

Table 1. Main variables used in this work

Variable	Description	Units	Variable	Description	Units
$\mathbf{b}$	body force	m s^{-2}	$\mathbf{v}^b$	velocity of oxide b	m s^{-1}
C	heat capacity	J Kg^{-1} K^{-1}	$\check{\mathbf{v}}$	composition-weighted velocity	m s^{-1}
c^b	oxide amount (weight percent)	[-]	$\mathbf{W}$	vorticity tensor	s^{-1}
$c_{k,j}$	viscous interaction coefficient	Pa s m^{-2}	$\mathbf{x}$	space variable	m
$\mathcal{D}$	fluctuating energy dissipation	J m^{-3} s^{-1}	α	interfacial area density	m^{-1}
$E_{k,j}$	interface energy-transfer rate	J m^{-3} s^{-1}	Γ^b	interface chemical mass-transfer rate	Kg m^{-3} s^{-1}
G	shear elastic modulus	Pa	Γ^m	interface mass-transfer rate	Kg m^{-3} s^{-1}
G	gibbs-free energy	J	$\dot{\boldsymbol{\varepsilon}}$	strain-rate tensor	s^{-1}
$\mathbf{g}$	gravitational acceleration	m s^{-2}	$\Theta_{k,j}$	surface tension hold by k and j	Pa
H_{pc}	molar enthalpy	J mol^{-1}	κ	interfacial curvature	m^{-1}
$\mathbf{Id}$	identity matrix	[-]	μ	shear viscosity	Pa s
K	bulk elastic modulus	Pa	μ_{pc}	chemical potential	J mol^{-1}
$\mathbf{M}$	interface momentum-transfer rate	Pa m^{-1}	ξ	bulk viscosity	Pa s
$\mathbf{m}_i$	total surface tension force	Pa m^{-1}	ξ_i	surface energy	Pa m
$\mathbf{n}_{k,j}$	unit vector normal to $S_{k,j}$	[-]	π	realization	[-]
P	mechanic pressure	Pa	ρ	density	Kg m^{-3}
$\mathcal{P}$	thermodynamic pressure	Pa	σ	surface tension coefficient	Pa m
$\mathbf{q}$	diffusive flux	J m^{-2} s^{-1}	$\boldsymbol{\sigma}$	stress tensor	Pa
Q	heat source	J m^{-3} s^{-1}	$\boldsymbol{\tau}$	deviatoric stress tensor	Pa
S_{pc}	molar entropy	J K^{-1} mol^{-1}	ϕ	average phase fraction	[-]
$S_{k,j}$	interface between k and j	[-]	Φ	general property	[-]
t	time	s	χ_k	characteristic function	[-]
T	temperature	K	$\chi_k^{\boldsymbol{\tau}}$	elastic shear stress evolution parameter	[-]
u	internal energy	J Kg^{-1}	$\chi_{k,j}^{P}$	elastic volumetric stress evolution parameter	[-]
$\mathbf{v}$	velocity	m s^{-1}	ω	surface energy partition coefficient	[-]

Indexes		Operators	
k, j, l	dynamic phases	$\frac{\partial}{\partial t}$	local time derivative
ω	ω-weighted interface property	$\frac{\mathrm{D}}{\mathrm{D}t}$	material time derivative
i	interface	$\hat{()}$	objective time derivative
b	chemical species, oxides	$()^{\circ}$	spherical component
pc	phase component	$()^{'}$	deviatoric component
v	viscous	$\overline{()}$	average mixture property
e	elastic	$\Delta()_{k,j}$	difference between k and j, $()_k - ()_j$
y	yielding	$\langle\rangle$	ensemble averaging operator

Miscellaneous	
$\sum_k ()_k$	sum over all existing dynamic phases
$\sum_{z\neq k} ()_{k,z}$	sum of a given interfacial property over all interfaces delimiting dynamic phase k. E.g. $\sum_{z\neq k} \Gamma^m_{k,z} = \Gamma^m_{k,j} + \Gamma^m_{k,l}$
$\sum_k \sum_{z>k} ()_{k,z}$	sum of a given interfacial property over all the existing interfaces. E.g. $\sum_{z\neq k} S_{k,z} = S_{k,j} + S_{j,l} + S_{l,k}$

the fundamental MPMCRT set of averaged equations. List of the variables used in this study is given in Table 1.

2.1 Ensemble averaging

In theory, the dynamics of MPMCRT could be studied by solving the local (microscopic) conservation equations (e.g. mass, momentum, energy) in each dynamic phase, provided that the exact location of the interfaces is known and accounted for. This approach forms the core of some small-scale engineering and geoscience applications (e.g. Scardovelli & Zaleski, 1999; Jessell et al., 2001; Jing, 2003; Kang et al., 2006). For the case of MPMCRT in the Earth, however, it is neither desirable nor possible to work with such a detailed description of the system (as the ones shown in Fig. 1-A left panel) at most scales of geodynamic interest. A more practical and widely used approach applies formal averaging formalisms to the phase-dependent conservation equations to obtain a macroscopic description of the multi-phase flow without the explicit tracking of interfacial discontinuities/structure. The purpose of averaging is therefore to replace a deterministic, exact (but complex) multi-boundary problem with a more tractable macroscopic one valid at coarser spatial and temporal scales (c.f. Drew, 1971, 1983; Ishii, 1975; Ishii & Hibiki, 2006) Consequently, the attention is shifted towards the average behaviour, structure and properties of the multi-phase flow, such as average melt content, average phase flux, and average chemical composition of each dynamic phase. The latter are therefore treated as independent continuum media that can, in theory, occupy the same region in space. Dynamic phases are, thus, modelled with their own averaged macroscopic set of equations (accounting for the amount of phase present in the region), but explicitly considering interfacial phenomena.

We use *ensemble averaging* as the basis of our MPMCRT model (Drew, 1971, 1983; Drew & Passman, 1999). This averaging method, which stems from statistical mechanics, is rapidly becoming the preferred option in engineering and physics applications as it provides some significant advantages over other existing averaging strategies. For instance, contrary to time and/or volume averaging, ensemble averaging does not require the existence or explicit consideration of a control volume or averaging time span that dictates the applicability of the averaged equations (Drew & Passman, 1999; Ishii & Hibiki, 2006). Moreover, it is readily applicable to a wide range of spatial scales, i.e. a small-scale late metasomatic fluid formation and migration along grain boundaries or a meso-scale melt migration problem as shown in Fig. 1. It can also be shown that volume and time averages are special cases of ensemble averaging (e.g. Drew & Passman, 1999), and therefore the latter is considered more fundamental.

In simple terms, ensemble averaging is based on the probability of the multi-phase flow being in a particular configuration or state at a given time. Therefore, an elementary concept of ensemble averaging involves simply adding many observed flow configurations/realizations and dividing by the number of observations. This large set of realizations is referred to as the ensemble. Each of the realizations will be different within a range of variability that we can observe, but all sets/ensembles based on these realizations will be identical in an average sense. Alternatively, perhaps a more practical

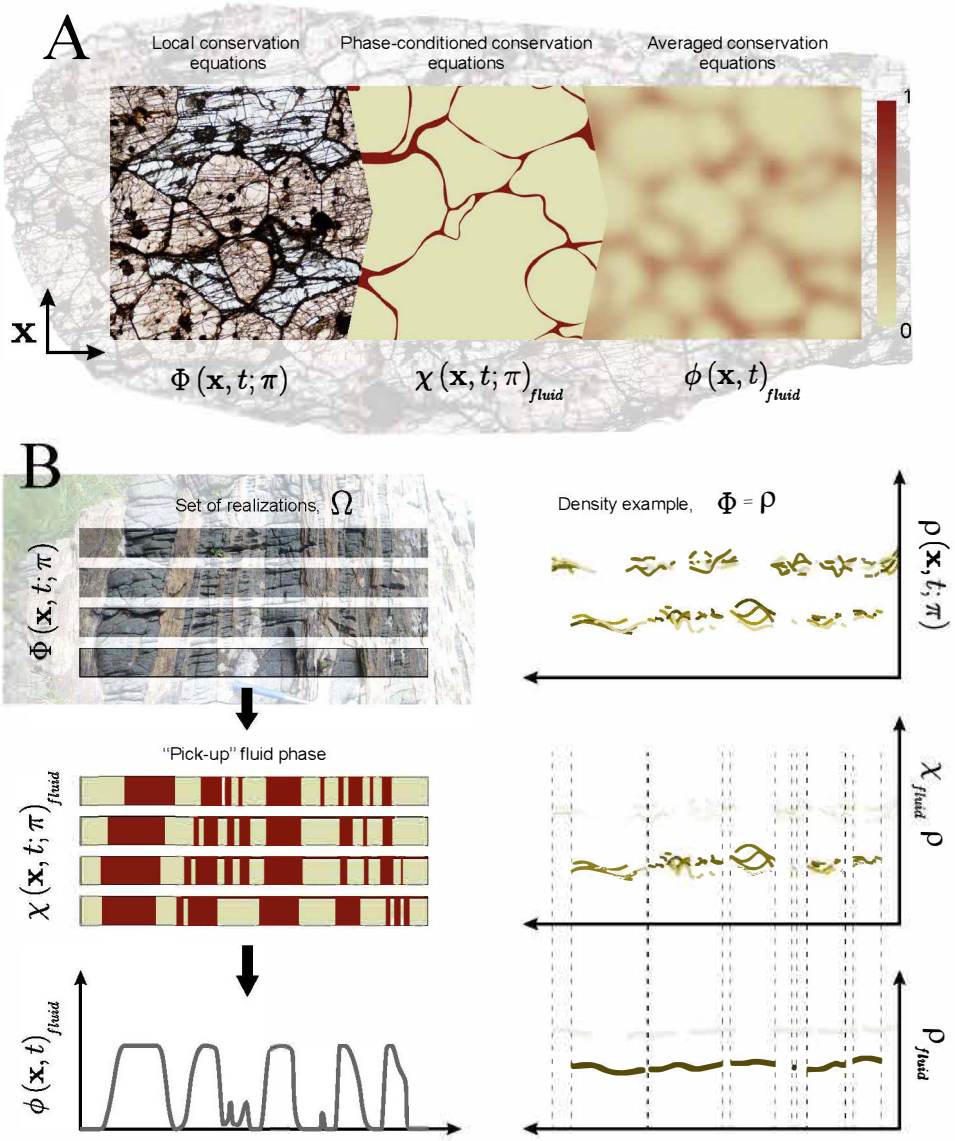

Figure 1. (Caption next page.)

conceptualization is assuming that the flow is deterministic, but a certain degree of randomness arises due to uncertainties e.g. in the initial conditions, physical parameters, phase location, or turbulence in the flow (Saffman, 1971; Lundgren, 1972; Drew, 1983; Jakobsen, 2014). In any case, the ensemble-averaged equations can be thought of providing the "expected" value, in a formal statistical sense, of the property of interest. Depending on whether discrete or continuous probabilities are used for the realizations, the ensemble average of a generic scalar, vectorial or tensorial quantity Φ can be defined either as,

Figure 1. (Previous page.) Two schematic illustrations of ensemble averaging. A) Different ensemble averaging stages over a single realization π (thin section) concerning a well equilibrated mantle eclogite (garnet + clinopyroxene) with triple point ($\sim 120^o$) grain boundaries. Note that the three different stages are represented on the same thin section, thus same realization π and time t, but on different spatial coordinates along the thin section. The presence of recrystallized amphibole along grain boundaries in the left panel suggests percolation of a late metasomatic fluid. Here, properties of the system, Φ, as well as local conservation equations, are defined over the entire domain. The characteristic function of the metasomatic fluid, χ_{fluid}, is depicted in the central panel where $\chi_{fluid} = 1$ indicates the region containing the fluid phase. If the local conservation equations valid in the entire domain are multiplied by χ_{fluid} (i.e. first step in the text), we obtain the phase-conditioned balance equations. In other words, these equations are only defined in the highlighted region and for the particular realization π. The third panel represents the averaged fluid fraction field, ϕ_{fluid}, that we would obtain after ensemble averaging a large number of similar realizations. B) Similar to A) for a field outcrop where the presence of melt is inferred from the assemblage of pyroxenites and dunites (modified from Tilhac et al., 2016). Left panels represent, from top to bottom, i) four 1D profiles illustrating a possible set of realizations (the ensemble over which averaging procedures are applied), ii) the characteristic function picking up the fluid phase (pyroxenite), iii) and the corresponding averaged fluid fraction field, ϕ_{fluid}. Right panels illustrate the procedure to obtain the averaged fluid density field. First, actual densities from the four realizations are collected in the top panel, where the density difference between the fluid and solid phases is apparent. Second, the fluid density is "picked out" at every realization, $\chi_{fluid}\rho$, in the central panel. Finally, ensemble averaging is applied and a single averaged fluid density field, ρ_{fluid}, is obtained in the bottom panel (ρ_{solid} is also shown for reference).

$$\langle \Phi \rangle (\mathbf{x}, t) = \langle \Phi (\mathbf{x}, t; \pi) \rangle = \lim_{\pi \to \infty} \frac{1}{\pi} \sum_{\pi} \Phi (\mathbf{x}, t; \pi) \tag{1}$$

or

$$\langle \Phi \rangle (\mathbf{x}, t) = \langle \Phi (\mathbf{x}, t; \pi) \rangle = \int_{\Omega} \Phi (\mathbf{x}, t; \pi)\, p(\pi) d\pi = \int_{\Omega} \Phi (\mathbf{x}, t; \pi)\, dm(\pi) \tag{2}$$

where the ensemble averaging is denoted by $\langle \circ \rangle$, a single realization by π, $\mathbf{x}$ and t are the usual space and time variables, and $p(\pi)\ d\pi = dm(\pi)$ is the probability that the flow configuration is between π and π+$d\pi$ on the set of all possible realizations Ω. With these definitions, $p(\pi)$ is a true probability density function satisfying

$$\int_{\Omega} p(\pi) d\pi = 1 \tag{3}$$

The reader is referred to Drew & Passman (1999) for thorough discussions on the properties and fundamentals of ensemble averaging.

2.1.1 Phase or characteristic function

Applying the averaging operator directly to the conservation equations of each phase results in some mathematical difficulties (related to the discontinuities in the fields associated with phase boundaries, (Drew & Passman, 1999; Jakobsen, 2014) that can be avoided by introducing a *phase* or *characteristic function*, $\chi_k(\mathbf{x}, t; \pi)$, defined as

$$\chi_k = \begin{cases} 1 & \text{if } \mathbf{x} \in k \text{ in realization } \pi, \\ 0 & \text{otherwise} \end{cases} \tag{4}$$

This function is mathematically expressed in terms of a Heaviside step function and therefore it plays the role of "picking out" phase k from the multi-phase mixture while ignoring other phases and interfaces. This is illustrated in Fig. 1-A (central) and -B (left-central) panels, where the fluid phase (inferred from the residual lithologies) for both (A) a single and (B) several realizations, are highlighted with $\chi_{fluid} = 1$. The important point is that the phase function is assigned the properties of a generalized function, which is especially useful when dealing with discontinuous functions and their differentiation within integrals (Drew, 1983; Jakobsen, 2014) In particular, using the properties of generalized functions, it can be shown that χ_k evolves according to the so-called topology equation

$$\frac{\partial \chi_k}{\partial t} + \mathbf{v}_i \cdot \nabla \chi_k = 0 \tag{5}$$

where $\mathbf{v}_i$ is the velocity of the interface (Drew, 1983; Jakobsen, 2014).

2.1.2 Averaged properties

General properties, Φ, may be discontinuous over single realizations concerning multiple phases as shown in Fig.1-B (top-right). With definition (A.2), the product $\chi_k \Phi$ represents the isolated or "picked" phase property (in this case, Φ) of a single realization of the multi-phase flow. This is schematically shown in Fig.1-A (middle) and B (middle-left) for $\Phi = 1$ and in Fig.1-B (middle-right) for Φ=ρ. Once Φ is isolated from its surroundings on the set of all possible realizations Ω, we can apply the ensemble average operator to it in order to obtain an average description of Φ inside a given dynamic phase k

$$\langle \chi_k \Phi \rangle = \lim_{\pi \to \infty} \frac{1}{\pi} \sum_{\pi} \chi_k \Phi \tag{6}$$

as illustrated in Fig. 1-A (right) and -B (bottom panels). Since χ_k is zero everywhere but in regions where phase k exists, we can rewrite the sum in Eq. (A.4) in terms of realizations where only phase k is present (denoted by π_k),

$$
\begin{aligned}
\langle \chi_k \Phi \rangle &= \lim_{\pi \to \infty} \frac{1}{\pi} \sum_{\pi_k} \Phi \\
&= \lim_{\pi \to \infty} \frac{\pi_k}{\pi} \frac{1}{\pi_k} \sum_{\pi_k} \Phi \\
&= \phi_k \lim_{\pi_k \to \infty} \frac{1}{\pi_k} \sum_{\pi_k} \Phi \\
&= \phi_k \Phi_k
\end{aligned}
\tag{7}
$$

where, $\phi_k = \langle \chi_k \rangle$ is the average phase fraction

$\Phi_k = \lim_{\pi_k \to \infty} \frac{1}{\pi_k} \sum_{\pi_k} \Phi$ is the intrinsic or phase-weighted average

The intrinsic or phase-weighted average $\Phi_k = \frac{\langle \chi_k \Phi \rangle}{\phi_k}$ defines "true" phase averaged quantities of any property Φ. A graphical representation of both the average phase fraction and the intrinsic average is given in Fig. 1-B bottom panels. Taking the example $\Phi = \rho$ (bottom-left panel), the intrinsic phase average of the density refers to the ensemble-averaged density of the phase and it exists wherever the phase has been observed (region delimited with dashed lines), regardless of whether the phase coexists with other phases (multi-phase region) or not. In the region where ϕ_k is neither one nor zero (coexisting phases), the average $\langle \chi_k \Phi \rangle$ = $\phi_k \Phi_k$ is the weighted density (perhaps it is easier to think of the equivalent weighted mass), according to its ensemble average amount ϕ_k, assigned to the continuum and thus used in the conservation equations.

According to Eq. (A.5), the average phase fraction, ϕ_k, is the ensemble average of the characteristic function itself,

$$
\langle \chi_k \rangle = \lim_{\pi \to \infty} \frac{1}{\pi} \sum_{\pi} \chi_k = \lim_{\pi \to \infty} \frac{\pi_k}{\pi} = \phi_k \tag{8}
$$

since χ_k is zero everywhere but in regions where phase k exists. From Eq. (8) it is clear that $\sum_k \phi_k = 1$. In other words, the ensemble average of the characteristic function χ_k is the number of realizations where phase k is present, π_k, divided by the total number of realizations (i.e. average occurrence). It has become customary to treat ϕ_k as equivalent to the local volume fraction of phase k from volume averaging. Although this can be shown to be true for spatially homogeneous, non-fluctuating, flows (as in our case), it is perhaps better to think of ϕ_k in terms of the meaning assigned by ensemble averaging: it is the *expected* value of the ratio of volume of phase k to the total volume, in the limit when volume tends to zero. Alternatively, it can also be viewed as the *probability* that a particular phase is present at a particular point in space and time. In two-phase studies within the geodynamics community, ϕ is commonly assumed equal to porosity. Here, we will refer to ϕ_k as the "average phase fraction" and generalize this definition to incorporate multiple dynamic phases into our formulation.

More details on the nature of the characteristic function and ensemble averaging relations are given in Appendix A.

2.1.3 Averaged conservation equations

With the aid of χ_k and $\langle\circ\rangle$, and following a similar procedure to that introduced in Fig. 1, any ensemble-averaged conservation equation for any dynamic phase k can be derived following two simple steps. First, the individual conservation equations valid in phase k are multiplied by χ_k in order to isolate the individual phase contribution to the multi-phase assemblage. We refer to the resulting conservation equations as the phase-conditioned conservation equations. Contributions to the phase-conditioned conservation equations for the fluid phase come only from regions containing the fluid, since the rest of the domain is multiplied by $\chi_{fluid} = 0$ (1-A central panel).

The second step is the actual application of the averaging operator to the phase-conditioned conservation equations. Since in essence the ensemble average is the generalization of adding the values of a given phenomenon for each realization and dividing it by the number of observations, the averaged conservation equations for each dynamic phase, k, are obtained by ensemble averaging a large set of phase-conditioned local conservation equations.

The set of averaged equations obtained after applying the above two steps is rigorous, but not solvable, as it contains averages of products of the independent variables. In order to overcome this problem, the averages of products are related to products of averaged variables. This is typically achieved by making use of either phase or mass-weighted averaged variables, as shown in the next sections (also Appendix A1).

2.2 Mass conservation

Continuum mechanics assumes that mass is absolutely continuous with respect to volume. Therefore, the Radon-Nikodym theorem proves the existence of a material property called density ρ, defined pointwise on the medium, that allows to write the local mass conservation equation as

$$\frac{\partial \rho}{\partial t} + \nabla \cdot \rho \mathbf{v} = 0 \tag{9}$$

where $\mathbf{v}$ is the velocity vector and $\frac{\partial}{\partial t}$ denotes the partial time derivative. As explained in the previous section, Eq. (9) is multiplied with χ_k in order to isolate the contribution of the dynamic phase k

$$\begin{aligned} \chi_k \frac{\partial \rho}{\partial t} + \chi_k \nabla \cdot \rho \mathbf{v} = 0 \quad \Rightarrow \quad & \frac{\partial \chi_k \rho}{\partial t} + \nabla \cdot \chi_k \rho \mathbf{v} = \rho \frac{\partial \chi_k}{\partial t} + \rho \mathbf{v} \cdot \nabla \chi_k \\ & \frac{\partial \chi_k \rho}{\partial t} + \nabla \cdot \chi_k \rho \mathbf{v} = \rho \left(\mathbf{v} - \mathbf{v}_i \right) \cdot \nabla \chi_k \end{aligned} \tag{10}$$

where $\mathbf{v}_i$ is the velocity of the interface and the topological equation in (A.3) has been used in the last step. Eq. (10) represents the phase-conditioned mass balance equation for the dynamic phase k. We now apply the ensemble average operator to Eq. (10) and obtain

$$\begin{aligned} &\langle \frac{\partial \chi_k \rho}{\partial t} \rangle + \langle \nabla \cdot \chi_k \rho \mathbf{v} \rangle = \langle \rho \left(\mathbf{v} - \mathbf{v}_i \right) \cdot \nabla \chi_k \rangle \quad \Rightarrow \\ \Rightarrow \quad &\frac{\partial \langle \chi_k \rho \rangle}{\partial t} + \nabla \cdot \langle \chi_k \rho \mathbf{v} \rangle = \langle \rho \left(\mathbf{v} - \mathbf{v}_i \right) \cdot \nabla \chi_k \rangle \end{aligned} \tag{11}$$

The right-hand side term represents the averaged interfacial mass transfer between phase k and the surrounding phases, which is exclusively non-zero on the interface between phases (see further details on interaction terms in section 2.6).

To render Eq. (11) solvable, we rewrite it in terms of average properties. This yields the final mass conservation equation for a single dynamic phase k,

$$\frac{\partial \phi_k \rho_k}{\partial t} + \nabla \cdot \left(\phi_k \rho_k \mathbf{v}_k \right) = \sum_{z \neq k} \Gamma^m_{k,z} \tag{12}$$

where,	$\phi_k = \langle \chi_k \rangle$	is the averaged phase fraction
	$\rho_k = \frac{\langle \chi_k \rho \rangle}{\phi_k}$	is the averaged phase density
	$\mathbf{v}_k = \frac{\langle \chi_k \rho \mathbf{v} \rangle}{\phi_k \rho_k}$	is the mass-weighted averaged phase velocity
	$\sum_{z \neq k} \Gamma^m_{k,z} = \langle \rho \left(\mathbf{v} - \mathbf{v}_i \right) \cdot \nabla \chi_k \rangle$	is the interfacial mass transfer rate

We note that the averaged velocity in Eq. (12) refers to a particular description of the velocity: the *mass-weighted* phase velocity. Although other average velocities are useful in analyzing different aspects of multi-phase systems (e.g. intrinsic average in Eq. (A.5)), the mass-weighted phase velocity has a dominant role when analysing the dynamics of the system. Importantly, the mass-weighted phase velocity is the direct extension of the fundamental *centre-of-mass velocity* to multi-phase averaged systems (Ishii, 1975). It is also the averaged velocity field resulting from ensemble averaging the mass and momentum equations written in terms of density, and therefore also the appropriate one for describing diffusion fluxes of chemical species. The mass-weighted velocity in Eq. (12) should then be understood as an additive set function of mass in space and time, as depicted in Fig. 2. In any case, if the dynamic phases are considered to be incompressible (thus, constant phase densities along mass trajectories), both definitions intrinsic and mass-weighted are equivalent, and $\mathbf{v}_k = \frac{\langle \chi_k \rho \mathbf{v} \rangle}{\phi_k \rho_k} = \frac{\langle \chi_k \mathbf{v} \rangle}{\phi_k}$.

For incompressible dynamic phases, Eq. (12) becomes

$$\frac{\partial \phi_k}{\partial t} + \nabla \cdot \left(\phi_k \mathbf{v}_k \right) = \frac{1}{\rho_k} \sum_{z \neq k} \Gamma^m_{k,z} \tag{13}$$

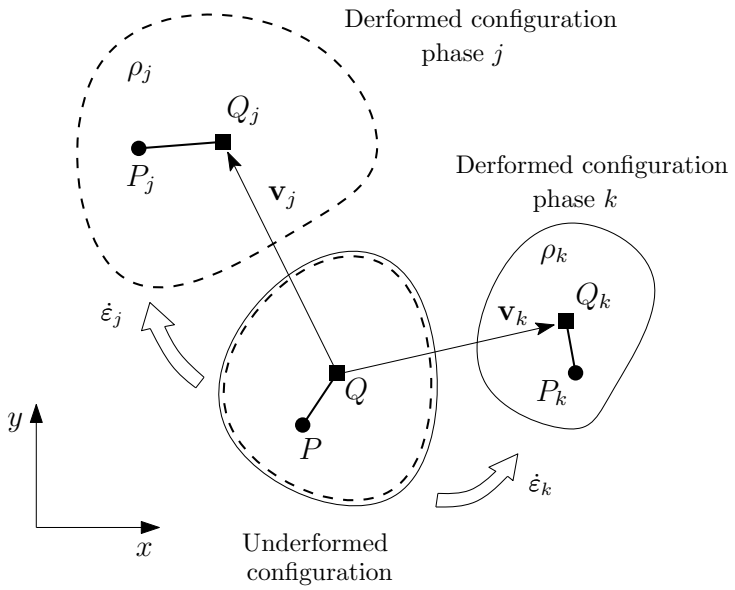

Figure 2. Deformation of a continuum made up of two dynamic phases (k and j). The boundaries of the two phases k and j are represented by solid and dashed lines respectively. The initial undeformed configuration depicts an infinitesimal control volume where the two phases coexist. Each of the phases is advected with its corresponding mass-averaged velocity and adopts a deformed configuration where Q is the barycentre and P is a reference Lagrangian point. If incompressible phases are considered, only volume changes related to phase transformations are possible and in the absence of such transformations, their true individual velocities should be solenoidal ($\nabla \cdot \mathbf{v} = 0$). However, the averaged velocity field is not divergence-free, even in the absence of phase changes (Eq. (14)). This phenomenon (also called compaction or squeezing, see C4), is due to the relative movement of the dynamic phases, which results in local variations of average phase fractions, ϕ_k, rather than the intrinsic incompressible/compressible nature of the materials. We compute deformations relative to infinitesimal volumes, where the individual strain-rate tensors for each dynamic phase are defined as a function of their respective gradients of mass-weighted velocities (see Appendix A3 for more details on the obtention of the averaged strain-rate tensor).

An overall total mass conservation equation can also be stated from Eq. (13) by summing over all phases

$$\sum_k \nabla \cdot (\phi_k \mathbf{v}_k) = \sum_k \sum_{z>k} \Gamma^m_{k,z} \left(\frac{1}{\rho_k} - \frac{1}{\rho_j} \right) \tag{14}$$

2.3 Momentum conservation

The local force-balance equation is described as,

$$\frac{\partial \rho \mathbf{v}}{\partial t} + \nabla \cdot \rho \mathbf{v}\mathbf{v} = \nabla \cdot \boldsymbol{\sigma} + \rho \mathbf{b} \tag{15}$$

where $\boldsymbol{\sigma}$ is the total stress tensor and $\mathbf{b}$ the body force term. Equation (15) describes the variation of momentum in a unit volume due to 1) advective transport of momentum across the surface (left-hand side), 2) molecular momentum flux across the surface of the volume (surface forces) and 3) body forces acting throughout the volume (right-hand side). Again, we isolate the k phase contribution and apply ensemble averaging to Eq. (15), which gives

$$\frac{\partial \langle \chi_k \rho \mathbf{v} \rangle}{\partial t} + \nabla \cdot \langle \chi_k \rho \mathbf{v}\mathbf{v} \rangle = \nabla \cdot \langle \chi_k \boldsymbol{\sigma} \rangle + \langle \chi_k \rho \mathbf{b} \rangle + \langle [\rho \mathbf{v} (\mathbf{v} - \mathbf{v}_i) - \boldsymbol{\sigma}] \cdot \nabla \chi_k \rangle \tag{16}$$

The last term in the right-hand side represents the balance of momentum across the interface and is composed of two terms: a term accounting for the momentum exchange due to inter-phase mass transfer processes (e.g. phase change) and a "mechanical" term describing the force balance at the interphase. Interfacial momentum transfer is associated with a number of effects/processes occurring in multi-phase systems such as capillarity (i.e. surface tension) and/or drag forces, among many others. More details on the nature of the interface are provided in section 2.6.

Equation (16) can be rewritten in terms of averaged variables as

$$\frac{\partial \phi_k \rho_k \mathbf{v}_k}{\partial t} + \nabla \cdot (\phi_k \rho_k \mathbf{v}_k \mathbf{v}_k) = \nabla \cdot \phi_k \left[\boldsymbol{\sigma}_k - \boldsymbol{\sigma}_k^{Re} \right] + \phi_k \rho_k \mathbf{b} + \sum_{z \neq k} \mathbf{M}_{k,z} \tag{17}$$

where,	$\mathbf{b}_k = \frac{\langle \chi_k \rho \mathbf{b} \rangle}{\phi_k \rho_k}$	is the averaged body source
	$\boldsymbol{\sigma}_k = \frac{\langle \chi_k \boldsymbol{\sigma} \rangle}{\phi_k}$	is the averaged stress tensor
	$\boldsymbol{\sigma}_k^{Re} = \frac{\langle \chi_k \rho \mathbf{v}_k'' \mathbf{v}_k'' \rangle}{\phi_k}$	is the Reynolds stress
	$\sum_{z \neq k} \mathbf{M}_{k,z} = \langle [\rho \mathbf{v} (\mathbf{v} - \mathbf{v}_i) - \boldsymbol{\sigma}] \cdot \nabla \chi_k \rangle$	is the the rate of interface momentum transfer

The expression above is rather general and can be further simplified. Except in the case of rapidly-evolving, low viscosity fluids (e.g. volatile-rich magma, pyroclasitc flows), inertia forces and Reynolds stresses can be neglected under the creeping flow approximation. We also assume that the body force is purely gravitational; therefore, $\mathbf{b} = -g\mathbf{z} = \mathbf{g}$, where g is the gravitational acceleration and $\mathbf{z}$ is the unit vector pointing upwards. In addition, the total stress tensor can be decomposed into its volumetric and deviatoric parts, $\boldsymbol{\sigma}_k = -P_k \cdot \mathbf{Id} + \boldsymbol{\tau}_k$, where $P_k = -\frac{1}{3}\text{tr}(\boldsymbol{\sigma}_k)$ is the mechanical pressure, $\mathbf{Id}$ is the identity matrix and $\boldsymbol{\tau}_k$ is the traceless deviatoric stress tensor. The relation between averaged stresses and deformation is highly problem-dependent and requires careful design. This is discussed in section 2.7, where an averaged visco-elasto-plastic rheology is developed.

Bearing these assumptions in mind, the momentum conservation equation for a single dynamic phase reads

$$\nabla\left(\phi_k P_k\right) - \nabla\cdot\left[\phi_k \boldsymbol{\tau}_k\right] = -\phi_k\rho_k\mathbf{g} + \sum_{z\neq k}\mathbf{M}_{k,z} \tag{18}$$

2.4 Energy conservation

The local internal energy conservation equation is

$$\frac{\partial \rho u}{\partial t} + \nabla\cdot\rho u\mathbf{v} = -\nabla\cdot\mathbf{q} + Q + \boldsymbol{\sigma}:\nabla\mathbf{v} \tag{19}$$

where u is the internal energy per unit mass, $\mathbf{q}$ the heat flux and Q refers to any other internal heat source (i.e. radioactive heating) per unit volume. Following the same procedure as above, we obtain ensemble-averaged equation for a single dynamic phase k

$$\frac{\partial\langle\chi_k\rho u\rangle}{\partial t} + \nabla\cdot\langle\chi_k\rho u\mathbf{v}\rangle = -\nabla\cdot\langle\chi_k\mathbf{q}\rangle + \langle\chi_k\boldsymbol{\sigma}:\nabla\mathbf{v}\rangle + \langle\chi_k Q\rangle + \langle\left[\rho u\left(\mathbf{v}-\mathbf{v}_i\right)-\mathbf{q}\right]_k\cdot\nabla\chi_k\rangle \tag{20}$$

In terms of averaged variables, Eq. (20) reads

$$\frac{\partial\phi_k\rho_k u_k}{\partial t} + \nabla\cdot\left(\phi_k u_k\rho_k\mathbf{v}_k\right) = \phi_k\boldsymbol{\sigma}_k:\nabla\mathbf{v}_k - \nabla\cdot\phi_k\left(\mathbf{q}_k + \mathbf{q}_k^{Re}\right) + \phi_k Q_k + \phi_k\mathcal{D}_k + \sum_{z\neq k}E_{k,z} \tag{21}$$

where,	$u_k = \frac{\langle\chi_k\rho u\rangle}{\phi_k\rho_k}$	is the mass-weighted averaged internal energy
	$\mathbf{q}_k = \frac{\langle\chi_k\mathbf{q}\rangle}{\phi_k}$	is the averaged energy flux
	$\mathbf{q}_k^{Re} = \frac{\langle\chi_k\rho\mathbf{v}_k''u_k''\rangle}{\phi_k}$	is the Reynolds internal energy flux
	$Q_k = \frac{\langle\chi_k Q\rangle}{\phi_k}$	is the averaged heat source
	$\mathcal{D}_k = \frac{\langle\chi_k\boldsymbol{\sigma}_k'':\nabla\mathbf{v}_k''\rangle}{\phi_k}$	is the averaged fluctuating energy dissipation
	$\sum_{z\neq k}E_{k,z} = \langle\left[\rho u\left(\mathbf{v}-\mathbf{v}_i\right)-\mathbf{q}\right]\cdot\nabla\chi_k\rangle$	is the averaged rate of interfacial energy transfer

In Eq. (21), the interface contribution is hidden in the interfacial internal energy transfer term, which is further discussed in section 2.6. The right-hand side of Eq. (21) includes the Reynolds internal energy flux and the energy dissipation due to fluctuating fields (see section A1.1). Under the slow creeping flow approximation, fluctuating velocities are presumably small and these terms can be assumed negligible in comparison to $\mathbf{q}_k$. This assumption circumvents the problem of formally defining $\mathbf{q}_k^{Re}$ and $\mathcal{D}_k$, which would require additional closure relations, thus increasing the number of unknowns and constitutive equations.

In the purposes of this work, we solve a single energy balance for the mixture rather than N energy equations for the N constitutive phases. This implicitly assumes that temperature changes in the multi-phase system are sufficiently slow for the temperature to equilibrate *locally* between the phases. If the fluid (e.g. melt) percolates at very high speeds on a coarse matrix network, this assumption will not hold. However, in the context of melt generation and migration inside the Earth, it is expected that the assumption of thermal equilibrium between dynamic phases applies. The validity of, and justification for, this commonly-used assumption in melting scenarios has been discussed, among others, by Fowler (1985) and Tirone et al. (2009). In any case, the MPMCRT formulation presented here can be readily modified to accommodate for more general conditions, as discussed later in Section 6.1.

From Eq. (21), the conservation of energy for the whole system can be written as

$$\begin{aligned}\sum_k \left[\frac{\partial \phi_k u_k \rho_k \mathbf{v}_k}{\partial t} + \nabla\cdot(\phi_k u_k \rho_k \mathbf{v}_k \mathbf{v}_k)\right] + \frac{\partial \xi\alpha}{\partial t} + \nabla\cdot(\xi\alpha\mathbf{v}_\omega) = \\ \sum_k \left[\phi_k \boldsymbol{\sigma}_k : \nabla\mathbf{v}_k - \nabla\cdot\phi_k\mathbf{q}_k + \phi_k Q_k\right] + \nabla\cdot(\omega\alpha\mathbf{v}_\omega)\end{aligned} \tag{22}$$

where the averaged rate of interfacial energy transfer, $\sum_k \sum_{z\neq k} E_{k,z}$, is now explicitly modelled through the surface energy ξ and surface tension coefficient σ, which are related via $\xi = \sigma - T\frac{d\sigma}{dT}$ when they are functions of T only (c.f. Ishii & Hibiki, 2006). The "volumetric" effect of the interface is quantified by the interfacial area per unit volume, α, which is transported by the average interface velocity $\mathbf{v}_\omega$ (further details in section 2.6).

A more familiar form of Eq. (22) can be obtained representing it in terms of temperature, T. Assuming incompressible and homogenous dynamic phases, we have that the isochoric heat capacity C_V and the isobaric heat capacity C_P of each phase are the same. Therefore, for each phase k, we have $\mathrm{D}u_k = C_k \mathrm{D}T_k$, where C_k is the intrinsic phase average of heat capacity. Furthermore, under the assumption of thermal equilibrium between coexisting dynamic phases (and their dividing interface), we can rewrite Eq. (22) in terms of a single temperature field, which leads to the total energy conservation equation for a multi-phase system,

$$\begin{aligned}\sum_k \phi_k\rho_k C_k \frac{\mathrm{D}_k}{\mathrm{D}t}T - T\frac{\mathrm{D}_\omega}{\mathrm{D}t}\left(\alpha\frac{d\sigma}{dT}\right) - T\alpha\frac{d\sigma}{dT}\nabla\cdot\mathbf{v}_\omega = Q - \nabla\cdot\mathbf{q} \\ + \sum_k\sum_{z>k} c_{k,z}\Delta\mathbf{v}_{k,z}\cdot\Delta\mathbf{v}_{k,z} + \sum_k \phi_k\tau_k : \nabla\mathbf{v}_k \\ - \sum_k (P_\omega - P_k)\frac{\mathrm{D}_k}{\mathrm{D}t}\phi_k - \sigma\frac{\mathrm{D}_\omega}{\mathrm{D}t}\alpha + \sum_k\sum_{z>k}\Delta H_{k,z}\Gamma^m_{k,z}\end{aligned} \tag{23}$$

where $\frac{D_k}{Dt}$ and $\frac{D_\omega}{Dt}$ are the standard material derivatives with respect to $\mathbf{v}_k$ or $\mathbf{v}_\omega$, respectively.

Equation (23) describes the evolution of the averaged temperature of a system formed by incompress-

ible dynamic phases, under the assumptions of local thermal and thermodynamic equilibrium. It is derived combining the conservation of internal energy of the whole system (22), together with the complete mass and momentum equations (Eqs. (12) and (17), and their respective interaction terms (see section 2.6). Time-dependent temperature changes are computed in the left-hand side, whereas the right-hand side terms are related to heat sources and fluxes, including (in order) internal heat sources Q, thermal diffusion $\nabla \cdot q$, work associated with the mechanical interaction between phases, mechanical dissipation, work due to out-of-equilibrium pressure differences between phases and interfaces, work done by surface tension, and heat release due to phase change effects. The last term in Eq. (23) ensures consistency between the computed temperature field and the enthalpy ($h_j = u_j - \frac{P_j}{\rho_j}$) of the reactions occurring in the system. Note that the released/absorbed heat due to any and all phase transformations is retrieved from the Gibbs free-energy minimization solver (Section 4.4).

2.5 Chemical transport

Ignoring diffusion of chemical species (or components) between dynamic phases, the local chemical mass conservation equation can be written as

$$\frac{\partial \rho \tilde{c}^b}{\partial t} + \nabla \cdot \left(\rho \tilde{c}^b \mathbf{v} \right) = 0 \tag{24}$$

where $\tilde{c}_b$ refers to chemical component weight-fractions. For instance, in a system made up entirely of olivine, $\tilde{c}_b$ would correspond to the three basic chemical oxides, MgO, FeO and SiO_2. From Eq. (24), we derive the ensemble-averaged chemical mass conservation equation

$$\frac{\partial \langle \chi_k \rho \tilde{c}^b \rangle}{\partial t} + \nabla \cdot \langle \chi_k \rho c^b \mathbf{v} \rangle = \langle \rho \tilde{c}^b \left(\mathbf{v} - \mathbf{v}_i \right) \cdot \nabla \chi_k \rangle \tag{25}$$

which can be rewritten in terms of averaged quantities as

$$\frac{\partial \phi_k \rho_k c_k^b}{\partial t} + \nabla \cdot \left(\phi_k \rho_k c_k^b \mathbf{v}_k \right) = \sum_{z \neq k} \Gamma_{k,z}^b \tag{26}$$

where, $c_k^b = \frac{\langle \chi_k \rho \tilde{c}^b \rangle}{\phi_k \rho_k}$ is the averaged component (oxide)

$\sum_{z \neq k} \Gamma_{k,z}^b = \langle \rho \tilde{c}^b \left(\mathbf{v} - \mathbf{v}_i \right) \cdot \nabla \chi_k \rangle$ is the interfacial chemical mass transfer rate

c_k^b refers to the averaged weight fraction of any component b within each dynamic phase k. The mass transfer rate, $\Gamma_{k,j}^b$, is defined by the quantity of oxide b exchanged between dynamic phase k and any other coexisting dynamic phase j, and therefore, $\sum_k \sum_{z \neq k} \Gamma_{k,z}^b = 0$ in order to conserve mass. In addition, $\Gamma_{k,j}^b$ needs to ensure that the stoichiometry between components inside each dynamic phase is fulfilled for a given petrological assemblage. This is ensured via the thermodynamic solver (see

section 3). For the olivine example, c_k^b refers to the weight fraction of $b = \{MgO, FeO \text{ or } SiO_2\}$ pertaining to $k = \{solid \text{ or } liquid\}$; the mass transfer rate controls the component exchange between the solid and liquid phase, ensuring that the olivine stoichiometry is satisfied in both phases individually. Thus, Eq. (26) represents two different sets of equations for the two-phase olivine system, where the components of both phases are independently transported with their respective phase velocities.
Equation (26) can be combined with the mass conservation equation (12), which results in the following Lagrangian chemical transport equation

$$\frac{\mathrm{D}_{\mathbf{v}_k}}{\mathrm{D}t} c^b = \frac{1}{\phi_k \rho_k} \left(\sum_{z \neq k} \Gamma_{k,z}^b - c_k^b \sum_{z \neq k} \Gamma_{k,z}^m \right) \tag{27}$$

Both Eulerian and Lagrangian forms of the chemical transport equation describe the transport of each component in each of the dynamic phases separately. Therefore Eq. (26) or (27) applied to a N-phase Q-component system is represented by a coupled $N \times Q$ system of equations. This system can be considerably simplified if thermodynamic equilibrium is assumed between dynamic phases (e.g. Tirone et al., 2009). In this case, we only need the system's bulk composition to solve the Gibbs free energy minimization problem, thus reducing the number of unknowns of the system from (number of dynamic phases $\times$ number of components) to Q (number of components). If equilibrium between dynamic phases is not warranted, however, separate free energy minimizations need to be performed for each dynamic phase, which would require a detailed description of the chemistry of each dynamic phases. We discuss this further in Section 6.1.
For cases where equilibrium between dynamic phases can be assumed, an equivalent transport expression to Eq. (26) or (27) can be derived in order to solve the chemical transport for the weight fraction c^b of any chemical component within our system. This expression is obtained by adding Eq. (26) over all the dynamic phases

$$\frac{\partial \overline{\rho} c^b}{\partial t} + \nabla \cdot \left(\overline{\rho} c^b \mathbf{v}^b \right) = 0 \tag{28}$$

where $\overline{\rho} = \sum_k \phi_k \rho_k$ is the averaged mixture thermodynamic density, $c^b = \frac{1}{\overline{\rho}} \sum_k \phi_k \rho_k c_k^b$ is the total weight fraction of component b, and $\mathbf{v}^b = \frac{1}{\overline{\rho} c^b} \sum_k \phi_k \rho_k c_k^b \mathbf{v}_k$ refers to the averaged velocity at which each oxide b is advected. Again, for the simple two-phase olivine system, Eq. (28) represents the individual transport of the oxides $\{MgO, FeO \text{ and } SiO_2\}$ (but now for the total weight fraction) according to their individual velocities $\mathbf{v}^{MgO}$, $\mathbf{v}^{FeO}$, $\mathbf{v}^{SiO_2}$.
Besides representing a smaller system of equations (dimension Q), Eq. (28) has the additional advantage that the interfacial terms in the right-hand side disappear from the transport equation, simplifying

the numerical solution. This formulation also enables the advection of the bulk chemistry, c^b, using a single weighted velocity, $\check{\mathbf{v}}$, via the following lagrangian description

$$\frac{\mathrm{D}_{\check{\mathbf{v}}}}{\mathrm{D}t} c^b = \frac{1}{\overline{\rho}} \nabla \cdot \left(\overline{\rho} c^b \left[\check{\mathbf{v}} - \mathbf{v}^b \right] \right) \tag{29}$$

where $\check{\mathbf{v}} = \sum_b c^b \mathbf{v}^b$ is a composition-weighted velocity. The right-hand side (RHS) term of Eq. (29) accounts for the relative motion of the components, and therefore it corrects the bulk chemistry along the trajectory of $\check{\mathbf{v}}$. Again, this term needs to ensure that the stoichiometry between phase components is satisfied (proportionality between different oxides, i.e. $\left(\mathrm{RHS}^{FeO} + \mathrm{RHS}^{MgO}\right) / \mathrm{RHS}^{SiO_2} = cte$). This is true, since the right-hand side of Eq. (29) is a lineal combination of c_k^b, which are consistently retrieved from our thermodynamic model and thus preserve the stoichiometry. Indeed, after some algebra, and using the definitions of $\check{\mathbf{v}}$, $\mathbf{v}^b$ and c^b, the RHS of Eq. (29) can be decomposed as (dropping off $\frac{1}{\overline{\rho}}\nabla\cdot$),

$$\begin{aligned}
\overline{\rho} c^b \left[\check{\mathbf{v}} - \mathbf{v}^b \right] &= \overline{\rho} c^b \left(\sum_b c^b \mathbf{v}^b \right) - \overline{\rho} c^b \mathbf{v}^b \\
&= c^b \left(\sum_b \sum_k \phi_k \rho_k c^b \mathbf{v}^b \right) - \sum_k \phi_k \rho_k c_k^b \mathbf{v}_k \\
&= c^b \left(\sum_k \sum_b \phi_k \rho_k c^b \mathbf{v}^b \right) - \sum_k \phi_k \rho_k c_k^b \mathbf{v}_k \\
&= \frac{1}{\overline{\rho}} \left(\sum_k \phi_k \rho_k c_k^b \right) \left(\sum_k \phi_k \rho_k \mathbf{v}^b \right) - \sum_k \phi_k \rho_k c_k^b \mathbf{v}_k
\end{aligned} \tag{30}$$

Furthermore, it is easy to show that mass is conserved, as $\sum_b \frac{1}{\overline{\rho}} \nabla \cdot \left(\overline{\rho} c^b \left[\check{\mathbf{v}} - \mathbf{v}^b \right] \right) = 0$. Both conditions, stoichiometry and mass conservation are illustrated in Figure 3, where discrete values of $\frac{1}{\overline{\rho}} \nabla \cdot \left(\overline{\rho} c^b \left[\check{\mathbf{v}} - \mathbf{v}^b \right] \right)$ for a simple olivine experiment are shown.

2.6 Interface and interaction terms

The treatment of interfacial phenomena is the most important ingredient of multi-phase flow models, as phase interaction terms control the type and degree of thermo-mechanical-chemical coupling between dynamic phases and thus they ultimately define the nature and behaviour of the multi-phase system (c.f. Ishii, 1975; Hassanizadeh & Gray, 1979a; Gray & Hassanizadeh, 1989; Ochoa-Tapia & Whitaker, 1995a,b; Sun & Beckermann, 2004). As for the present formulation, interphase processes are modelled through the interaction terms arising after ensemble averaging the local balance equations. This section is devoted to the description of such models, based on both mathematical and

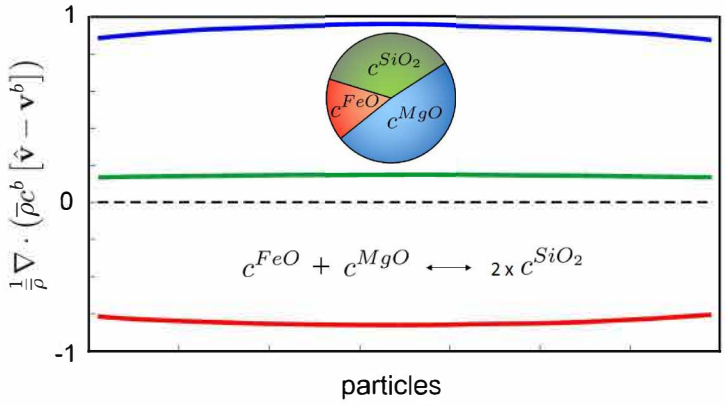

Figure 3. Normalized values of the right-hand side of the chemical mass balance Eq. (29) for a simple example with olivine. Mass conservation of the system components is inferred from the dashed line, which represents $\sum_b \frac{1}{\bar{\rho}}\nabla\cdot\left(\bar{\rho}c^b\left[\check{\mathbf{v}}-\mathbf{v}^b\right]\right)=0$. The stoichiometry between FeO (red), MgO (blue) and SiO (green), i.e. $c^{FeO}+c^{MgO}\leftrightarrow 2\times c^{SiO_2}$, is held exactly and correctly at every single Lagrangian point or particle (see section 4.3 for further details on the numerical discretization of the chemistry).

thermodynamic grounds. The proposed models are by no means unique, and one should review their applicability according to the system under consideration.

2.6.1 General considerations and definitions

Ideally, dynamic phases in a multi-phase system are separated by thin transition zones, called interfaces, which in a continuum description are treated as massless two-dimensional surfaces (surface and interface are used interchangeably). Although properties are generally discontinuous at interfaces, mass, momentum, energy and chemical component conservation equations must be fulfilled. This is mathematically represented by the jump conditions across the interface delimiting two dynamic phases, k and j (denoted as $S_{k,j}$ in Fig. 4),

$$\begin{aligned}
||\rho\left(\mathbf{v}-\mathbf{v}_i\right)\cdot\mathbf{n}|| &= 0\\
||\rho\mathbf{v}\left(\mathbf{v}-\mathbf{v}_i\right)\cdot\mathbf{n}-\boldsymbol{\sigma}\cdot\mathbf{n}|| &= \tilde{\sigma}_{k,j}\tilde{\kappa}_{k,j}\mathbf{n}_{k,j}\\
||\rho u\left(\mathbf{v}-\mathbf{v}_i\right)\cdot\mathbf{n}-\mathbf{q}\cdot\mathbf{n}|| &= \tilde{\xi}_{k,j}\\
||\rho\mathbf{c}^{\mathbf{b}}\left(\mathbf{v}-\mathbf{v}_i\right)\cdot\mathbf{n}|| &= 0
\end{aligned} \tag{31}$$

where $\mathbf{v}_i$ is the velocity of the interface, $\tilde{\sigma}_{k,j}$ is the true surface tension coefficient, $\tilde{\kappa}_{k,j}=\nabla\cdot\mathbf{n}_{k,j}$ is the local curvature of the interface, $\mathbf{n}_{k,j}$ is the normal unit vector to the surface (pointing outwards from k to j) and $||()||$ denotes a jump of a function f across $S_{k,j}$, as $||f||=f_k-f_j$. The term $\tilde{\sigma}_{k,j}\tilde{\kappa}_{k,j}\mathbf{n}_{k,j}$ is the force per unit area associated with surface tension at $S_{k,j}$, and $\tilde{\xi}_{k,j}$ is the internal

surface energy of the same surface. In theory however, multiphase system might be compound by more than one interface, as depicted in Fig. 4. We note that the jump conditions in Eqs. (31) are only defined at the interface between dynamic phases k and j ($S_{k,j}$ in Fig. 4) and therefore, unless otherwise indicated, all the properties discussed in this section refer exclusively to this interface. In addition, the jump conditions in Eqs. (31) imply, first, the existence of an explicit surface energy and a stress discontinuity (surface tension) across the interface; thus the two dynamic phases in each side of the interface are subject to different pressures in the presence of surface tension. Second, they require a phase-boundary whose shape, location and orientation is known.

Representing surface processes in terms of jump conditions over an infinitesimally thin layer, however, is a mathematical idealization. In practice, we need expressions for the average macroscopic behaviour of microscopic interfacial processes, rather than a detailed description of the thermodynamic state of the interface. The location and orientation of the interface is given by $|\nabla\chi_k|$, which is in fact a delta Dirac function centered at the interface, times $\mathbf{n}_{k,j}$. $|\nabla\chi_k|$ plays the role of "picking up" the interface k from the multiphase mixture, and therefore it can be understood as the characteristic function for the interface. Since the exact location and orientation of the interface is unknown in our formulation, we need to incorporate its effects on the mixture's properties/behaviour by computing average interface properties. Under isotropic conditions, the "volumetric" average effect of interfaces is controlled by the interfacial area density, $\alpha_{k,j}$ (Ni & Beckermann, 1991). This parameter, which is defined as $\alpha_{k,j} = -\langle \mathbf{n}_{k,j} \cdot \nabla\chi_k \rangle$, is commonly modelled as a function of phase abundances ϕ_k and ϕ_j, but it can adopt different forms depending on the application. One of the simplest forms is that proposed by Ni & Beckermann (1991) and generalized in Bercovici et al. (2001)

$$\alpha_{k,j} = \alpha_0 \phi_k^a \phi_j^b \tag{32}$$

where α_0, a and b are parameters (typically constants) accounting for different material properties and geometries of the interface. For illustrative purposes, we will adopt this form in this study, acknowledging that it may be too simplistic to model real scenarios of geological interest.

Further insight on the interfacial terms can be gained by ensemble averaging the jump conditions in Eqs. (31). Following the same two-step procedure as in sections (2.2, 2.3, 2.4 and 2.5), jump conditions are first multiplied by $|\nabla\chi_k|$ (not by χ_k, as discussed above) and then ensemble-averaged to give

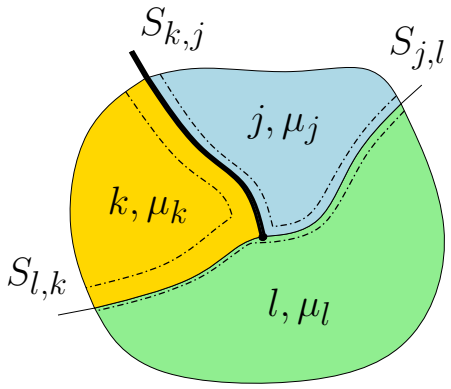

Figure 4. Schematic illustration of a three-phase $k-j-l$ interface morphology. The interface between dynamic phases k and j, $S_{k,j}$, is highlighted. Selvedge layers appear embedded into their respective dynamic phases (dashed lines). The thicknesses of the selvedge layers vary as functions of the phases' viscosities ($\mu_l < \mu_j < \mu_k$).

$$
\begin{aligned}
\langle[\rho\left(\mathbf{v}-\mathbf{v}_i\right)]\cdot\nabla\chi_k\rangle + \langle[\rho\left(\mathbf{v}-\mathbf{v}_i\right)]\cdot\nabla\chi_j\rangle &= \Gamma^m_{k,j}+\Gamma^m_{j,k}=0\\
\langle[\rho\mathbf{v}\left(\mathbf{v}-\mathbf{v}_i\right)-\boldsymbol{\sigma}]_k\cdot\nabla\chi_k\rangle + \langle[\rho\mathbf{v}\left(\mathbf{v}-\mathbf{v}_i\right)-\boldsymbol{\sigma}]\cdot\nabla\chi_j\rangle &= \boldsymbol{M}_{k,j}+\boldsymbol{M}_{j,k}=\sigma_{k,j}\langle\tilde{\kappa}_{k,j}\nabla\chi_k\rangle\\
\langle[\rho u\left(\mathbf{v}-\mathbf{v}_i\right)-\mathbf{q}]\cdot\nabla\chi_k\rangle + \langle[\rho u\left(\mathbf{v}-\mathbf{v}_i\right)-\mathbf{q}]\cdot\nabla\chi_j\rangle &= E_{k,j}+E_{j,k}=\xi_{k,j}\\
\langle[\rho\mathbf{c}^b\left(\mathbf{v}-\mathbf{v}_i\right)]\cdot\nabla\chi_k\rangle + \langle[\rho\mathbf{c}^b\left(\mathbf{v}-\mathbf{v}_i\right)]\cdot\nabla\chi_j\rangle &= \Gamma^b_{k,j}+\Gamma^b_{j,k}=0
\end{aligned}
\tag{33}
$$

where $\sigma_{k,j}$ is the averaged surface tension coefficient (assumed constant), $\xi_{k,j} = \langle\tilde{\xi}_{k,j}\nabla\chi_k\rangle$ is the averaged surface energy for $S_{k,j}$, and $\nabla\chi_k = -\nabla\chi_j$ at the interface between the two dynamic phases. $\Gamma^m_{k,j}$, $\boldsymbol{M}_{k,j}$, $E_{k,j}$ and $\Gamma^b_{k,j}$ are the mass, momentum, energy, and chemical components interaction terms, respectively, across $S_{k,j}$. As previously mentioned, under the framework of ensemble averaging, interfaces as well as dynamic phases are treated as continuum average quantities that exist over the entire domain. Consequently, interaction terms become averaged effective body sources acting at all points in the domain. Among the existing models for the averaged surface body force (Bercovici et al., 2001; Fischer et al., 2008, and references therein), we consider

$$
\sigma_{k,j}\langle\tilde{\kappa}_{k,j}\nabla\chi_k\rangle = \nabla\left(\alpha_{k,j}\sigma_{k,j}\right) \tag{34}
$$

where surface tension variations along the interface (i.e. Marangoni effects) are assumed negligible. The results in Eqs. (33) provide formal conditions that interaction terms need to fulfill; yet, they are relations for individual averaged surfaces (e.g. $S_{k,j}$). What we seek now are averaged relations con-

cerning the union of all the interfaces of interest so as to define averaged interface variables such as interface density α, interface pressure P_ω or interfacial velocity $\mathbf{v}_\omega$. For this, we collapse the contribution of all the surfaces into a single average interface, $S = \sum_k \sum_{z>k} S_{k,z}$, which enables us to write expressions for the total averaged surface tension force $\mathbf{m}_i$ and total averaged interfacial energy ξ_i as,

$$\begin{aligned} \mathbf{m}_i &= \sum_k \sum_{z>k} \nabla \left(\alpha_{k,z}\sigma_{k,z}\right) = \nabla\left(\sigma\alpha\right) \\ \xi_i &= \sum_k \sum_{z>k} \xi_{k,z} \end{aligned} \tag{35}$$

The averaged mechanical and thermodynamic state of the interface is thus described by its surface energy ξ_i, surface density $\alpha = \sum_k \sum_{z>k} \alpha_{k,z}$, and the effective surface tension coefficient $\sigma = \frac{\sum_k \sum_{z>k} \alpha_{k,z}\sigma_{k,z}}{\alpha}$. The surface energy, is typically considered to be an energy excess (or anomaly) resulting from the rearrangement of atoms near the surface (Leo & Sekerka, 1999; Fischer et al., 2008). When creating a new surface area, atomic bonds near the exposed surface are broken in order to create a new relaxed atomic environment, which will in general differ from the original equilibrium structure (Sutton & Balluffi, 1995). The surface energy is thus the amount of energy required to create this new surface area with the same atomic structure. From a thermodynamic point of view, it is defined as the excess Gibbs free energy per unit of surface area (i.e. the thermodynamic potential per unit of surface area that is required in order to reversibly increase the surface under consideration). Therefore, the surface is not an infinitesimally thin section delimiting dynamic phases, but the sum of two layers (each several molecules deep and embedded in the dynamic phases conforming the interface), where the energy anomalies exist. This two layers are often referred as selvedges, and are illustrated in Fig. 4.

Since surface energy is the sum of the energy anomalies existing at the selvedges of each dynamic phase, we assume that when ensemble averaged, interfacial quantities such as interfacial energy ξ_i and surface tension force $\mathbf{m}_i$ (Eqs. (35)) are not uniformly partitioned among the coexisting dynamic phases, but according to their molecular bond strength; in other words, in proportion to the extent to which the selvedge layers are embedded in their respective dynamic phases. As such, the apparent partitioning of the averaged interfacial energy, as well as surface tension between the phases, can be modelled via a single weighting fraction ω_k. Based on these considerations, Bercovici & Ricard (2003) suggested a definition for ω_k, considering that materials with larger molecular bonds (and therefore larger activation energies), carry larger energy anomalies, and thus, their contribution to the total surface energy is greater. They defined ω_k as a function of viscosity, arguing that information about the activation energy (or molecular bond strength) is mainly contained in this material property

(see section 3 in Bercovici & Ricard (2003) for further discussion on the topic). Here we extend their definition of the partition coefficient ω_k to multiple dynamic phases, as,

$$\omega_k = \frac{\phi_k \mu_k}{\sum_k \phi_k \mu_k} \tag{36}$$

where $0 \leq \omega_k \leq 1$. In summary, Eq. (36) implies that the dynamic phase with larger viscosity/activation energy carries more surface tension and surface energy with it. For two dynamic phases (fluid (f)- solid (s)) at mantle conditions, $\mu_f \ll \mu_s$ and hence $\omega_f \approx 0$.

In the following we provide further details on the modelling of interaction terms for both momentum and energy conservation equations.

2.6.2 Momentum interaction term and surface tension

The momentum interaction force for a given dynamic phase k results from the forces acting on that particular phase across the multiple interfaces $\sum_{z \neq k} \mathbf{M}_{k,z}$ is written as,

$$\sum_{z \neq k} \mathbf{M}_{k,z} = \langle [\rho \mathbf{v} (\mathbf{v} - \mathbf{v}_i) - \boldsymbol{\sigma}] \cdot \nabla \chi_k \rangle \approx \sum_{z \neq k} c_{k,z} \Delta \mathbf{v}_{k,z} + P_\omega \nabla \cdot \phi_k + \omega_k \nabla (\sigma \alpha) \tag{37}$$

where the phase change contribution to the momentum exchange has been neglected (appropriate for geodynamic timescales), and only mechanical effects have been taken into account. $c_{k,j}$ is a symmetric, rheology-dependent interaction coefficient between phase j and k (see below), $\Delta \mathbf{v}_{k,j} = \mathbf{v}_k - \mathbf{v}_j$ is the velocity difference between dynamic phases, and P_ω refers to a constant interfacial pressure (see below). As mentioned before, $\nabla (\sigma \alpha)$ is the effective body force accounting for the averaged surface tension in the system (Eq. (35)). The first two terms in the right-hand side of Eq. (37) represent the Galilean-invariant interaction force due to interfacial stresses, i.e. mechanical interaction or interfacial drag forces between phases. The last term represents the surface tension contribution to each dynamic phase from all existing surfaces. Although this seems somewhat counterintuitive, it is consistent with the continuum approach to modelling surface tension effects. For the example depicted in Fig. 4, according to the definition in Eq. (37), phase k is also influenced by interfaces in the system other than its own (hereafter referred to as *external surface tension*, $S_{j,l}$), since $\nabla (\sigma \alpha) = \sum_k \sum_{z>k} \nabla (\alpha \sigma)_{k,j}$ (where $\sum_k \sum_{z>k} \nabla (\alpha \sigma)_{z,j} \equiv \sum_k \sum_{z>k} \nabla (\alpha_{k,z} \sigma_{k,z})$). The nature and extent of this external surface tension is, however, reflected in ω_k (by the presence of μ_j and μ_l) and thus, indirectly included when the total surface tension is weighted by ω_k. When the external surface tensions in $S_{j,l}$ and $S_{l,k}$ are negligible in comparison with that on $S_{k,j}$ (Fig. 4), the total surface tension force is the surface tension in $S_{k,j}$ ($\nabla (\sigma \alpha) = \nabla (\sigma \alpha)_{k,j}$).In this case, $\mu_k \gg \mu_j > \mu_l$ and hence $\omega_k = 1$. On the contrary, if surface tension is negligible on $S_{k,j}$ and $S_{l,k}$, we obtain $\omega_k = 0$, and thus there is no surface tension

effect acting over dynamic phase k ($\omega_k \nabla(\sigma\alpha) = 0$), even in the presence of external surface tensions in $S_{j,l}$ ($\nabla(\sigma\alpha) = \nabla(\sigma\alpha)_{j,l} \neq 0$).

Notice that in absence of surface tension, and for a two-phase system, $\sum_{z \neq k} \mathbf{M}_{k,z}$ ensures $\mathbf{M}_{k,j} = -\mathbf{M}_{j,k}$ (equal and opposite force of one phase against the other), whereas for a general multiphase flow including surface tension, $\sum_k \sum_{z \neq k} \mathbf{M}_{k,z} = \nabla(\sigma\alpha)$.

Depending on the nature of the system $c_{k,j}$ may adopt a different form (Zhang & Prosperetti, 1997; Drew & Passman, 1999; Bercovici et al., 2001; Bercovici & Michaut, 2010). For viscous flows involving melt percolation through a permeable matrix, $c_{k,j}$ is related to the fluid viscosity, μ_f, and matrix permeability, k_s, such that $c_{k,j} \sim \mu_f / \mathrm{k}_s$. Likewise, when dealing with turbulent flows $c_{k,j}$ depends on eddy velocities and phase densities. General estimates of $c_{k,j}$ do not exist, and its definition should always be related to the particular system under consideration.

As for the interfacial pressure, P_ω, it is defined as a $\omega-$weighted average of the coexisting pressures at the interface,

$$P_\omega = \sum_k \frac{1 - \omega_k}{\sum_k (1 - \omega_k)} P_k \tag{38}$$

which is the natural extension of the interface pressure in (Bercovici & Ricard, 2003) for multiphase systems. The behavior of P_ω can be understood by rewriting the pressure jump between two phases, k and j, as the difference between the pressure jump across the k-selvedge layer and that across j, such that $\Delta P_{k,j} = (P_k - P_\omega) - (P_j - P_\omega)$. For a three dynamic phase system (k, j, and l in Fig. 4), with $\mu_k \gg \mu_j > \mu_l$ all the surface effects should be embedded in the k phase, since $\omega_k = 1$ and $\omega_j = \omega_l = 0$. Therefore, the entire pressure drop across the interface delimiting phase k is accounted for by the k-selvedge layer, i.e. controlled by the first term, $P_k - P_\omega$. It is clear that for this case, $P_\omega = 0.5(P_j + P_l)$, and hence $P_\omega = P_j = P_l$ as $P_j = P_l$. Furthermore, in absence of gravity and when pressures are uniform and equal, the multiphase system should remain motionless even if $\nabla\phi_k \neq 0$. This means that when $\nabla P_k = 0$ and $P = P_k$, the force balance in Eq. (18) should read $P\nabla\phi_k - \sum_{z \neq k} \mathbf{M}_{k,z} = 0$ if $\Delta \mathbf{v}_{k,j} = \boldsymbol{\tau}_k = 0$ is to be zero. Indeed, Eq. (37) verifies the equilibrium condition, as $P_\omega = P$ and consequently $\Delta \mathbf{v}_{k,j} = \boldsymbol{\tau}_k = 0$, since $\sum_{z \neq k} \mathbf{M}_{k,z} = P\nabla\phi_k$ by definition.

2.6.3 Surface energy

As shown in Eq. (35) the energy contribution from all existing interfaces collapses into an averaged surface energy ξ, whose thermodynamic evolution could be modelled via appropriate conservation equations and their respective interaction terms. However, for the purposes of this study, the energy balance in Eqs. (23)-(22) is solved for the mixture system, i.e. adding contributions from individual

phases (internal energies) and interfaces (surface energies) into the total energy budget. Despite the simple form of Eqs. (22)-(23), there are several implicit assumptions in its derivation that need further discussion.

First, we account for the interfacial surface energy in terms of the volumetric energy density as $\xi_i \alpha$, where ξ_i refers to the total surface energy per unit area. This is obtained adding all energy anomalies from every selvedge layer of the system (Eq. (35)). Secondly, we assume that the interfacial surface energy is transported by the effective velocity of the interface, defined as

$$\mathbf{v}_\omega = \sum_k \omega_k \mathbf{v}_k \tag{39}$$

which reflects the extent to which the interface is advected by each of the dynamic phases. The total bulk transport in Eq. (22) as $\nabla \cdot (\xi_i \alpha \mathbf{v}_\omega)$ is thus controlled by the ω_k-weighted average velocity in Eq. (39). In addition, the surface work in Eq. (22), defined as $\nabla \cdot (\sigma \alpha \mathbf{v}_\omega)$, is controlled by the averaged interface velocity in Eq. (39).

Thus, with the previous considerations, the conservation equation for the averaged interfacial energy reads

$$\frac{\partial \xi_i \alpha}{\partial t} + \nabla \cdot (\xi_i \alpha \mathbf{v}_\omega) - \nabla \cdot (\sigma \alpha \mathbf{v}_\omega) = 0 \tag{40}$$

which we assume equivalent to the sum of all the energy transfer rates across interfaces, $\sum_k \sum_{z \neq k} E_{k,z}$.

2.7 Rheology

In order to obtain a closed MPMCRT formulation we need to supplement our set of conservation equations and interaction terms with constitutive laws defining the rheological behaviour of the multi-phase system. In particular, we need to relate the averaged phase stress tensor $\boldsymbol{\sigma}_k$ to averaged phase velocities $\mathbf{v}_k$ and pressures P_k. Since our intention is to formulate a general scheme that can be applied to a large number of geodynamic problems, we need to deal with the three main constitutive laws governing the deformation of Earth materials, namely elastic, plastic and viscous. Which of these three rheologies dominates the bulk deformation of the multi-phase system will depend not only on the nature and abundance of the actual phases (and their interactions) but also on the local P-T conditions and spatial-temporal time scales of the process of interest.

Plastic behaviour is implemented via the "effective viscosity" approach, which has been described and validated in previous works (e.g. Moresi et al., 2003; Kaus, 2010; Keller et al., 2013); in particular, we follow exactly the formulation in Keller et al. (2013). Therefore, we focus the following discussion on the implementation of the visco-elastic rheology. A local visco-elastic rheology is first introduced,

Table 2. Viscous and elastic constitutive laws

Newtonian Isotropic Viscous Rheology	*Linear Elastic Rheology*
$\boldsymbol{\sigma}_v = -\mathcal{P}\cdot\mathbf{Id} + \xi\ \mathrm{tr}\left(\dot{\boldsymbol{\varepsilon}}_v\right)\cdot\mathbf{Id} + 2\mu\boldsymbol{\varepsilon}'_v$	$\hat{\boldsymbol{\sigma}}_e = \lambda\ \mathrm{tr}\left(\dot{\boldsymbol{\varepsilon}}_e\right)\cdot\mathbf{Id} + 2G\dot{\boldsymbol{\varepsilon}}'_e$
$\boldsymbol{\sigma}^\circ_v = \left(-\mathcal{P} + \xi\ \mathrm{tr}\left(\dot{\boldsymbol{\varepsilon}}_v\right)\right)\cdot\mathbf{Id}$	$\hat{\boldsymbol{\sigma}}^\circ_e = K\ \mathrm{tr}\left(\dot{\boldsymbol{\varepsilon}}_e\right)\cdot\mathbf{Id}$
$\boldsymbol{\tau}_v = 2\mu\boldsymbol{\varepsilon}'_v$	$\hat{\boldsymbol{\tau}}_e = 2G\dot{\boldsymbol{\varepsilon}}'_e$

based on individual viscous and elastic constitutive laws (section 2.7.1). This constitutive law is then ensemble-averaged in order to obtain the final individual deviatoric and volumetric rheologies (section 2.7.2 and 2.7.3).

2.7.1 Local visco-elastic constitutive law

The individual viscous and elastic constitutive laws (hereafter indicated with subindices v and e, respectively) are written in Table 2 in rate form for the case of isostropic materials.
where $\mathcal{P}$ is the so-called thermodynamic or equilibrium pressure, $\dot{\boldsymbol{\varepsilon}} = \frac{1}{2}\left(\nabla\mathbf{v} + [\nabla\mathbf{v}]^T\right)$ the strain-rate, ξ the bulk or volumetric viscosity, μ the shear viscosity, $K = \lambda + 2/3G$ the bulk modulus, G the shear or rigidity modulus and λ is the first Lamé constant (c.f. Batchelor, 2000; Schlichting & Gersten, 2003; Bower, 2009). Note that with the previous definition of strain-rate, $\mathrm{tr}\left(\dot{\boldsymbol{\varepsilon}}\right) = \nabla\cdot\mathbf{v}$. In addition, the mechanical pressure is defined as $P = -\frac{\mathrm{tr}(\boldsymbol{\sigma})}{3}$, which is related to the thermodynamic pressure via $P - \mathcal{P} + \xi\nabla\cdot\mathbf{v} = 0$. Consequently, the mechanical pressure P and the thermodynamic pressure $\mathcal{P}$ are not equivalent unless $\xi\nabla\cdot\mathbf{v} = 0$, which is the case for incompressible media.
We use a Maxwell model to combine viscous and elastic rheologies into one local visco-elastic constitutive relation. The deviatoric and volumetric components of the combined visco-elastic constitutive law read, respectively

$$\begin{aligned} \dot{\boldsymbol{\varepsilon}}' &= \frac{\boldsymbol{\tau}}{2\mu} + \frac{1}{2G}\hat{\boldsymbol{\tau}} \\ \mathrm{tr}\left(\dot{\boldsymbol{\varepsilon}}\right) &= \frac{1}{\xi}\left(\mathcal{P} + 3\ \mathrm{tr}\left(\boldsymbol{\sigma}\right)\right) + \frac{1}{K}\ \mathrm{tr}\left(\hat{\boldsymbol{\sigma}}\right) \end{aligned} \tag{41}$$

which implicitly means that $\boldsymbol{\sigma} = \boldsymbol{\sigma}_v = \boldsymbol{\sigma}_e$ and $\dot{\boldsymbol{\varepsilon}} = \dot{\boldsymbol{\varepsilon}}_v + \dot{\boldsymbol{\varepsilon}}_e$. We model $\hat{\boldsymbol{\tau}}$ (objective time derivative of $\boldsymbol{\tau}$) with the Jauman stress rate, $\hat{\boldsymbol{\tau}} = \frac{\mathrm{D}}{\mathrm{D}t}\boldsymbol{\tau} - \mathbf{W}\boldsymbol{\tau} + \boldsymbol{\tau}\mathbf{W}$, where $\frac{\mathrm{D}}{\mathrm{D}t}\boldsymbol{\tau}$ is the material derivative (stress tensor translation), and $\mathbf{W} = \frac{1}{2}\left(\nabla\mathbf{v} - [\nabla\mathbf{v}]^T\right)$ is the vorticity tensor (stress tensor rotation). Although this definition of objective stress derivative is neither the only one nor the most general one (de Souza Neto et al., 2011), it is the simplest to implement and its validity in geodynamic contexts

have been demonstrated in a number of previous studies (e.g. Muhlhaus & Regenauer-Lieb, 2005; Beuchert & Podladchikov, 2010); therefore we do not further discuss it here.

2.7.2 Averaged Visco-elasto-plastic deviatoric rheology

Proceeding as before, we condition the averaged visco-elastic deviatoric constitutive law to the presence of single dynamic phase k by using χ_k and the ensemble average operator; this yields

$$\dot{\boldsymbol{\varepsilon}}'_k = \frac{\boldsymbol{\tau}_k}{2\mu_k} + \frac{1}{2G_k}\hat{\boldsymbol{\tau}}_k \tag{42}$$

where μ_k and G_k are assumed constants at every realization of the ensemble, $\boldsymbol{\tau}_k$ is the averaged deviatoric stress tensor (see Appendix A3), $\hat{\boldsymbol{\tau}}_k$ is the averaged objective Jaumann derivative and $\dot{\boldsymbol{\varepsilon}}'_k$ is the averaged deviatoric strain-rate tensor. The latter can be written as (Appendix A3)

$$\dot{\boldsymbol{\varepsilon}}'_k = \frac{1}{2}\left(\nabla\mathbf{v}_k + [\nabla\mathbf{v}_k]^\top - \frac{2}{3}\nabla\cdot\mathbf{v}_k\mathbf{Id}\right) \tag{43}$$

We define the averaged Jaumann derivative in Eq. (42) as

$$\hat{\boldsymbol{\tau}}_k = \frac{\mathrm{D}_k}{\mathrm{D}t}\boldsymbol{\tau}_k - \mathbf{W}_k\boldsymbol{\tau}_k + \boldsymbol{\tau}_k\mathbf{W}_k \tag{44}$$

The averaged vorticity tensor is defined as a stress tensor average, $\mathbf{W}_k = \frac{\langle\chi_k\boldsymbol{\tau}\mathbf{W}\rangle}{\phi_k\boldsymbol{\tau}_k}$, which we approximate here as $\mathbf{W}_k \approx \frac{1}{2}\left(\nabla\mathbf{v}_k - \nabla\left[\mathbf{v}_k\right]^\top\right)$. Eq. (44) is simply the standard Jaumann derivative in terms of averaged values and has been obtained assuming $\frac{\mathrm{D}_k}{\mathrm{D}t}\boldsymbol{\tau}_k = \frac{1}{\phi_k}\langle\frac{\mathrm{D}}{\mathrm{D}t}\chi_k\boldsymbol{\tau}\rangle \approx \frac{1}{\phi_k}\frac{\mathrm{D}}{\mathrm{D}t}\langle\chi_k\boldsymbol{\tau}\rangle$, and therefore setting the second term in Eq. (A.11) to zero. This implies that either the fluctuation of the deviatoric stress tensor, $\tau_k^{''}$ in Eq. (A.8), is negligible, or the velocity field is truly solenoidal. This assumption is therefore exact when dealing with incompressible materials as $\nabla\cdot\mathbf{v} = 0$.

We discretize the time derivative in Eq. (42) with an implicit backward finite-difference scheme. Thus, we have

$$\hat{\boldsymbol{\tau}}_k = \frac{\boldsymbol{\tau}_k - \hat{\boldsymbol{\tau}}_k^0}{\Delta t} \tag{45}$$

where

$$\hat{\boldsymbol{\tau}}_k^0 = \frac{\mathrm{D}_k}{\mathrm{D}t}\boldsymbol{\tau}_k^0\Delta t - \left(\mathbf{W}_k^0\boldsymbol{\tau}_k^0 + \boldsymbol{\tau}_k^0\mathbf{W}_k^0\right)\Delta t \tag{46}$$

Note that $\hat{\boldsymbol{\tau}}_k^0$ accounts for the advection (first term on the right-hand side of Eq. (46)) and rotation (second term on the right-hand side of Eq. (46)) of the deviatoric stress tensor from the previous time step (denoted with superindex ^{0}). As explained in section 4.1 and Appendix B2, the stress advection

and rotation (Eq. (46)) is performed by storing the stresses $\boldsymbol{\tau}_k^0$ on Lagrangian particles, which are advected with their corresponding averaged velocity fields.

After some algebra, the visco-elastic rheology for the deviatoric stress can be written as,

$$\boldsymbol{\tau}_k = \frac{2}{\frac{1}{\mu_k} + \frac{1}{G_k \Delta t}} \dot{\boldsymbol{\varepsilon}}_k^{'} + \frac{1}{1 + \frac{G_k \Delta t}{\mu_k}} \hat{\boldsymbol{\tau}}_k^0 \tag{47}$$

As mentioned before, plastic yielding is included in Eq. (47) via the effective viscosity approach (Moresi et al., 2003; Kaus, 2010; Keller et al., 2013), where the viscosity in Eq. (47) is iteratively corrected to keep the local stresses on the yield surface. This simple procedure enables us to rewrite Eq. (47) in terms of effective viscosities μ_k^{eff}. Doing so, the final visco-elasto-plastic shear constitutive law for each of the dynamic phases reads

$$\boldsymbol{\tau}_k = 2\mu_k^{eff} \dot{\boldsymbol{\varepsilon}}_k^{'} + \chi_k^{\boldsymbol{\tau}} \hat{\boldsymbol{\tau}}_k^0 \tag{48}$$

with

$$\mu_k^{eff} = \left\{ \begin{array}{ll} \frac{\boldsymbol{\tau}_k^y - \chi_k^{\boldsymbol{\tau}} \boldsymbol{\tau}_{k,II}^0}{2\dot{\boldsymbol{\varepsilon}}_{k,II}^{'}} & \boldsymbol{\tau}_{k,II} = \boldsymbol{\tau}_k^y \\ \frac{1}{\frac{1}{\mu_k} + \frac{1}{G_k \Delta t}} & \boldsymbol{\tau}_{k,II} < \boldsymbol{\tau}_k^y \end{array} \right\}$$

$$\chi_k^{\boldsymbol{\tau}} = \frac{1}{1 + \frac{G_k \Delta t}{\mu_k}}$$

where $\dot{\boldsymbol{\varepsilon}}_{k,II}^{'} = \sqrt{\frac{1}{2}\dot{\boldsymbol{\varepsilon}}_{k_{ij}}^{'} \dot{\boldsymbol{\varepsilon}}_{k_{ij}}^{'}}$ is the second invariant of deviatoric strain rates (Einstein's summation convention applies), $\boldsymbol{\tau}_{k,II}^0$ is the second invariant of advected deviatoric stresses of the previous time step, and $\boldsymbol{\tau}_k^y$ is the scalar yield shear stress. The use of the effective viscosity approach in Eq. (48) enables us to keep the same form of the visco-elastic constitutive law as in Eq. (47), where plastic yielding is captured by limiting the values of stresses according to a prescribed failure envelope for the system under consideration. Furthermore, when local averaged deviatoric stresses remain below the plastic yield criterion, $\boldsymbol{\tau}_{k,II} < \boldsymbol{\tau}_k^y$, the effective viscosity μ_k^{eff} remains unchanged and the visco-elastic constitutive law in Eq. (47) is recovered from Eq. (48).

2.7.3 Averaged visco-elasto-plastic volumetric rheology

We now present an averaged constitutive law relating volumetric strain-rates and volumetic stresses at the interface. On the one hand, this constraints the difference in mechanical pressure for every pair of coexisting dynamic phases, $\Delta P_{k,j}$; on the other, it provides closure to the whole MPMCRT set of equations. This is achieved by combining averaged individual volumetric constitutive laws, under

material invariance requirements. Again, we isolate the volumetric phase contribution of Eq. (41), including surface tension, and apply ensemble averaging to obtain

$$\phi_k \nabla \cdot \mathbf{v}_k = -\frac{P_k + \omega_k \sigma \frac{\mathrm{d}\alpha}{\mathrm{d}\phi_k}}{\xi_k^V} + \frac{1}{K_k} \frac{\mathrm{D}}{\mathrm{D}t} \left(P_k + \omega_k \sigma \kappa_k \right) \tag{49}$$

where K_k is the average bulk modulus and $\xi_k^V = \xi_k \frac{P_k + \omega_k \sigma \frac{\mathrm{d}\alpha}{\mathrm{d}\phi_k}}{P_k - \mathcal{P}_k + \omega_k \sigma \frac{\mathrm{d}\alpha}{\mathrm{d}\phi_k}}$ is the volumetric viscosity controlling the averaged viscous volumetric compaction or expansion of the dynamic phase. This volumetric viscosity is dependent on both mechanic and thermodynamic pressures, the bulk viscosity and the surface tension. In this way, the thermodynamic pressure in Eq. (41) is absorbed into the volumetric viscosity, which greatly simplifies the resulting volumetric constitutive law, as otherwise an additional equation to constrain the thermodynamic pressure would be required . Note that in the absence of surface tension, and when both pressures are equivalent, the volumetric viscosity is $\xi_k^V = +\infty$. In this particular case, elastic stresses provide the resistance to isotropic compression. The left-hand side of Eq. (49) refers to the averaged volumetric deformation, which can be inferred from the trace of the averaged strain-rate tensor in Eq. (A.15), since $\mathrm{tr}\left(\dot{\boldsymbol{\varepsilon}}_k\right) = \frac{\langle \chi_k \mathrm{tr}(\dot{\boldsymbol{\varepsilon}}) \rangle}{\phi_k} = \nabla \cdot \mathbf{v}_k$. In addition, $\mathrm{tr}\left(\boldsymbol{\sigma}\right) = -3P$ being a scalar, the objective derivative in the right-hand-side of Eq. (49) takes the form of a material derivative $\frac{\mathrm{tr}(\hat{\boldsymbol{\sigma}})}{3} = \frac{\mathrm{D}}{\mathrm{D}t} \frac{\mathrm{tr}(\boldsymbol{\sigma})}{3} = -\frac{\mathrm{D}}{\mathrm{D}t} P$. The same reasoning applies for the surface tension. As shown in section 2.7.2 for the deviatoric stress tensor, we estimate the averaged material derivative of pressure as the material derivative of the averaged pressure, bearing in mind the potential error associated with this assumption for compressible materials.

In order to constrain the pressure jump between phases we need to compare individual volumetric constitutive laws for two dynamic phases k and j at the interface. As mentioned in section 2.6, the contribution to the pressure difference is not evenly partitioned between the dynamic phases, since the partitioning of the pressure jump is also closely related to the physical properties (i.e. the molecular bond strength and viscosity) of the dynamic phases. As these properties vary among the coexisting phases, the pressure jump can not be uniformly divided over the mixture (simply weighted with ϕ_k). Following these considerations and in close analogy with section 2.6, we weight Eq. (49) with the surface energy partitioning coefficient ω_k and compare pairs of single volumetric constitutive laws. This procedure results in the following frame invariant visco-elastic constitutive law for the pressure difference between two (k and j) dynamic phases,

$$\omega_k \phi_k \nabla \cdot \mathbf{v}_k - \omega_j \phi_j \nabla \cdot \mathbf{v}_j = -\frac{\Delta P_{k,j} + \Theta_{k,j}}{\xi_{k,j}} - \frac{1}{K_{k,j}} \frac{\mathrm{D}_\omega}{\mathrm{D}t} \left(\Delta P_{k,j} + \Theta_{k,j} \right) \tag{50}$$

where $\xi_{k,j} = C_\xi \frac{\xi_k^V \xi_j^V}{\omega_j \xi_k^V + \omega_k \xi_j^V}$ and $K_{k,j} = C_K \frac{K_k K_j}{\omega_j K_k + \omega_k K_j}$ are both material invariant constants contain-

ing information on average volumetric compaction resistance (viscous and elastic, respectively), and $\Theta_{k,j} = \sigma\left(\omega_k \frac{\mathrm{d}\alpha}{\mathrm{d}\phi_k} - \omega_j \frac{\mathrm{d}\alpha}{\mathrm{d}\phi_j}\right)$ refers to the amount of surface tension held by both dynamic phases. C_ξ and C_K are first order dimensionless constants accounting for different interface geometries (Šrámek et al., 2007). Note that for a simple two-phase system $\Theta_{k,j} = \sigma\left(\omega_k \frac{\mathrm{d}\alpha}{\mathrm{d}\phi_k} + \omega_j \frac{\mathrm{d}\alpha}{\mathrm{d}\phi_k}\right) = \sigma \frac{\mathrm{d}\alpha}{\mathrm{d}\phi_k} = \sigma \frac{\mathrm{d}\alpha_{k,j}}{\mathrm{d}\phi_k}$, as expected. Equation (50) establishes a general relationship controlling the pressure drop between two coexisting phases, where the left-hand-side represents the volumetric deformation caused by the out-of-equilibrium pressure differences in the right-hand side, including phase change effects.

Following the same strategy as in the previous section, we include plasticity through the effective viscosity approach. Thus, the final visco-elasto-plastic volumetric constitutive law for pressure difference, $\Delta P_{k,j}$, reads,

$$\Delta P_{k,j} + \Theta_{k,j} = -\xi_{k,j}^{eff}\left(\omega_k \phi_k \nabla \cdot \mathbf{v}_k - \omega_j \phi_j \nabla \cdot \mathbf{v}_j\right) + \chi_{k,j}^{P} \Delta P_{k,j}^{0} \tag{51}$$

with

$$\xi_{k,j}^{eff} = \begin{cases} \frac{\Delta P_{k,j}^{y} + \Theta_{k,j} - \chi_{k,j}^{P} \Delta P_{k,j}^{0}}{\omega_k \phi_k \nabla\cdot\mathbf{v}_k - \omega_j \phi_j \nabla\cdot\mathbf{v}_j} & \Delta P_{k,j} = \Delta P_{k,j}^{y} \\ \frac{1}{\frac{1}{\xi_{k,j}} + \frac{1}{K_{k,j}\Delta t}} & \Delta P_{k,j} < \Delta P_{k,j}^{y} \end{cases}$$

$$\chi_{k,j}^{P} = \frac{1}{1 + \frac{K_{k,j}\Delta t}{\xi_{k,j}}}$$

where $\Delta P_{k,j}^{y}$ is the yielding pressure difference condition, and $\Delta P_{k,j}^{0} = \left(\Delta P_{k,j} + \Theta_{k,j}\right)^{0}$ is the advected pressure difference including surface tension effects.

Previous works on multiphase dynamics proposed different constraints for the pressure difference between phases. For instance, McKenzie (1984) employed a bulk viscosity dependent constitutive law for compaction stresses applied to the limiting case of two-phase flows (solid (s) and fluid(f)) with $\mu_s \gg \mu_f$. Alternatively, Fowler (1985) and Scott & Stevenson (1986) explicitly related compaction pressures to a difference between solid and fluid pressures throughout a porosity-dependent bulk viscosity. For small porosity values, all three formulations become equivalent (Ryan, 1990). On the other hand, Bercovici et al. (2001); Bercovici & Ricard (2003) obtained a material-invariant two-phase formulation with surface tension based on micromechanical models, where no explicit definition for the bulk viscosity was made. Later, Šrámek et al. (2007) provided additional thermodynamic rigour to Bercovici and Ricard's material-invariant theory. More recently, Keller et al. (2013) formulated a visco-elasto-plastic compaction rheology based on a Maxwell body analogue for a two-phase (melt-solid) system. The present work, however, combines material-invariant principles and ensemble averaging procedures in order to constraint Maxwell-type visco-elasto-plastic rheologies for a general

multi-phase system. Thus, our volumetric constitutive law differs from the abovementioned works in several ways. First, unlike McKenzie's (1984) and Keller's et al. (2013), our formulation is material-invariant, and thus it is not restricted to two-phase systems with $\mu_s \gg \mu_f$. Second, unlike Bercovici et al. (2001), the bulk viscosity for each dynamic phase naturally arises in Eq. (50) from the explicit assumption of a Newtonian isotropic viscous rheology. Thirdly, our model is fully visco-elasto-plastic. Correspondence between our formulation and previous works is, however, exact under certain assumptions. For the limiting case of two-phase viscous flows with $\mu_s \gg \mu_f$ and without surface tension, the compaction condition from McKenzie (1984) reads $\xi \nabla \cdot \mathbf{v}_s = -\Delta P_{s,f}$ where ξ is the bulk viscosity. Under the same assumptions, our model predicts $C_\xi \xi_s^V \phi_s \nabla \cdot \mathbf{v}_s = -\Delta P_{s,f}$. Therefore, allowing for $\omega_f \to 0$ as $\mu_f / \mu_s \to 0$ exactly recovers McKenzie's (1984) theory assuming that $\xi = C_\xi \xi_s^V \phi_s$. Under the same assumptions, Bercovici and Ricard's (2001) relation becomes $\frac{C_0 \mu_s}{\phi_f} \nabla \cdot \mathbf{v}_s = -\Delta P_{s,f}$ where C_0 is a first order constant, which is also in agreement with our formulation assuming that $\phi_s \xi_s^V = \frac{C_0}{C_\xi} \frac{\mu_s}{\phi_f}$. Lastly, in absence of motion and when two dynamic phases are considered, Eq. (50) recovers Laplace's surface tension equilibrium condition.

3 THERMODYNAMIC MODEL

The coupling among the thermo-mechanical-chemical system of equations is formally achieved by means of a thermodynamic model under the assumption of local thermodynamic equilibrium (we discuss the actual meaning of "local" in Section 6). Therefore, the main variables (P_k, $\mathbf{v}_k$, T, $\mathbf{c}^b$), physical properties (e.g. ρ_k, heat capacity c_k), phase abundances ϕ_k, and closure terms (e.g. $\Gamma^m_{k,j}$) are all related by fundamental thermodynamic rules. In addition to guaranteeing a thermodynamically-consistent coupling of the main field equations, the thermodynamic model provides a wealth of information that can be used to compare the results of simulations with observed data (e.g. seismic velocities, geochemical data, gravity data, etc). For instance, complete mineralogical assemblages, thermodynamic phase properties, dynamic phase properties and bulk system properties in every and any part of the model can be retrieved from the thermodynamic model. This is achieved by solving local Gibbs free-energy minimization problems "on the fly" as needed by the simulation. Our approach is therefore identical to that in Tirone et al. (2009).

The local minimization problem involves finding the amounts and compositions of the thermodynamic phases that minimize the Gibbs free-energy of the (local) system, at constant P-T, subject to mass balance constrains among the thermodynamic phases and the bulk composition of the system. This can be written as

$$G_{syst} = \sum_{i=1}^{i=np} \alpha_i G^i = min$$
$$\text{subject to} \quad \mathbf{b}_j = \mathbf{A}_{ji}\alpha_i \tag{52}$$
$$\text{and} \qquad \alpha_i \geqslant 0$$

where np is the total number of phases coexisting in equilibrium, G^i the molar Gibbs energy of phase i, α_i the molar amount of phase i, $\mathbf{b}_j$ the bulk composition vector, and $\mathbf{A}^b_{ji}$ is the coefficient matrix containing the equilibrium composition of each phase i (i.e. amount of j component in the ith phase). Following a conventional chemical thermodynamic formulation, the molar Gibbs free energy of a thermodynamic phase (i.e. phase component) G^i is given as the sum of three contributions: a mechanical mixture contribution G^i_{mech}, an ideal solution contribution G^i_{ideal} and a non-ideal or "excess" contribution $G^i_{non-ideal}$

$$G^i = G^i_{mech} + G^i_{ideal} + G^i_{non-ideal} \tag{53}$$

where

$$G^i_{mech} = \sum X^i_j G^{i0}_j \tag{54}$$

$$G^i_{ideal} = RT \sum X^i_j ln X^i_j \tag{55}$$

$$G^{i0}_j = H_0 + \int_{T_0}^{T} Cp\, dT - T\left[S_0 + \int_{T_0}^{T} \frac{Cp}{T}\, dT\right] + \int_{P_0}^{P} V\, dP \tag{56}$$

where X^i_j is the molar fraction of phase component j in phase i and G^{i0}_j is the molar free energy of pure component j in phase i. In Eq. (56), H_0 and S_0 are the molar enthalpy and entropy of pure phase component j at standard conditions of temperature and pressure (normally $T_0 = 298$ K and $P_0 = 1$ bar), Cp the heat capacity at constant pressure and V the molar volume. Heat capacity as a function of temperature is typically tabulated as a polynomial (Holland & Powell, 1998), whereas the volume has to be described using an equation of state (EoS). The non-ideal term in Eq. 53 takes different expressions depending on the model used to account for departures from ideality, but it is

generally modelled as either a polynomial or a power series of the mole fraction (e.g. Margules or Redlich-Kister models; c.f. Holland & Powell (2003); Ganguly (2009)).

The thermodynamic information necessary to solve the minimization problem in Eq. (52) for j-component systems can be extracted from internally-consistent thermodynamic databases (e.g. Berman, 1988; Ghiorso & Sack, 1995; Holland & Powell, 1998). The actual optimization method used to find the minimum of the system's Gibbs free energy is discussed in the next section.

4 NUMERICAL/IMPLEMENTATION OVERVIEW

4.1 Mechanical problem

The mechanical problem is solved in order to obtain velocities $\mathbf{v}_k$ and pressures P_k for each dynamic phase. We use the mixed finite-element formulation to solve the coupled system formed by an individual, quasi-stationary, Stokes-type momentum Eq. (17) for each dynamic phase, together with a total mass conservation equation (Eq. (14)) and $k-1$ pressure-difference equations (Eq. (51)). Therefore, for a general N-phase problem, we have a total of $N+1+(N-1)$ equations and $2\times N$ unknowns. The solvability of the system depends on a proper choice of finite-element spaces for the velocity and pressure interpolation, due to the saddle-point nature of the variational problem (Donea & Huerta, 2003). We use an extended Taylor-Hood Q2-(Q1+Q0) element (continuous quadratic velocity, discontinuous linear pressure), which is proven to satisfy the LBB condition (Arndt, 2013) and minimize shear locking in elasticity problems (see Appendix C).

The non-linearities arising from the effective viscosity approach and the stress dependent variables are solved through an inner fixed-point iteration loop (Zienkiewicz & Taylor, 2000) assuming that physical properties and mass-transfer rates remain constants within this inner loop. The advection and rotation of stresses is dealt with passive markers, and the stresses are recovered using Global Smoothing (Hinton & Campbell, 1974) (other methods such as the Superconvergent Patch Recovery method (Zienkiewicz & Zhu, 1992) have also been implemented).

The reader is referred to Appendix B for further details on the numerical implementation of the mechanical problem, including FE discretization and the particle-based stress treatment.

4.2 Thermal problem

The thermal problem stated in Eq. (23) requires a double time-space discretization in order to obtain the temperature at every point in time and space. Given the presence of sharp gradients and the need to advect them over many time steps, an accurate and stable advection-diffusion algorithm is required to avoid numerical oscillations or excessive numerical diffusion. Here we use the particle-based

Lagrangian-Eulerian formulation of (Oliveira et al., 2016), which combines a Lagrangian formulation for the advective part and an Eulerian-based heat source method for the diffusion and heat sources. This method employs a fixed structured quadrilateral finite-element Eulerian grid and a single set of Lagrangian particles for the temperature advection. We use linear quadrilateral elements together with an implicit second order Crank-Nicolson time discretization for the Eulerian approach, whereas the Lagrangian advection is solved using a fourth-order Runge Kutta scheme (RK4). We have also designed an effective interpolation scheme to transfer temperature information from nodes to particles and back at every time step. (Oliveira et al., 2016) showed that the method is high-order, accurate, oscillation-free and applicable to a wide range of fully-coupled advection-diffusion-reaction problems (see Appendix C).

4.3 Reactive transport

We solve Eq. (29) in order to track the evolution of the bulk chemistry of our system. Here we use the same Lagrangian-Eulerian numerical method as for the thermal problem (Oliveira et al., 2016). The chemistry (in weight percent) is defined in a single moving set of particles, which updates its values along the trajectory of the particles via interpolation of the divergence computed at the nodes of the grid. However, unlike temperature, chemical mass is a conserved quantity and therefore conservation needs to be ensured in time and space. Our numerical treatment of the right-hand side of Eq. (29) at the particles verifies that $\sum_b c^b = 1$ over all the particles and at every time step (see section 2.5 and (Oliveira et al., 2016)).

4.4 Thermodynamic solver

Since Eq. 53 is a non-linear function of composition, searching for the absolute minimum Gibbs free energy of the system can be challenging and subject to convergence problems. Here we overcome such problems by adopting the "pseudocompound strategy" (Connolly & Kerrick, 1987; Connolly, 2005), where the non-linear chemical potential is approximated as a series of stoichiometric (i.e. fixed composition) pseudocompounds; this transforms the non-linear problem into a linear one that can be solved by efficient and robust linear programming techniques (e.g. Simplex algorithm). In this way, the solution is represented by a linear combination of pseudocompounds weighted by their respective weight fractions (more details in Connolly & Kerrick (1987)). Although the quality of the solution and the time that it takes to solve the minimization problem depend strongly on the number of pseudocompounds used to discretize the compositional space, efficient adaptive strategies are available (Connolly, 2009).

Since thermodynamic information is required by FEM computations at Gaussian points, it is desirable

to solve the minimization problem at the integration points. This implies that, for a simple 100×100 element 2D problem with a 2×2 quadrature, a total of 4000 linear programming minimizations per iteration in a single time step need to be computed. However, minimization problems are perfectly parallelizable, rendering the procedure practical when cluster-computing is available. Moreover, we note that in many problems of geodynamic interest, only a reduced portion of the numerical domain experiences dynamic phase changes (e.g. melting), whereas the rest of the domain stays in a "single phase" state. In this case, we can solve minimization problems in those regions where dynamic phases interact and use a *static* approach (i.e. precomputed properties) elsewhere in the domain. Such a combination of dynamic and static approaches can significantly reduce the computation time associated with the minimization problem, especially when tensor-rank decompositions are used for the static approach (Afonso et al., 2015).

Besides basic thermodynamic information on solution (or activity) models and solution end-members, the input for the minimization problem are pressure, temperature and bulk composition. Given our assumption of thermal equilibrium, the input temperature coming from the solution of the thermal problem is well defined. Pressure, on the other hand, is more problematic since in principle different dynamic phases can experience different pressures at equilibrium and therefore the use of a single pressure in the thermodynamic problem is inconsistent. However, for the purposes of this study, the difference in pressure between phases in local equilibrium can be considered small (identical if there is no surface tension) compared to the absolute pressures. We therefore use the average of the mechanical pressures, $\mathcal{P} = \sum_k \phi_k P_k$, as a representative total pressure in solving the minimization problem. A different approach, where dynamic phases are not considered to be in equilibrium with each other, is discussed in Section 6.1.

4.5 Coupling scheme

The four problems described above are highly coupled via e.g. advective terms in the energy and reactive transport equations, energy dissipation terms as functions of velocity, and the P-T-composition-dependent physical properties. More importantly, both the mechanical and thermal problems involve closure terms, which are outputs of the thermodynamic solver. The coupling scheme used in this study is outlined below for a single time step

(i) Retrieve initial set up from the previous time step n. This includes velocities $\mathbf{v}_k^n$, pressures P_k^n, temperature T^n, chemical composition $\mathbf{c}^n$, phase abundances ϕ_k^n, physical properties $prop_k^n$ and mass-transfer rates $\left(\Gamma_{k,j}^m\right)^n$.

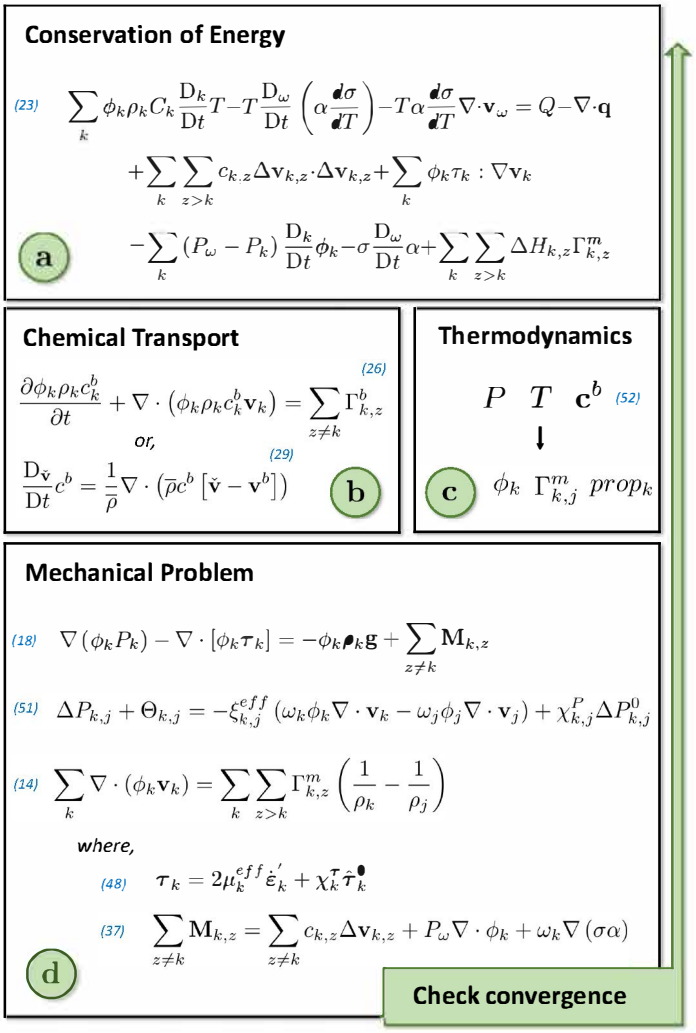

Figure 5. Numerical scheme workflow. Equations are referenced as in the text (in brackets).

(ii) Assume velocities $\mathbf{v}_k^{n+1} = \mathbf{v}_k^n$, pressures $P_k^{n+1} = P_k^n$, properties $prop_k^{n+1} = prop_k^n$ and mass-transfer rates $\left(\Gamma_{k,j}^m\right)^{n+1} = 0$ in order to start the non-linear iterations (Fig. 5).

(a) Solve the thermal problem and obtain T^{n+1}.

(b) Solve the reactive transport problem and obtain $\mathbf{c}_b^{n+1}$.

(c) Obtain new properties $prop_k^{n+1}$ and closure terms $\left(\Gamma_{k,j}^m\right)^{n+1}$ from the thermodynamic solver using T^{n+1} and $\mathbf{c}_b^{n+1}$.

(d) Solve the mechanical problem for $\mathbf{v}_k^{n+1}$ and P_k^{n+1}. This requires inner iterations to accommodate stresses (only needed if plasticity is used).

(e) Go to step (ii)(a) if convergence of velocities and temperatures is not reached.

(iii) Check time and go to (i) for the next time step.

5 NUMERICAL EXAMPLES

In this section, we present some simple, yet illustrative, numerical examples that highlight some of the capabilities of our numerical scheme for general cases of partial melting. The first example illustrates some differences that arise from incorporating a thermodynamically-consistent approach into a two-phase model relative to a case where no thermodynamic consistency is enforced. The second example explores the behaviour of a thermally-driven upwelling experiencing partial decompression melting. To keep the analysis tractable and focus on the major features of the model, we restrict ourselves to the case of systems made up entirely of olivine (i.e. a single solid solution). A more thorough analysis, including more realistic mineralogies, will be presented in a forthcoming publication. A number of numerical benchmarks use to validate our numerical scheme are presented in Appendix C.

5.1 Melt extraction from host matrix

This experiment explores the effect of various parameters on the extraction of melt from the host matrix. All the models are run in a 600 km wide and 400 km deep rectangular box discretized with 241 x 161 nodes, respectively. The initial background composition is spatially homogeneous with equal amounts of FeO and MgO (i.e. olivine #Mg = 0.5). The temperature structure is shown in Fig. 7A. The viscosities of both the solid and fluid phases are considered constant; $\mu_s = 10^{20}$ and $\mu_f = 1$. Results for a single time step are shown in Fig. 7D-F, 8 and summarized in Table 3. Velocity vectors in Figs 7 and 8 are normalized by the local maximum velocity, whereas those shown in Table 3 represent absolute magnitudes.

Figure (7 - A (right), B and C (right) show, respectively, the thermodynamically-consistent melt content, the solid's density and the density difference between solid and fluid phases that results from the imposed T-P-composition conditions. Note that the background pressure field is gravitational, and since it depends on density, it needs to be computed iteratively in order to obtain a consistent initial configuration. As expected, melt is more abundant in regions where the temperature is higher. The olivine phase diagram (Fig. 6) predicts that the solid phase becomes progressively more depleted in FeO as melting proceeds, which contributes to lower the density of the solid in regions where melt is present (Figure 7 - B). Despite its higher relative iron content (Figure 6), the melt remains lighter than the surrounding solid (Figure 7 - C; left), but it becomes denser in regions of higher melt content, as the solid phase becomes more depleted in FeO (i.e. lighter) whereas the opposite occurs in the melt phase. For comparison, we also compute results for a thermodynamically non-consistent scheme in which the

melt density is forced to be $\%90$ that of the solid everywhere, resulting in maximum $\Delta\rho \approx 400$ kg/m^3 (Fig. 7C; right) (e.g. $\Delta\rho \approx 500$ in Sparks & Parmentier (1991); Keller et al. (2013)). Both simulations are thus identical except for the way melt densities are computed.

Figure 7-D-E-F show pressure differences ($P_s - P_f$) for both consistent (left) and non-consistent (right) schemes; normalized melt extraction velocity vectors for different values of the interaction coefficient c are also plotted. Since melt extraction by percolation is affected (among other factors, see Eq. (18)) by the density contrast between solid and fluid phases, significant differences in the dynamics of the system arise when comparing the consistent and non-consistent schemes. We observe pressure differences up to one order of magnitude higher for the non-consistent scheme. Due to the higher density difference in this case, the fluid experiences a stronger overpressure in the upper region of the melt zone in comparison to the thermodynamically-consistent scheme. This can cause up to a factor of 4 difference in relative velocities (rows 5 and 6 in table 3) between the two schemes. We can also expect that discrepancies in melt extraction velocity will become larger as the system evolves, mainly due to rheological weakening of the host matrix in overpressured zones (plastic tensile failure, Keller et al. (2013)). Furthermore, the lower (max. $\Delta\rho \approx 70$ kg/m^3) and spatially non-uniform density difference predicted by the consistent scheme results in significantly different fluid velocity fields (relative to the solid) within the partially molten region, especially for low values of the interaction term c (i.e. high permeability; Fig. 7-D).

The importance of the interaction term c on melt migration has been reported in previous works (McKenzie, 1984; Ni & Beckermann, 1991) and it is confirmed here. We run several numerical experiments for increasing values of interaction coefficient ($c_{s,f} = \{10^9, 10^{10}, 10^{11}\}$), which correspond to porosity-independent permeabilities of $k_0 = \{10^{-9}, 10^{-10}, 10^{-11}\}$, respectively (i.e. exponential factor of permeability $n = 2$). Since $c\Delta\mathbf{v}$ controls the viscous mechanical interaction between phases (Eq. (37)), we expect smaller velocity differences for larger interaction coefficients. Not only the absolute velocity magnitudes of the melt and solid phases, but also the direction of melt extraction velocities are affected by this constant (Fig. 7-right panels and rows 1-4 in table 3). As expected, lower values of $c_{s,f}$ (i.e. higher permeability) lead to higher relative velocities, and thus a more efficient melt extraction mechanism. On the contrary, higher values of $c_{s,f}$ result in smaller relative displacements between both phases. This will be discussed further in the next example.

Table 3 also includes results from simulations in which a constant background extensional strain-rate of $\dot{\varepsilon} = 10^{-14}$ s^{-1} was imposed. When compared with identical simulations with no extensional strain-rate (and removing the background extensional component from the resultant velocity field), no apparent effect is observed in the melt extraction pattern. This seems counterintuitive at first glance, as imposed background strain-rates are known to play a key role in the segregation and organization

of melt transport (e.g. Holtzman et al., 2003); (Katz et al., 2006). However, this is simply due to the fact that constant viscosities were used in this numerical example, whereas non-Newtonian viscosities are needed in order to observe any difference between the two cases (Katz et al., 2006).

Lastly, Fig. 8 compares results from our thermodynamically-consistent scheme with and without surface tension effects for the particular case where $c = 10^9$. As discussed in section 2.6, surface tension is related to the abundance and morphology of the interfaces via its surface area density (Eq. (32)). For the particular definition given in Eq. (32), surface tension can be modelled as a function of parameters α_0, a and b. Although for illustrative purposes these parameters can be considered constants, they are actually related to the microstructure of the two-phase assemblage (Bercovici et al., 2001; Boettinger et al., 2002; Sun & Beckermann, 2004) and therefore more realistic formulations would be necessary when modelling actual processes. Figure 8-A shows the solid phase velocity vectors and surface area densities for two cases: $i)$ $\alpha_0 = 10^6$, $a = b = 0.5$ and $ii)$ $\alpha_0 = 10^6$, $a = 0.1$, $b = 0.9$. The former corresponds to a simple hexagonal tubular network (Ricard et al., 2001, and references therein) whereas the latter is perhaps more representative of real silicate melts at low porosities (e.g. Bercovici et al., 2001). At first glance, different surface tension configurations seem to have little or no effect on the dynamics of the system. However, a closer look at the solid velocities reveals some interesting features. Figure 8-B (left) compares the vertical velocities of the solid phase between case $i)$ and an identical simulation without surface tension. This figure shows an increase in vertical velocities in zones where melt is overpressured (upper region of the melt zone) and a decrease in vertical velocities in the lower parts of the melt zone. This is a direct consequence of the effect of surface tension curvature, $\frac{\mathrm{d}\alpha}{\mathrm{d}\phi}$, on the pressure difference between the solid and fluid phases (Eq. (51)). Another way to see this is by considering the divergence of the solid velocities, which is larger in the middle of the melt region when surface tension curvature effects are included. In other words, surface tension has an effective *expansive effect* over the solid phase, which causes the above velocity differences (positive in the upper region, negative in the lower region). This effect is more pronounced when comparing cases $i)$ and $ii)$, as seen in Fig. 8-B (right).

5.2 Upwelling and melting driven by thermal instability

This example solves a transient two-phase (solid (s) - fluid (f)) multi-component reactive transport problem for the simple case of a viscous olivine solid solution with homogeneous initial composition. The experiment is run in a 300×200 km box (only half of the plume is computed) discretized with 121×181 nodes and 540,000 randomly distributed Lagrangian markers (∼25 particles per element). The main model features are: (1) uniform initial bulk composition of Mg# = 0.5, (2) constant viscosities ($\mu_s = 10^{20}$ $\mu_f = 1$), (3) viscous interaction coefficient $c_{s,f} = 1/k_0$, where $k_0 = 10^{-11}$ Pa s is

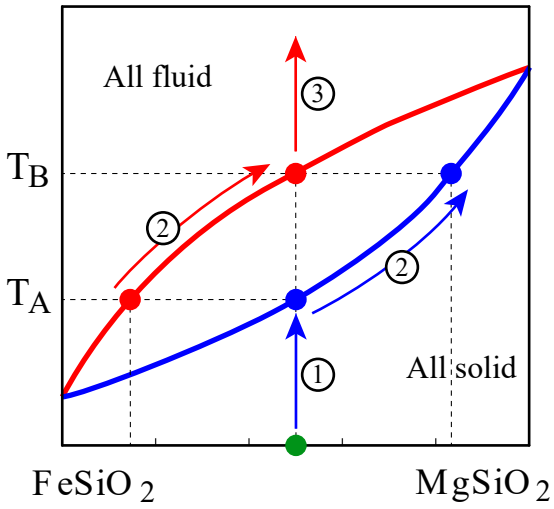

Figure 6. Phase equilibria diagram for a simple olivine binary solution. Blue and red lines represent the solidus and liquidus respectively. Numbers in phase diagram correspond as follows. 1) initially everything is solid with #Mg = 0.5. 2) first melt is formed as $T > T_A$. To determine the composition of both solid and fluid phases move horizontally across the diagram to the solidus and liquidus lines, respectively. As the temperature increases the composition of the solid and fluid phases migrate up the solidus and liquidus lines (decreasing iron content). 3) If $T > T_B$ everything is fluid with #Mg = 0.5.

the permeability constant, (4) free-slip mechanical boundary condition at the left and top boundaries; no-slip at the bottom and right boundaries, (5) fixed temperature at the bottom and top walls, and (6) initial temperature field with a thermal anomaly in the bottom left corner given by,

Table 3. Results from the melt extraction experiment for various case studies for the node with higher melt content.

		$c = 10^9$		$c = 10^{10}$		$c = 10^{11}$	
		$\dot{\varepsilon} = 0$	$\dot{\varepsilon} = 10^{-14}$	$\dot{\varepsilon} = 0$	$\dot{\varepsilon} = 10^{-14}$	$\dot{\varepsilon} = 0$	$\dot{\varepsilon} = 10^{-14}$
Abs. Solid	Cons.	8,026E-9	8,033E-9	8,451E-9	8,458E-9	8,937E-9	8,942E-9
$[v_s^y]$	N-Cons.	3,203E-9	3,211E-9	7,603E-9	7,61E-9	1,305E-8	1,305E-8
Abs. Melt	Cons.	1,844E-8	1,844E-8	1,181E-8	1,181E-8	9,575E-9	9,577E-9
$\left[v_f^y\right]$	N-Cons.	6,282E-8	6,282E-8	4,02E-8	4,02E-8	2,063E-8	2,063E-8
Rel. Diff	Cons.	0,5647	0,5643	0,2844	0,2838	0,06669	0,06632
$\left[\frac{v_f^y - v_s^y}{v_f^y}\right]$	N-Cons.	0,949	0,9289	0,8109	0,8107	0,3677	0,3675

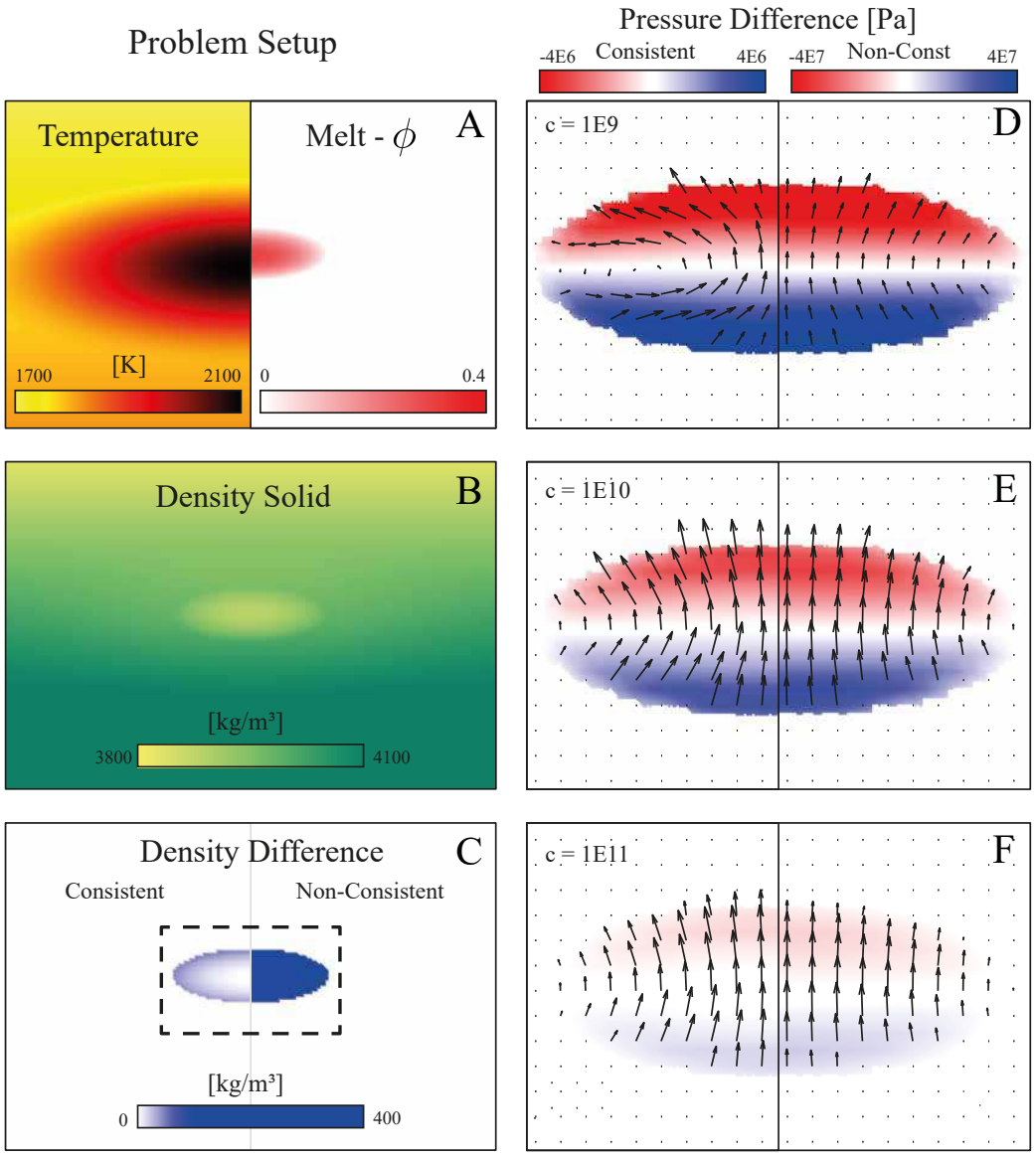

Figure 7. Melt extraction from host matrix with and without a thermodynamically-consistent scheme for a system made up of olivine with Mg#=0.5. Left panels (A-C) display the problem set up, including (from top to bottom) temperature field, melt content, bulk density of solid phase and density difference ($\rho_s - \rho_f$) for both consistent and non-consistent cases. Right panels (D-F) compare pressure differences ($\Delta P = P_s - P_f$) between the consistent (left) and non-consistent (right) cases for increasing values (from top to bottom) of the interaction term (corresponding to decreasing values of permeability); normalized melt extraction velocity vectors ($\frac{\mathbf{v}_f - \mathbf{v}_s}{\mathbf{v}_{max}}$) are also shown.

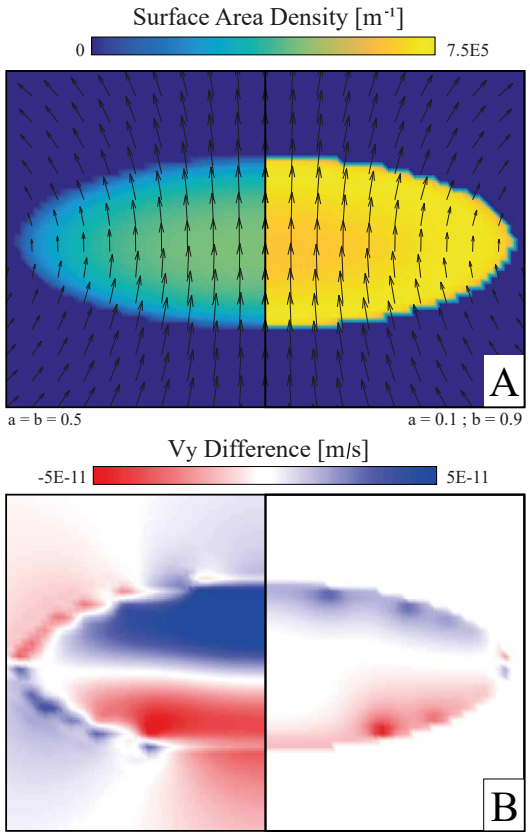

Figure 8. Surface tension effects on the solid velocity for the melt extraction problem in Fig. 7. A-left: surface area density computed with $a = b = 0.5$. A-right: surface area density computed with $a = 0.1$ and $b = 0.9$. Solid velocity vectors are also plotted. B-felt: absolute difference in the solid's vertical velocity (v_y) between the case in A-left and an identical simulation without surface tension. B-right: absolute difference in v_y between the cases in A-left and A-right (as $v_y^B - v_y^A$).

$$
\begin{aligned}
T(x,y) =& T_{ref} && \text{if } r(x,y) > 1 \\
T(x,y) =& T_{ref} + 100\left[1 + \cos\left(\pi \min\{r(x,y);1\}\right)\right] && \text{if } r(x,y) \leq 1 \\
\text{where,} \quad & r(x,y) = 1.5\sqrt{\left(\frac{x}{2E5}\right)^2 + \left(\frac{y}{1E5}\right)^2} \\
& T_{ref} = \frac{T_{top} - T_{bot}}{3E5}\left(y - 3E5\right) + T_{top} \\
& T_{top} = 1810 \\
& T_{bot} = 1900
\end{aligned}
\tag{57}
$$

For the above initial conditions, the thermodynamic problem predicts that the numerical box is occupied entirely by solid olivine. The initial temperature field, however, results in a lower density zone

around the bottom left corner that triggers upward advection. As the thermal plume enters lower pressure zones, it starts experiencing decompression melting (at ∼7.6 Ma). Figure 9 and 10 display the thermo-chemical evolution of the system at different times.

Thermodynamic consistency is apparent when comparing A, B, C, E and F in Fig. 9. The difference in chemical composition between solid and melt is perhaps better illustrated in E and F, where the relative oxide composition (e.g. FeO, MgO and SiO_2) of both phases is depicted along the plume's symmetry axis. Partial melting (B) causes a drop in the FeO content of the solid phase (E), which is reflected in a higher Mg# number and an associated decrease in density (A). As expected for this binary system, we observe the opposite behavior in the melt phase (C and F). Despite the relative higher FeO content of the melt (F), Fig. 9-D shows a positive density difference $\rho_s - \rho_f$ in the entire region of partial melting, which results in a negative vertical buoyancy flux difference $\Delta B_y = (\rho_s v_s) - (\rho_f v_f)$. In other words, the melt is initially lighter than the surrounding solid and therefore contributes positively to the upward velocity of the plume (D-left panel).

As the plume reaches shallower depths (9 Ma), significant compositional variations in both solid and melt phases are observed (Fig. 9-G-L). Both phases behave similarly: they are lighter in regions with higher temperature (head of the plume) and lower FeO content (i.e. higher Mg#), and denser in regions of lower temperature (margins of the plume) and higher FeO content (i.e. lower Mg#). However, due to the lower ambient pressures and the larger differentiation (mainly FeO partitioning) experienced by the phases, the melt now becomes denser than the solid in the inner, hotter parts of the plume (J-red color zones), whereas the solid remains denser in the outer regions (J-blue color), where temperatures and melt fractions are smaller. The maximum density difference is ∼50 kg/m^3. Despite this heterogeneous density field, ΔB_y (J) indicates a faster ascend of the melt phase relative to the solid inside the plume (fig. 9 mid-bottom panels), although the absolute magnitude of ΔB_y tends to increase in those regions where the melt is denser. This is related to the fact that the solid matrix deformation (i.e. compaction) overcomes the local effect of the melt's negative buoyancy. Note that ΔB_y is significantly larger ($\sim$ an order of magnitude) than that in (D), resulting in an increasingly faster transport towards the surface and a consequent increase in melt production.

Melting in our simulations occurs in response to changes in the three main thermodynamic variables, namely temperature, pressure and composition. Melting by increasing temperature or decreasing pressure is standard practice in geodynamic simulations. Melting by changing the bulk composition of the system, on the other hand, is less common. In our simple olivine example, this occurs when the FeO-rich melt is advected into a solid parcel with a smaller Mg# (more depleted) and reacts (equilibrates) with it, thus effectively producing a metasomatic effect. This, in turn, can produce additional melting in the parcel, even without changing the temperature or pressure, as the solidus of its new

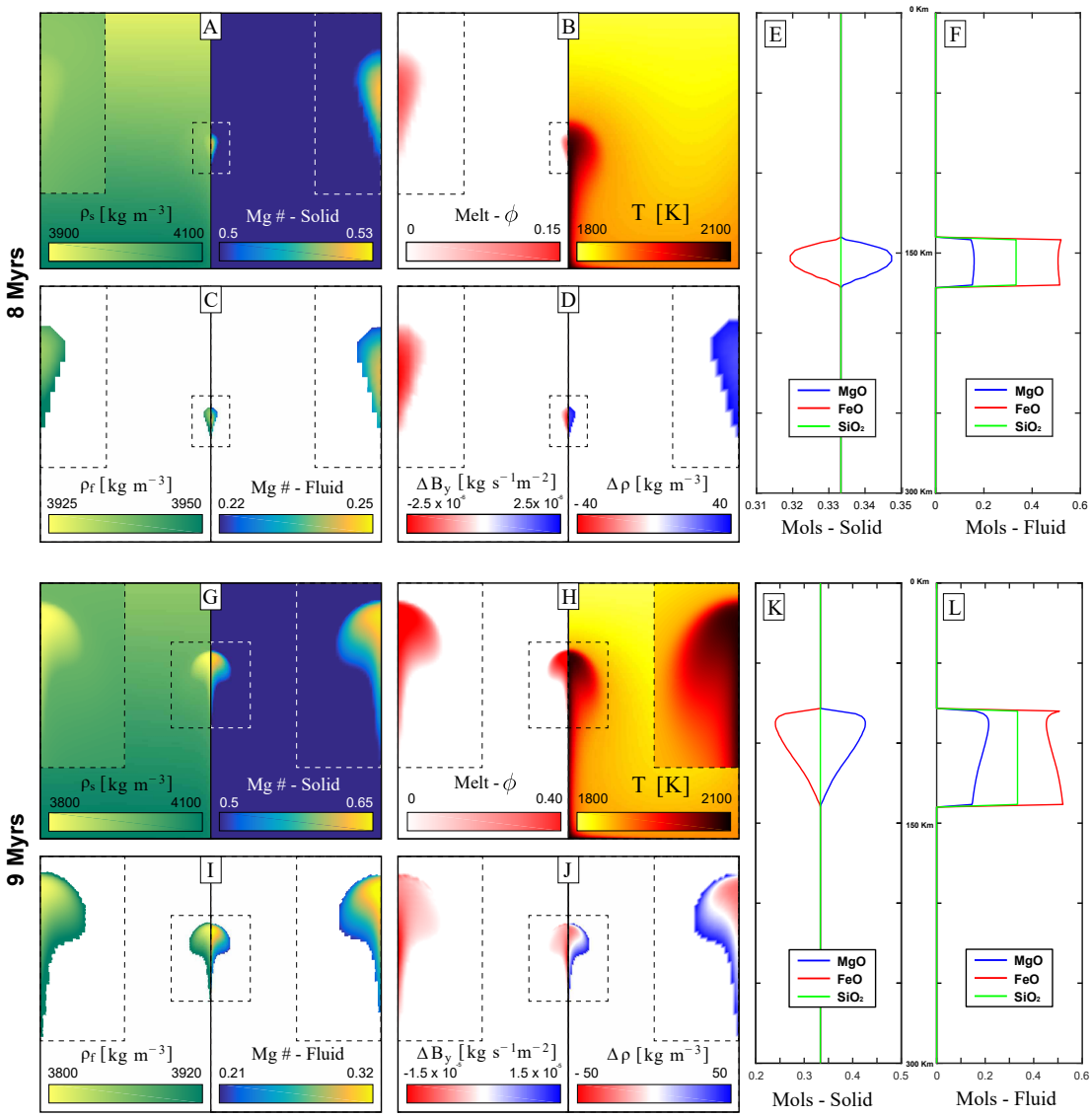

Figure 9. Snapshots of the thermal upwelling example for an olivine solid solution after 8 Ma (A-F) and 9 Ma (G-L). For clarity, areas of interest have been zoomed in. The zig-zag contours in the zoomed-in panels in C and D are plotting artifacts due to the way in which the fluid's information is extracted from the Eulerian mesh.

more fertile bulk composition is lower than that before metasomatism (Fig. 6). In reality, most steps in a simulation involve simultaneous changes in temperature, pressure and composition coupled with different velocity fields for the different phases.

Figure 10A-D show snapshots of melt content and temperature field for the same simulation as in Fig. 9, but at times of 9.1, 9.3, 9.5 and 9.7 Ma, respectively. Details on the relative velocity field (computed as $\mathbf{v}_f - \mathbf{v}_s$) within the melt region are shown in Fig. 10E-H, including the horizontal solid velocity

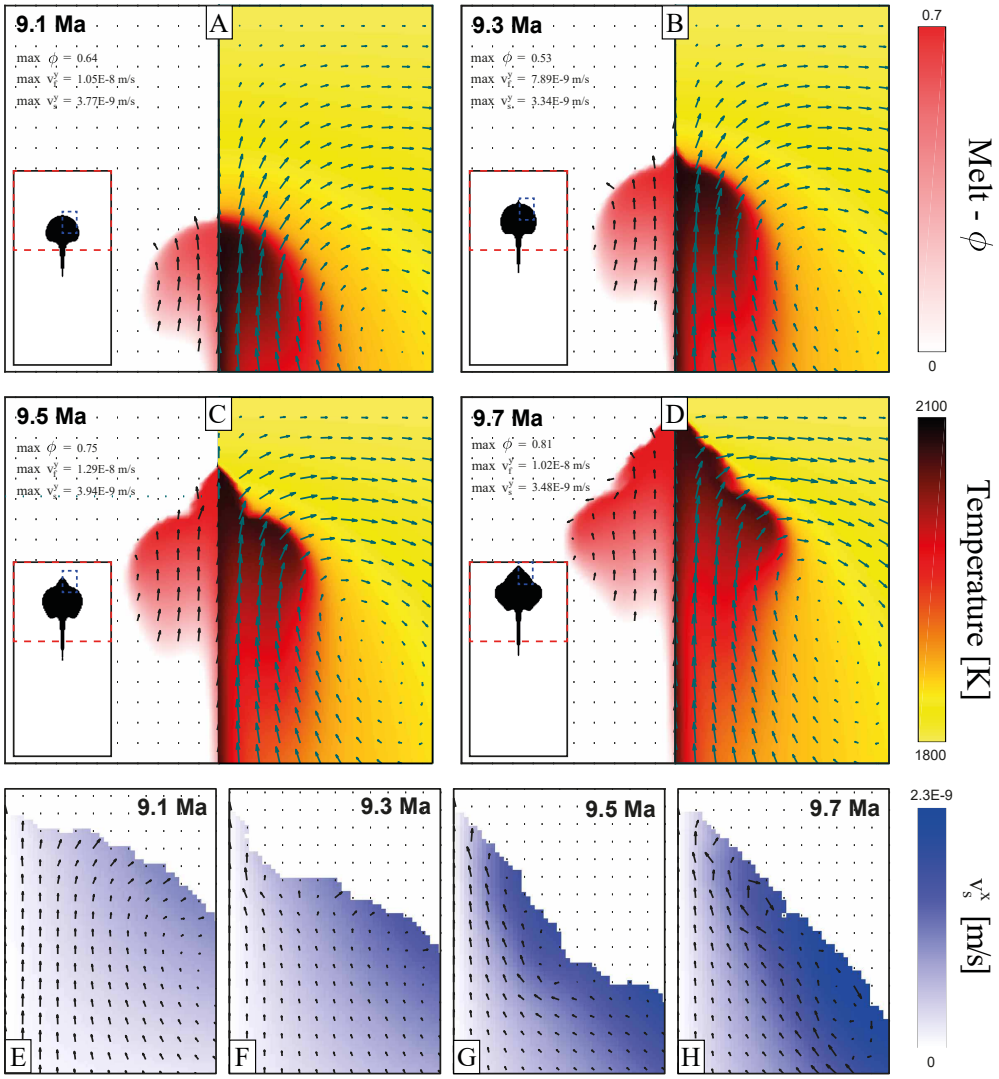

Figure 10. Snapshots of the example in Fig. 9 after 9.1, 9.3, 9.5 and 9.7 Ma. Upper panels (A-D) illustrate melt content (left), temperature field (right) and fluid/solid velocity vectors. Bottom panels (E-H) show the x-component of the solid velocity (as background colour) with melt extraction velocity vectors ($\mathbf{v}_f - \mathbf{v}_s$) for the four snapshots in A-D. Velocity vectors have been normalized with the maximum velocity in each panel.

component as a background color map. As the melt fraction increases, the energetics and dynamics of the two-phase system becomes progressively controlled by the fluid's behaviour. In the sequence shown in Fig. 9, the plume begins to interact with the rigid upper boundary, its vertical velocity begins to decrease, and a clear lateral deflection of the solid flow (i.e. horizontal spread of the plume head) is observed. The overpressured melt phase at the top of the plume, on the other hand, is expelled upwards and carries a significant portion of the system's heat content with it. At the same time, this

melt metasomatizes the colder and less fertile material at the top of the plume, triggering more melting. In particular, a "secondary plume" is developed around 9.3Ma at the top of the primary plume, where the higher melt velocities and higher melting rates occur. This secondary plume increases in size over a short time period (C-D) and generates a high melt-content zone ($>70\%$). Figure 10E-H shows that when this secondary plume develops, melt is preferentially focused towards its centre. This effect would be accentuated in a mid-ocean ridge environment and in simulations with stress-dependent viscosities (Kelemen et al., 1997, and references therein). At around 9.7 Ma, the chilled margins (melt solidifying) of the secondary plume trigger internal small-scale convection cells (evident in the irregular margins in Fig. 10D and in the velocity vectors in Fig. 10H).

We end this section by recalling that for small melt fractions, both phases are strongly coupled and it is the velocity of the solid phase that dictates the energetics of the system, which ultimately (together with pressure and composition) controls whether melting/solidification will occur. For larger melt fractions, however, the phases become more uncoupled and the physical properties of both melt and residual solid (and therefore the system as a whole) become progressively controlled by the composition and mechanical properties of the migrating melt (Spiegelman, 1993b)). At these stages, formulations that obtain the fluid velocity field as a post-process of the solid velocity field become questionable, and more general formulations where the velocity field of each phase is explicitly modelled (as in this study) may prove more useful. However, a more realistic formulation for the mechanical behaviour of disaggregated systems dominated by high melt fractions would be required.

6 DISCUSSION

Although the framework presented in this work is general and can be used to model a wide range of processes, some of the assumptions/methods used in the illustrative examples are rather simplistic and/or restrictive. In the following, we briefly discuss the implications of such choices as well as different ways of implementing more realistic ones.

6.1 Local thermodynamic equilibrium

An important hypothesis used throughout this work is that of local thermodynamic equilibrium (LTE). However, different meanings can be assigned to this hypothesis depending on the context. Strictly speaking, LTE is the fundamental assumption behind the classical theory of irreversible thermodynamics, also known as Classical Irreversible Thermodynamics (CIT); it states that even in systems out of (global) equilibrium, thermodynamic relations defined in equilibrium thermodynamics can be used locally and instantaneously (c.f. Lebon et al., 2008). Conceptually, the global system is split into

"small", local subsystems that are large enough to be considered independent macroscopic thermodynamic subsystems, but sufficiently small that thermodynamic equilibrium is always realized (or close to being realized). For large-scale systems that are not too far from equilibrium, CIT is known to be a good approximation and provides the theoretical support to the classical transport equations of mass, energy and momentum, as well as their coupling terms (c.f. Lebon et al., 2008; De Groot & Mazur, 2013). The framework presented in this work is therefore based on the principles of CIT.

A slightly different meaning can be given to the hypothesis of LTE when considering the actual numerical method to solve the transport equations. We refer to this particular meaning as the "numerical" LTE. In this case, not a conceptual but a real spatiotemporal discretization needs to be adopted, which depends on the scales of interest for the problem at hand. The question therefore is what are the spatial and temporal scales at which the system can reach equilibrium and how do they compare to the actual discretization scales used in solving the transport problem? Simply put, numerical LTE in our finite-element context means that equilibrium (chemical, thermal, mechanical, etc) is assumed to be always achieved within a volume equal or smaller than that of the finite element in a time smaller than the time step used in the simulation (e.g. Knapp, 1989; Tirone et al., 2009). Using standard values for thermal and chemical diffusivities, it can be shown that typical equilibrium scales are $\lesssim$ 100-200 m and $\lesssim$ 200-500 years (e.g. Knapp, 1989; Tirone et al., 2009).

The above equilibrium scales are smaller than typical discretization scales in geodynamic/melting scenarios, suggesting that the numerical LTE assumption is appropriate e.g. in large-scale simulations of slow porous flow. This assumption, however, may breakdown in the simulation of smaller scale or fast segregation processes (i.e. phases are said to be "decoupled") for which the time-spatial scale for equilibrium is larger than the time-spatial scale of interest. Our framework can be readily extended to deal with these cases, for example, by either adding separate energy and mass-diffusion equations (and interaction terms) for each phase to the system of conservation equations, and/or by explicitly considering that different dynamic phases can be in relative disequilibrium. In the latter case, we need to either compute (e.g. considering kinetics) or assume (e.g. as in fractional melting) how much of each phase can equilibrate with the other and solve separate thermodynamic minimization problems for each phase. These modifications can be important for the modelling of out-of-equilibrium thermochemical processes such as melt channeling (e.g. Spiegelman & Kelemen, 2003), disequilibrium melting (e.g. Iwamori, 1993; Elliott & Spiegelman, 2003), and kinetics-controlled processes in general. The details of such implementations are outside the scope of this work and will be presented in a separate publication.

6.2 Darcy equation, momentum interaction term and interfaces

A common practice in two-phase flows is to choose the interaction coefficient c in such a way that the momentum equation for the fluid phase recovers Darcy's law when $\mu_f \ll \mu_s$ and in absence of surface tension. The validity of Darcy's law has been, however, challenged in recent years, primarily based on theoretical works where thermodynamic properties are attained to interfaces (Hassanizadeh & Gray, 1979b, 1993; Gray & Hassanizadeh, 1998; Joekar-Niasar et al., 2010). Indeed, Darcy's law was originally developed for simple 1D steady-state isothermal flow experiments concerning almost incompressible water in saturated homogenous isotropic rigid sandy soils. While these assumptions are reasonable for single-phase flow, one may expect many other factors to affect the dynamics of MPMCRT systems. Despite acknowledging that closure relations (i.e. interaction terms) are based on simple empirical information, we wonder about the convenience/correctness of relying upon Darcy's law as a valid criterion to obtain general expressions for c in geodynamic contexts.

Work by Hassanizadeh and co-authors (references) circumvent this problem by deriving averaged mass, momentum and energy balance equations not only for the dynamic phases but also for the interfaces, under the framework of rational thermodynamics and volume averaging. Thus, a complete thermodynamic state of the interface is taken into account. In the present work, interfaces are assumed massless, and therefore no additional mass and/or momentum conservation equations are solved for them. Instead, surface tension forces are considered embedded into the dynamic phases, which are taken into account in the individual momentum equations (Eq. (18)). On the contrary, the energetics of the interface, i.e. surface energy density, is explicitly accounted for in the total energy balance Eq. (23). Incorporating a complete thermodynamic state of the interface into our formulation would require both ensemble averaged mass and momentum balance equations for the interface, and an extended numerical scheme. In any case, any resulting system of equations and associated coupling terms should be supported and validated by comprehensive experimental work. Given the progress made in experimental techniques over the ten years, we anticipate that this will be the case in the next decade or so.

6.3 Numerical model

Here we briefly address some inherent numerical issues concerning the solution MPMCRT systems (see Oliveira et al. (2016) and Appendix B for complimentary numerical details).

The mechanical problem represents a major numerical challenge in the present MPMCRT approach. We chose to formulate the individual momentum equations in terms of Cauchy stresses, and therefore constitutive relations are invoked only after obtaining the weak form (see Appendix B). In principle, this approach is more fundamental and general than those in which a certain velocity-stress relation is

assumed beforehand (e.g. the velocity-pressure approach), as it is valid for any arbitrary constitutive relation. However, it is intrinsically less numerically stable (Donea & Huerta, 2003) and it may be challenging for standard some algorithms. In the current implementation, we solve the linear system of governing equations using Matlab's "backslash" solver (2016 edition). Numerous tests indicated that this solver provides satisfactory results. However, we anticipate that a carefully designed global iterative method (e.g. UZAWA method Brezzi & Fortin, 1991) or a nested iterative method (Quarteroni & Valli, 2008; Gresho & Sani, 2000) would improve stability, accuracy and efficiency.

As mentioned above, the solvability of the system as well as local mass-conservation are guaranteed by the use of the augmented Taylor-Hood (Q2-(Q1+Q0)) element. Results between different Taylor-Hood elements are compared in Fig. 11 (A-(Q2-Q1), B-(Q2-(Q1+Q0))). Despite satisfying the LBB compatibility condition, the continuous description of pressure in (Q2-Q1) cannot ensure local mass conservation, which generates unrealistic spurious oscillations on the velocity field (11-A). These instabilities are avoided with the use of (Q2-(Q1+Q0)) (11-B), without the need for further smoothing techniques (Arndt, 2013). The improvement in the stability of the solution using (Q2-(Q1+Q0)) comes at the cost of increasing the degrees of freedom of the system (i.e. 1 additional DOF per element), which translates into an increase in the computation time (up to a factor of $\sim$1.5 for high-resolution experiments).

However, the evaluation of dynamic phase pathlines need oscillation-free continuous flow fields, otherwise coherent trajectories for the dynamic phases cannot be computed. Also, smooth fluxes or secondary quantities derived from pressure and velocity fields (e.g. gradients and divergences of velocities) are needed to compute accurate visco-elasto-plastic stresses. We refer the reader to Section B2 for further details on global smoothing and stresses' computation.

7 CONCLUSIONS

We have presented a conceptual and numerical framework for solving multi-phase multi-component reactive transport (MPMCRT) problems based on the theories of ensemble averaging and classic irreversible thermodynamics. In particular, we presented detailed derivations of $i)$ the fundamental MPMCRT set of ensemble-averaged equations for materials with complex visco-elasto-platic rheologies, $ii)$ the coupling among the thermo-mechanical-chemical system of equations by means of Gibbs-free energy minimization under the assumption of local thermodynamic equilibrium, and $iii)$ a complete numerical scheme to obtain accurate and reliable solutions of the complete set of governing equations. The framework is general and readily extendable to accommodate numerous processes of geodynamic relevance. Our approach is based on the effective tracking of the most basic thermodynamic variables, namely internal energy and chemical composition (not with proxies but actual chemical

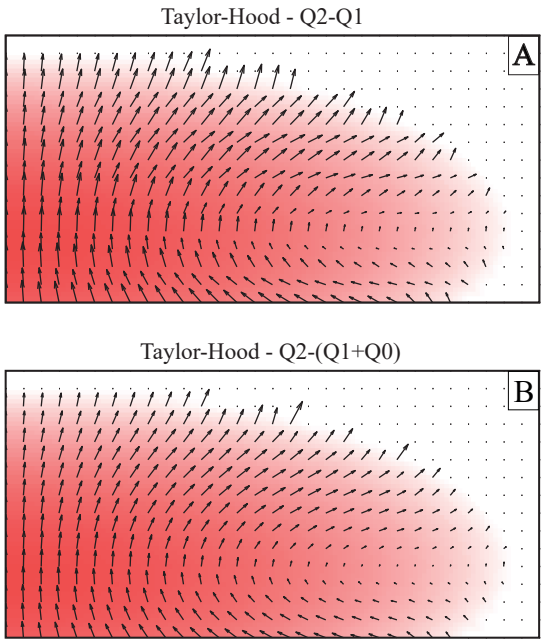

Figure 11. Melt velocity using (upper panel) Taylor-Hood - Q2-Q1 elements, and (bottom panel) Taylor-Hood - Q2-(Q1+Q0) elements for the example depicted in fig. 7 (D, $c = 1E9$). The melt fraction is depicted at the background for reference.

elements), coupled with a true multi-phase formulation in which the different dynamic phases are modelled with their own set of conservations equations and can be subject to different conditions of pressure and temperature. This approach opens up the possibilities to model general non-equilibrium processes and to study the feedbacks between the chemical and thermomechanical behaviours of natural systems (e.g. disequilibrium melting, metasomatism, strain localization via chemical reactions, etc). The method may be particularly useful for studying processes where the assumption of strong coupling between phases is not warranted (e.g. formation of magma chambers, melt localization, volcanic eruptions). Also, the implementation of a chemical thermodynamics solver allows retrieving whole sets of thermodynamically-consistent physical and chemical properties that can be used to predict geophysical and/or geochemical observables. This in turn allows to make an explicit connection to formal geophysical inverse theory and data-assimilation methods and opens up new opportunities for integrated studies of deep processes combining numerical simulations and data inverse analysis (e.g. Baumann & Kaus, 2015; Afonso et al., 2016).

Two simple numerical examples of a two-phase system made up olivine (i.e. one solid solution) were presented to illustrate some of the main concepts and capabilities of the presented method. We showed that the dynamics of a two-phase system using a thermodynamically-consistent scheme can be signifi-

cantly different from those obtained using simpler parameterized (yet widely used) schemes. The main reason for these differences is the chemical-thermomechanical non-linear feedbacks that develop in a thermodynamically-consistent scheme, but that are absent in a parameterized approach. As in most non-linear systems, these feedbacks are not easy to predict or parameterize in complex MPMCRT simulations and their explicit treatment is one of the main strengths of thermodynamically-consistent methods such as the one presented here. We corroborated that the effects of surface tension on the macro-dynamics of the system is of second order (see also Ricard et al., 2001). However, the inclusion of this effect may be critical for interpreting/modelling small-scale segregation processes (e.g. those arising in laboratory experiments).

The numerical examples also highlighted the central role played by the interaction terms (i.e. interface processes) and the assumptions behind their modelling. These terms arise naturally when averaging the phase conservation equations with explicit consideration of jump conditions. This is a critical part of MPMCRT and our ability to develop realistic models for the key interaction terms will determine the success of MPMCRT in modelling real-world scenarios. The form of these interaction terms must be justified based on mathematical, thermodynamic, and experimental grounds. For the purposes of this work, we have employed relatively simple interaction terms, but more comprehensive/realistic forms should be worked out, with support from laboratory experiments, depending on the nature of the system under consideration.

Given space limitations, we have not presented a detailed analysis of the mathematical behaviour of the individual equations (e.g. instability development, porosity-waves, etc), which has been studied in many previous works (e.g. Spiegelman, 1993c; Aharonov et al., 1995; Spiegelman et al., 2001; Connolly & Podladchikov, 2007) We rather focused on the complete chemical-thermal-mechanical coupling of the resulting full system of equations, which is a less understood topic. Similarly non-Newtonian viscosities, damage, strain localization, melt shear bands and full disequilibrium implementations have not been addressed in this study. The predictions and implications of our modelling approach for the understanding of these processes will be the focus of future studies.

ACKNOWLEDGMENTS

B.O. thanks support from an International Macquarie Research Excellence Scholarship (iMQRES) and a graduate scholarship from Obra Social ”la Caixa” and Casa Asia. The work of JCA has been supported by funds from the ARC Centre of Excellence for Core to Crust Fluid Systems and by two ARC Discovery Grants (DP110104145 and DP120102372). This is contribution XX from the Australian Research Council Centre of Excellence for Core to Crust Fluid Systems (http://www.ccfs.mq.edu.au) and YY in the GEMOC Key Centre (http://www.gemoc.mq.edu.au).

References

Afonso, J. C., Zlotnik, S., & Fernández, M., 2008. Effects of compositional and rheological stratifications on small-scale convection under the oceans: Implications for the thickness of oceanic lithosphere and seafloor flattening, *Geophysical Research Letters*, **35**(20).

Afonso, J. C., Zlotnik, S., & Dez, P., 2015. An efficient and general approach for implementing thermodynamic phase equilibria information in geophysical and geodynamic studies, *Geochemistry, Geophysics, Geosystems*, **16**(10), 3767–3777.

Afonso, J. C., Rawlinson, N., Yang, Y., Schutt, D. L., Jones, A. G., Fullea, J., & Griffin, W. L., 2016. 3-d multiobservable probabilistic inversion for the compositional and thermal structure of the lithosphere and upper mantle: Iii. thermochemical tomography in the western-central us, *Journal of Geophysical Research: Solid Earth*, **121**(10), 7337–7370.

Aharonov, E., Whitehead, J., Kelemen, P., & Spiegelman, M., 1995. Channeling instability of upwelling melt in the mantle, *Journal of Geophysical Research: Solid Earth*, **100**(B10), 20433–20450.

Arndt, D., 2013. *Augmented Taylor-Hood Elements for Incompressible Flow*, Ph.D. thesis.

Babeyko, A. & Sobolev, S., 2008. High-resolution numerical modeling of stress distribution in visco-elasto-plastic subducting slabs, *Lithos*, **103**(1), 205–216.

Batchelor, G. K., 2000. *An introduction to fluid dynamics*, Cambridge university press.

Baumann, T. & Kaus, B. J., 2015. Geodynamic inversion to constrain the non-linear rheology of the lithosphere, *Geophysical Journal International*, **202**(2), 1289–1316.

Bear, J. & Bachmat, Y., 2012. *Introduction to modeling of transport phenomena in porous media*, vol. 4, Springer Science & Business Media.

Bercovici, D. & Michaut, C., 2010. Two-phase dynamics of volcanic eruptions: compaction, compression and the conditions for choking, *Geophysical Journal International*, **182**(2), 843–864.

Bercovici, D. & Ricard, Y., 2003. Energetics of a two-phase model of lithospheric damage, shear localization and plate-boundary formation, *Geophysical Journal International*, **152**(3), 581–596.

Bercovici, D., Ricard, Y., & Schubert, G., 2001. A two-phase model for compaction and damage: 1. general theory, *Journal of Geophysical Research: Solid Earth*, **106**(B5), 8887–8906.

Berman, R. G., 1988. Internally-consistent thermodynamic data for minerals in the system na2o-k2o-cao-mgo-feo-fe2o3-al2o3-sio2-tio2-h2o-co2, *Journal of petrology*, **29**(2), 445–522.

Beuchert, M. J. & Podladchikov, Y. Y., 2010. Viscoelastic mantle convection and lithospheric stresses, *geophysical Journal international*, **183**(1), 35–63.

Boettinger, W. J., Warren, J. A., Beckermann, C., & Karma, A., 2002. Phase-field simulation of solidification, *Materials Research*, **32**(1), 163.

Bowen, R. M., 1976. Theory of mixtures, *Continuum physics*, **3**(Pt I).

Bower, A. F., 2009. *Applied mechanics of solids*, CRC press.

Brezzi, F. & Fortin, M., 1991. Mixed and hybrid finite element methods, no. 15 in springer series in computational mathematics.

Chen, L. & Gerya, T. V., 2016. The role of lateral lithospheric strength heterogeneities in orogenic plateau growth: Insights from 3-d thermo-mechanical modeling, *Journal of Geophysical Research: Solid Earth*, **121**(4), 3118–3138, 2016JB012872.

Connolly, J., 2005. Computation of phase equilibria by linear programming: a tool for geodynamic modeling and its application to subduction zone decarbonation, *Earth and Planetary Science Letters*, **236**(1), 524–541.

Connolly, J., 2009. The geodynamic equation of state: what and how, *Geochemistry, Geophysics, Geosystems*, **10**(10).

Connolly, J. & Kerrick, D., 1987. An algorithm and computer program for calculating composition phase diagrams, *Calphad*, **11**(1), 1–55.

Connolly, J. & Podladchikov, Y., 2007. Decompaction weakening and channeling instability in ductile porous media: Implications for asthenospheric melt segregation, *Journal of Geophysical Research: Solid Earth*, **112**(B10).

De Groot, S. R. & Mazur, P., 2013. *Non-equilibrium thermodynamics*, Courier Corporation.

de Souza Neto, E. A., Peric, D., & Owen, D. R. J., 2011. *Computational methods for plasticity: theory and applications*, John Wiley & Sons.

Donea, J. & Huerta, A., 2003. *Finite element methods for flow problems*, John Wiley & Sons.

Drew, D. A., 1971. Averaged field equations for two-phase media, *Studies in Applied Mathematics*, **50**(2), 133–166.

Drew, D. A., 1983. Mathematical modeling of two-phase flow., *Annual Review of Fluid Mechanics*, **50**, 261–291.

Drew, D. A. & Passman, S. L., 1999. Theory of multicomponent fluids.

Dufek, J. & Bachmann, O., 2010. Quantum magmatism: Magmatic compositional gaps generated by melt-crystal dynamics, *Geology*, **38**(8), 687–690.

Elliott, T. & Spiegelman, M., 2003. Melt migration in oceanic crustal production: a u-series perspective, *Treatise on Geochemistry*, **3**, 465–510.

Fischer, F., Waitz, T., Vollath, D., & Simha, N., 2008. On the role of surface energy and surface stress in phase-transforming nanoparticles, *Progress in Materials Science*, **53**(3), 481–527.

Fowler, A. C., 1985. A mathematical model of magma transport in the asthenosphere, *Geophysical & Astrophysical Fluid Dynamics*, **33**(1-4), 63–96.

Frank, F., 1968. Two-component flow model for convection in the earth's upper mantle, *Nature*, **220**,

350–352.

Ganguly, J., 2009. *Thermodynamics in earth and planetary sciences*, Springer Science & Business Media.

Gerya, T. V. & Yuen, D. A., 2007. Robust characteristics method for modelling multiphase visco-elasto-plastic thermo-mechanical problems, *Physics of the Earth and Planetary Interiors*, **163**(14), 83 – 105, Computational Challenges in the Earth Sciences.

Ghiorso, M. S. & Sack, R. O., 1995. Chemical mass transfer in magmatic processes iv. a revised and internally consistent thermodynamic model for the interpolation and extrapolation of liquid-solid equilibria in magmatic systems at elevated temperatures and pressures, *Contributions to Mineralogy and Petrology*, **119**(2-3), 197–212.

Gidaspow, D., 1994. *Multiphase flow and fluidization: continuum and kinetic theory descriptions*, Academic press.

Gray, W. & Hassanizadeh, S., 1989. Averaging theorems and averaged equations for transport of interface properties in multiphase systems, *International Journal of Multiphase Flow*, **15**(1), 81 – 95.

Gray, W. G. & Hassanizadeh, S. M., 1998. Macroscale continuum mechanics for multiphase porous-media flow including phases, interfaces, common lines and common points, *Advances in Water Resources*, **21**(4), 261–281.

Gresho, P. & Sani, R., 2000. Incompressible flow and the finite element method. vol. 1: Advection diffusion. vol. 2: Isothermal laminar flow.

Hassanizadeh, M. & Gray, W. G., 1979a. General conservation equations for multi-phase systems: 1. averaging procedure, *Advances in Water Resources*, **2**, 131 – 144.

Hassanizadeh, M. & Gray, W. G., 1979b. General conservation equations for multi-phase systems: 2. mass, momenta, energy, and entropy equations, *Advances in Water Resources*, **2**, 191–203.

Hassanizadeh, S. M. & Gray, W. G., 1993. Toward an improved description of the physics of two-phase flow, *Advances in Water Resources*, **16**(1), 53–67.

Hesse, M., Schiemenz, A., Liang, Y., & Parmentier, E., 2011. Compaction-dissolution waves in an upwelling mantle column, *Geophysical Journal International*, **187**(3), 1057–1075.

Hill, D. P., 1998. *The computer simulation of dispersed two-phase flow*, Ph.D. thesis, University of London.

Hinton, E. & Campbell, J., 1974. Local and global smoothing of discontinuous finite element functions using a least squares method, *International Journal for Numerical Methods in Engineering*, **8**(3), 461–480.

Holland, T. & Powell, R., 2003. Activity–composition relations for phases in petrological calculations:

an asymmetric multicomponent formulation, *Contributions to Mineralogy and Petrology*, **145**(4), 492–501.

Holland, T. J. B. & Powell, R., 1998. An internally consistent thermodynamic data set for phases of petrological interest, *Journal of Metamorphic Geology*, **16**(3), 309–343.

Holtzman, B., Kohlstedt, D., Zimmerman, M., Heidelbach, F., Hiraga, T., & Hustoft, J., 2003. Melt segregation and strain partitioning: implications for seismic anisotropy and mantle flow, *Science*, **301**(5637), 1227–1230.

Ishii, M., 1975. Thermo-fluid dynamic theory of two-phase flow, *NASA STI/Recon Technical Report A*, **75**, 29657.

Ishii, M. & Hibiki, T., 2006. Thermo-fluid dynamics of two-phase flow. 2006: Springer science.

Iwamori, H., 1993. Dynamic disequilibrium melting model with porous flow and diffusion-controlled chemical equilibration, *Earth and planetary science letters*, **114**(2), 301–313.

Jakobsen, H., 2014. *Chemical Reactor Modelling: multiphase reactive flows (2nd edition)*, Springer, Heidelberg.

Jessell, M., Bons, P., Evans, L., Barr, T., & Stüwe, K., 2001. Elle: the numerical simulation of metamorphic and deformation microstructures, *Computers & Geosciences*, **27**(1), 17–30.

Jing, L., 2003. A review of techniques, advances and outstanding issues in numerical modelling for rock mechanics and rock engineering, *International Journal of Rock Mechanics and Mining Sciences*, **40**(3), 283–353.

Joekar-Niasar, V., Hassanizadeh, S. M., & Dahle, H., 2010. Non-equilibrium effects in capillarity and interfacial area in two-phase flow: dynamic pore-network modelling, *Journal of Fluid Mechanics*, **655**, 38–71.

Kang, Q., Lichtner, P. C., & Zhang, D., 2006. Lattice boltzmann pore-scale model for multicomponent reactive transport in porous media, *Journal of Geophysical Research: Solid Earth*, **111**(B5).

Karakas, O. & Dufek, J., 2015. Melt evolution and residence in extending crust: Thermal modeling of the crust and crustal magmas, *Earth and Planetary Science Letters*, **425**, 131–144.

Katz, R. F., 2008. Magma dynamics with the enthalpy method: Benchmark solutions and magmatic focusing at mid-ocean ridges, *Journal of Petrology*, **49**(12), 2099–2121.

Katz, R. F., Spiegelman, M., & Holtzman, B., 2006. The dynamics of melt and shear localization in partially molten aggregates, *Nature*, **442**(7103), 676–679.

Kaus, B. J., 2010. Factors that control the angle of shear bands in geodynamic numerical models of brittle deformation, *Tectonophysics*, **484**(14), 36 – 47, Quantitative modelling of geological processes.

Keken, P. v., King, S., Schmeling, H., Christensen, U., Neumeister, D., & Doin, M.-P., 1997. A

comparison of methods for the modeling of thermochemical convection, *Journal of Geophysical Research: Solid Earth*, **102**(B10), 22477–22495.

Kelemen, P., Hirth, G., Shimizu, N., Spiegelman, M., & Dick, H., 1997. A review of melt migration processes in the adiabatically upwelling mantle beneath oceanic spreading ridges, *Philosophical Transactions of the Royal Society of London A: Mathematical, Physical and Engineering Sciences*, **355**(1723), 283–318.

Keller, T. & Katz, R. F., 2016. The role of volatiles in reactive melt transport in the asthenosphere, *Journal of Petrology*, p. egw030.

Keller, T., May, D. A., & Kaus, B. J., 2013. Numerical modelling of magma dynamics coupled to tectonic deformation of lithosphere and crust, *Geophysical Journal International*, **195**(3), 1406–1442.

Knapp, R. B., 1989. Spatial and temporal scales of local equilibrium in dynamic fluid-rock systems, *Geochimica et Cosmochimica Acta*, **53**(8), 1955–1964.

Lebon, G., Jou, D., & Casas-Vázquez, J., 2008. *Understanding non-equilibrium thermodynamics*, Springer.

Leo, P. & Sekerka, R., 1999. The effect of surface stress on crystal-melt and crystal-crystal equilibrium, in *Fundamental Contributions to the Continuum Theory of Evolving Phase Interfaces in Solids*, pp. 176–195, Springer.

Liu, J., Pereira, G. G., & Regenauer-Lieb, K., 2014. From characterisation of pore-structures to simulations of pore-scale fluid flow and the upscaling of permeability using microtomography: A case study of heterogeneous carbonates, *Journal of Geochemical Exploration*, **144**, 84–96.

Liu, L., Wan, C., Zhao, C., & Zhao, Y., 2011. Geodynamic constraints on orebody localization in the anqing orefield, china: computational modeling and facilitating predictive exploration of deep deposits, *Ore Geology Reviews*, **43**(1), 249–263.

Lundgren, T. S., 1972. Slow flow through stationary random beds and suspensions of spheres, *Journal of Fluid Mechanics*, **51**(02), 273–299.

Mayer, K. U., Frind, E. O., & Blowes, D. W., 2002. Multicomponent reactive transport modeling in variably saturated porous media using a generalized formulation for kinetically controlled reactions, *Water Resources Research*, **38**(9).

McKenzie, D., 1984. The generation and compaction of partially molten rock, *Journal of Computational Physics*, **25**, 713–765.

Moresi, L., Dufour, F., & Mhlhaus, H.-B., 2003. A lagrangian integration point finite element method for large deformation modeling of viscoelastic geomaterials, *Journal of Computational Physics*, **184**(2), 476 – 497.

Muhlhaus, H.-B. & Regenauer-Lieb, K., 2005. Towards a self-consistent plate mantle model that includes elasticity: simple benchmarks and application to basic modes of convection, *Geophysical Journal International*, **163**(2), 788–800.

Ni, J. & Beckermann, C., 1991. A volume-averaged two-phase model for transport phenomena during solidification, *Metallurgical Transactions B*, **22**(3), 349–361.

Ochoa-Tapia, J. A. & Whitaker, S., 1995a. Momentum transfer at the boundary between a porous medium and a homogeneous fluidi. theoretical development, *International Journal of Heat and Mass Transfer*, **38**(14), 2635–2646.

Ochoa-Tapia, J. A. & Whitaker, S., 1995b. Momentum transfer at the boundary between a porous medium and a homogeneous fluidii. comparison with experiment, *International Journal of Heat and Mass Transfer*, **38**(14), 2647–2655.

Oliveira, B., Afonso, J. C., & Zlotnik, S., 2016. A lagrangian eulerian finite element algorithm for advectiondiffusionreaction problems with phase change, *Computer Methods in Applied Mechanics and Engineering*, **300**, 375 – 401.

Peters, M., Veveakis, M., Poulet, T., Karrech, A., Herwegh, M., & Regenauer-Lieb, K., 2015. Boudinage as a material instability of elasto-visco-plastic rocks, *Journal of Structural Geology*, **78**, 86 – 102.

Quarteroni, A. & Valli, A., 2008. *Numerical approximation of partial differential equations*, vol. 23, Springer Science & Business Media.

Rabinowicz, M. & Vigneresse, J.-L., 2004. Melt segregation under compaction and shear channeling: Application to granitic magma segregation in a continental crust, *Journal of Geophysical Research: Solid Earth*, **109**(B4).

Regenauer-Lieb, K., Veveakis, M., Poulet, T., Paesold, M., Rosenbaum, G., Weinberg, R. F., & Karrech, A., 2015. Multiscale, multiphysics geomechanics for geodynamics applied to buckling instabilities in the middle of the australian craton, *Philosophical Magazine*, **95**(28-30), 3055–3077.

Ricard, Y., Bercovici, D., & Schubert, G., 2001. A two-phase model for compaction and damage. ii- applications to compaction, deformation, and the role of interfacial surface tension, *Journal of geophysical research*, **106**(B5), 8907–8924.

Rudge, J. F., Bercovici, D., & Spiegelman, M., 2011. Disequilibrium melting of a two phase multicomponent mantle, *Geophysical Journal International*, **184**(2), 699–718.

Ryan, M. P., 1990. *Magma transport and storage*, John Wiley & Sons Incorporated.

Saffman, P. G., 1971. On the boundary condition at the surface of a porous medium, *Studies in Applied Mathematics*, **50**(2), 93–101.

Scardovelli, R. & Zaleski, S., 1999. Direct numerical simulation of free-surface and interfacial flow,

Annual review of fluid mechanics, **31**(1), 567–603.

Schiemenz, A., Liang, Y., & Parmentier, E., 2011. A high-order numerical study of reactive dissolution in an upwelling heterogeneous mantlei. channelization, channel lithology and channel geometry, *Geophysical Journal International*, **186**(2), 641–664.

Schlichting, H. & Gersten, K., 2003. *Boundary-layer theory*, Springer Science & Business Media.

Scott, D. R. & Stevenson, D. J., 1986. Magma ascent by porous flow, *Journal of Geophysical Research: Solid Earth*, **91**(B9), 9283–9296.

Sleep, N. H., 1974. Segregation of magma from a mostly crystalline mush, *Geological Society of America Bulletin*, **85**(8), 1225–1232.

Sobolev, S. V., Babeyko, A. Y., Koulakov, I., & Oncken, O., 2006. Mechanism of the andean orogeny: insight from numerical modeling, in *The Andes*, pp. 513–535, Springer.

Sparks, D. W. & Parmentier, E., 1991. Melt extraction from the mantle beneath spreading centers, *Earth and Planetary Science Letters*, **105**(4), 368–377.

Spiegelman, M., 1993a. Flow in deformable porous media. part 1 simple analysis, *Journal of Fluid Mechanics*, **247**, 17–38.

Spiegelman, M., 1993b. Physics of melt extraction: Theory, implications and applications, *Philosophical Transactions of the Royal Society of London A: Mathematical, Physical and Engineering Sciences*, **342**(1663), 23–41.

Spiegelman, M., 1993c. Flow in deformable porous media. part 2 numerical analysis–the relationship between shock waves and solitary waves, *Journal of Fluid Mechanics*, **247**, 39–63.

Spiegelman, M. & Elliott, T., 1993. Consequences of melt transport for uranium series disequilibrium in young lavas, *Earth and Planetary Science Letters*, **118**(1), 1–20.

Spiegelman, M. & Kelemen, P. B., 2003. Extreme chemical variability as a consequence of channelized melt transport, *Geochemistry, Geophysics, Geosystems*, **4**(7).

Spiegelman, M., Kelemen, P. B., & Aharonov, E., 2001. Causes and consequences of flow organization during melt transport: The reaction infiltration instability in compactible media, *Journal of Geophysical Research: Solid Earth*, **106**(B2), 2061–2077.

Šrámek, O., Ricard, Y., & Bercovici, D., 2007. Simultaneous melting and compaction in deformable two-phase media, *Geophysical Journal International*, **168**(3), 964–982.

Steefel, C. I., DePaolo, D. J., & Lichtner, P. C., 2005. Reactive transport modeling: An essential tool and a new research approach for the earth sciences, *Earth and Planetary Science Letters*, **240**(3), 539–558.

Sun, Y. & Beckermann, C., 2004. Diffuse interface modeling of two-phase flows based on averaging: mass and momentum equations, *Physica D: Nonlinear Phenomena*, **198**(3), 281–308.

Sutton, A. P. & Balluffi, R. W., 1995. Interfaces in crystalline materials.

Takei, Y. & Hier-Majumder, S., 2009. A generalized formulation of interfacial tension driven fluid migration with dissolution/precipitation, *Earth and Planetary Science Letters*, **288**(12), 138 – 148.

Tilhac, R., Ceuleneer, G., Griffin, W. L., OReilly, S. Y., Pearson, N. J., Benoit, M., Henry, H., Girardeau, J., & Grégoire, M., 2016. Primitive arc magmatism and delamination: Petrology and geochemistry of pyroxenites from the cabo ortegal complex, spain, *Journal of Petrology*, p. egw064.

Tirone, M., Ganguly, J., & Morgan, J. P., 2009. Modeling petrological geodynamics in the earth's mantle, *Geochemistry, Geophysics, Geosystems*, **10**(4), n/a–n/a, Q04012.

Weatherley, S. & Katz, R., 2012. Melting and channelized magmatic flow in chemically heterogeneous, upwelling mantle, *Geochemistry, Geophysics, Geosystems*, **13**(5).

Zhang, D. & Prosperetti, A., 1997. Momentum and energy equations for disperse two-phase flows and their closure for dilute suspensions, *International Journal of Multiphase Flow*, **23**(3), 425 – 453.

Zienkiewicz, O. C. & Taylor, R. L., 2000. *The finite element method: solid mechanics*, vol. 2, Butterworth-heinemann.

Zienkiewicz, O. C. & Zhu, J. Z., 1992. The superconvergent patch recovery and a posteriori error estimates. part 1: The recovery technique, *International Journal for Numerical Methods in Engineering*, **33**(7), 1331–1364.

APPENDIX A: ENSEMBLE AVERAGING

This appendix provides further details on the ensemble averaging technique presented in the main text, including schematic illustrations and definitions of averaged properties, spatial and temporal derivatives of averaged variables and a complete description of the averaged strain-rate tensor in MPMCRT scenarios. For an extended review on ensemble averaging and other averaging techniques we refer the reader to (Ishii, 1975; Drew, 1971; Drew & Passman, 1999; Bear & Bachmat, 2012, and references therein).

A1 Basic definitions

For completeness, we first recover the definition of the ensemble average of a scalar, vectorial or tensorial quantity $\Phi(\mathbf{x}, t; \pi)$. From section 2.1, we have

$$\langle \Phi(\mathbf{x}, t; \pi) \rangle = \lim_{\pi \to \infty} \frac{1}{\pi} \sum_{\pi} \Phi(\mathbf{x}, t; \pi) \tag{A.1}$$

where π refers to a single realization, and $\mathbf{x}$ and t are the usual space and time variables. Measurements

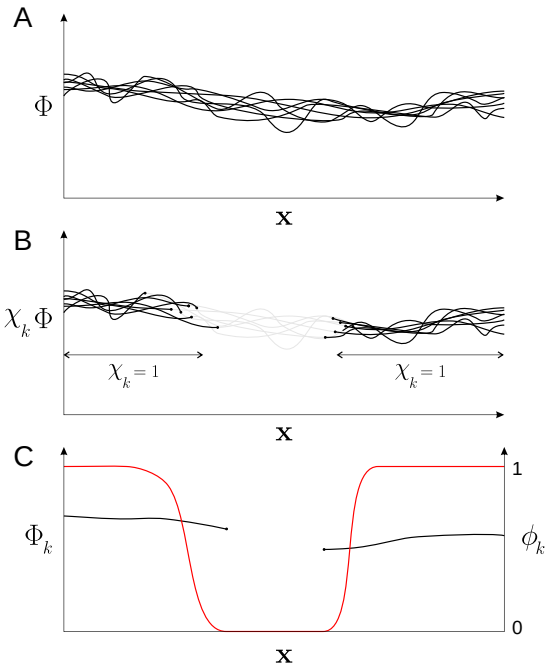

Figure A1. Graphic representation of the ensemble averaging of a generic property Φ. A) Set of realizations, or ensemble, of Φ. B) Conditioned measurements of each of the realization to the presence of the dynamic phase k, $\chi_k\Phi$. Notice that each realization is multiplied by a different characteristic function χ_k, since the topology varies between realizations. C) Intrinsic average of Φ, $\Phi_k = \frac{\langle\chi_k\Phi\rangle}{\phi_k}$ and the averaged phase fraction $\phi_k = \langle\chi_k\rangle$.

of any quantity Φ at a given point in space and time of a MPMCRT system is a challenging task, since in general we may encounter various phases at that particular point for different realizations. This is illustrated in Fig. A1-A, where several realizations of Φ are shown in a 1-D space profile and for a fixed time t. The measurement of a particular property coming from only one of the dynamic phases is achieved conditioning the property to the presence of the dynamic phase under consideration. We condition the quantity Φ in phase k by multiplying it with the characteristic function, $\chi_k\left(\mathbf{x}, t; \pi\right)$. The characteristic function is defined to be unity within the region/phase of interest and zero elsewhere for any realization π

$$\chi_k = \left\{ \begin{array}{ll} 1 & \text{if } \mathbf{x} \in k \text{ in realization } \pi, \\ 0 & \text{otherwise} \end{array} \right\} \tag{A.2}$$

Consequently, $\chi_k\Phi$ represents the isolated phase property (Φ) of a single realization π. This is schematically shown in Fig. A1-B. Furthermore, the characteristic function evolves according to the so-called topological equation, which is obtained considering the temporal derivative of the characteristic function

$$\frac{\partial \chi_k}{\partial t} + \mathbf{v}_i \cdot \nabla \chi_k = 0 \tag{A.3}$$

where $\mathbf{v}_i$ is the velocity of the interface. Once Φ has been isolated from its surroundings (Fig. A1-B, $\chi_k \Phi$), we ensemble average it in order to obtain a separate averaged description of the property Φ inside a given dynamic phase k (Fig. A1-C)

$$\langle \chi_k \Phi \rangle = \lim_{\pi \to \infty} \frac{1}{\pi} \sum_{\pi} \chi_k \Phi \tag{A.4}$$

Since χ_k is zero everywhere except in regions where phase k exists, we can rewrite the sum in Eq. (A.4) in terms of realizations where only phase k is present (denoted by π_k)

$$\begin{aligned} \langle \chi_k \Phi \rangle &= \lim_{\pi \to \infty} \frac{1}{\pi} \sum_{\pi_k} \Phi \\ &= \lim_{\pi \to \infty} \frac{\pi_k}{\pi} \frac{1}{\pi_k} \sum_{\pi_k} \Phi \\ &= \phi_k \lim_{\pi_k \to \infty} \frac{1}{\pi_k} \sum_{\pi_k} \Phi \\ &= \phi_k \Phi_k \end{aligned} \tag{A.5}$$

where, $\phi_k = \langle \chi_k \rangle$ is the averaged phase fraction

$\Phi_k = \lim_{\pi_k \to \infty} \frac{1}{\pi_k} \sum_{\pi_k} \Phi$ is the intrinsic phase average

Intrinsic average or phase-weighted average values correspond to the "true" phase averaged quantities of any property Φ, and are denoted with subindex k (except for the averaged phase fraction ϕ_k, and other mass-weighted variables, see below). A graphical representation of both, the intrinsic average and average phase fraction, is given in Fig. A1-C. For the simple case of the density, $\Phi = \rho$, the intrinsic phase average of the density refers to the averaged density that the system would have if it was only comprised by that single phase. From Eq. (A.5) we define the intrinsic or phase-weighted average as,

$$\Phi_k = \frac{\langle \chi_k \Phi \rangle}{\phi_k} \tag{A.6}$$

In the formulation developed here, however, we also introduce mass-weighted average quantities, such as the mass-weighted average velocity in Eq. (12). Its definition naturally arises after ensemble averaging the local conservation equations (see section 2.2), and is proven to be useful when analyzing different aspects of multiphase systems (i.e. momentum transport and/or reactive transport). The mass-weighted average for a general property Φ is defined as

$$\Phi_k = \frac{\langle \chi_k \rho \Phi \rangle}{\phi_k \rho_k} \tag{A.7}$$

Note that we used the same notation (subindex k) to represent both the intrinsic and the mass-weighted averages (Eqs. (A.6) and (A.7)). In the main text, however, we will make clear which definition is being used.

A1.1 Fluctuating fields

In general, the ensemble-averaged velocity of a multi-phase system is not the same as the complete (or true) velocity field due to the fluctuating motion of the individual interfaces (e.g. due to turbulence). Therefore, analogous to the single-phase Reynolds decomposition, any variable can be represented as its ensemble-averaged value plus its corresponding fluctuating field, $\Phi_k^{''}$, as

$$\Phi = \Phi_k + \Phi_k^{''} \tag{A.8}$$

Using the previous relation we can further explore the ensemble average of the product between two different properties (i.e. ${}^A\Phi$, ${}^B\Phi$) as,

$$\begin{aligned} \langle \chi_k {}^A\Phi {}^B\Phi \rangle &= \langle \chi_k \left({}^A\Phi_k + {}^A\Phi_k^{''} \right) \left({}^B\Phi_k + {}^B\Phi_k^{''} \right) \rangle \\ &= \langle \chi_k \rangle {}^A\Phi_k {}^B\Phi_k + \langle \chi_k {}^A\Phi_k^{''} {}^B\Phi_k^{''} \rangle \\ &= \phi_k {}^A\Phi_k {}^B\Phi_k + \langle \chi_k {}^A\Phi_k^{''} {}^B\Phi_k^{''} \rangle \end{aligned} \tag{A.9}$$

where the ensemble average of the fluctuating fields is zero, $\langle \chi_k \Phi_k^{''} \rangle = 0$. The last term above represents the correlation between the fluctuating fields, which is, in general, non zero. Thus, from Eq. (A.9) we conclude that the ensemble average of the product between two different properties, such as velocity and internal energy, is not the simple product of their averaged values ($\langle \chi_k \mathbf{v} u \rangle \neq \phi_k \mathbf{v}_k u_k$). The Reynolds fluxes arising in the averaged energy equation in Eq. (21) are, for instance, direct consequence of this result.

A2 Gauss and Leibniz averaging rules

Terms involving temporal and spatial derivatives of Φ and χ_k arise when local conservation equations are ensemble-averaged. In the following, we summarize the main relations employed in this work, which can be found in Drew (1971); Drew & Passman (1999); Bear & Bachmat (2012).

These relations are equally valid for any type of average, and are known as the Gauss and Leibniz rules. They read, respectively, as

$$\begin{aligned}\langle\chi_k\nabla\Phi\rangle &= \langle\nabla\chi_k\Phi\rangle - \langle\Phi\nabla\chi_k\rangle = \nabla\langle\chi_k f\rangle - \langle\Phi\nabla\chi_k\rangle \\ \langle\chi_k\frac{\partial\Phi}{\partial t}\rangle &= \langle\frac{\partial\chi_k\Phi}{\partial t}\rangle - \langle\Phi\frac{\partial\chi_k}{\partial t}\rangle = \frac{\partial\langle\chi_k\Phi\rangle}{\partial t} - \langle\Phi\frac{\partial\chi_k}{\partial t}\rangle\end{aligned} \tag{A.10}$$

The last terms on the right-hand-side refer to the averaged influence of Φ on the interface, and are closely related to the interaction terms arising in our MPMCRT formulation. Therefore the interaction terms are not only conceptually appealing to model the influence of the surrounding media on a given phase (i.e. Newton's third law), but also rigorously justified and obtained through mathematical derivation.

Another useful expression is the average of a material derivative,

$$\langle\frac{\mathrm{D}}{\mathrm{D}t}(\circ)\rangle = \frac{\mathrm{D}}{\mathrm{D}t}\langle(\circ)\rangle - \langle(\circ)\,\nabla\cdot\mathbf{v}\rangle + \langle(\circ)\rangle\langle\nabla\cdot\mathbf{v}\rangle = \frac{\mathrm{D}}{\mathrm{D}t}\langle(\circ)\rangle - \langle((\circ) - \langle(\circ)\rangle)\,(\nabla\cdot\mathbf{v})\rangle \tag{A.11}$$

which clearly shows that, in general, the ensemble average of the material derivative is not the material derivative of the averaged value. This result is of particular importance when ensemble averaging the objective time derivative of the stress tensor for elastic rheologies (section 2.7.2, Eq. (44)).

A3 Averaged strain-rate tensor

The deformation of a continuum is usually defined by the strain-rate tensor, $\dot{\boldsymbol{\varepsilon}}$, which is function of the velocity gradients. For small deformations it is defined as,

$$\dot{\boldsymbol{\varepsilon}} = \frac{1}{2}\left(\nabla\mathbf{v} + [\nabla\mathbf{v}]^T\right) \tag{A.12}$$

The averaged strain-rate tensor, $\dot{\boldsymbol{\varepsilon}}_k$, is obtained from Eq. ((A.12)) following the standard averaging procedure. We first isolate the phase contribution multiplying the strain-rate tensor with the characteristic function χ_k, and then proceed with the usual ensemble averaging as,

$$\begin{aligned}\dot{\boldsymbol{\varepsilon}}_k = \frac{\langle\chi_k\rho\dot{\boldsymbol{\varepsilon}}\rangle}{\phi_k\rho_k} &= \frac{1}{2\phi_k\rho_k}\left(\langle\chi_k\rho\nabla\mathbf{v}\rangle + \langle\chi_k\rho\nabla\mathbf{v}\rangle^\top\right) \\ &= \frac{1}{2\phi_k\rho_k}\left(\nabla\langle\chi_k\rho\mathbf{v}\rangle + \nabla\langle\chi_k\rho\mathbf{v}\rangle^\top - \left(\mathbf{U}_k + \mathbf{U}_k^\top\right)\right) \\ &= \frac{1}{2\phi_k\rho_k}\left(\nabla\phi_k\rho_k\mathbf{v}_k + \nabla\left[\phi_k\rho_k\mathbf{v}_k\right]^\top - \left(\mathbf{U}_k + \mathbf{U}_k^\top\right)\right) \\ \text{where}\quad \mathbf{v}_k = \frac{\langle\chi_k\rho\mathbf{v}\rangle}{\phi_k\rho_k} &\text{ and } \mathbf{U}_k = \langle\mathbf{v}\nabla\chi_k\rho\rangle\end{aligned} \tag{A.13}$$

where the average strain rate tensor corresponds to the mass-weighted averaged strain rate tensor and not the intrinsic phase average strain-rate tensor. The justification is based on the following arguments. First, the mass-weighted averaged strain rate tensor aligns with the definition of motion,

and consequently deformation, in terms of the mass-weighted properties (see section 2.2 for further discussion on the topic). The averaged strain-rate tensor in Eq. (A.13), thus, defines the relative deformation of small volumes of mass associated to a single dynamic phase (Fig. 2). An second, it enables us to keep consistency with the definition of velocity used throughout this work, since the resulting average strain-rate tensor is an explicit function of mass-weighted average velocities. Indeed, the mass-weighted average definition of the strain-rate tensor itself incorporates the density into relation (A.13) (first line), which is used, after minor algebra, to describe the average velocity as a mass-weighted average (third line). This greatly simplifies the formulation presented here, as otherwise, the deformation could be expressed in terms of other averaged velocity quantities (i.e. intrinsic average velocities), which would inevitably require additional closure relations, introducing yet more equations and unknowns.

As for the tensor $\mathbf{U}_k$ in Eq. (A.13), it contains information relating bulk velocities at the interface. Its evaluation requires proper modelling, since the analytical solution of it is, to our knowledge, unknown. However, its form can be estimated from fundamental constraints (Bercovici et al., 2001). For instance, $\mathbf{U}_k$ needs to ensure that the deviatoric strain-rate tensor remains traceless after ensemble averaging the true deviatoric strain-rate tensor. This characteristic is a must regardless the employed averaging technique (i.e. volume, time, ensemble), since external isotropic forces over an incompressible mixture should not produce any expansion or extension, and only the pressures should increase/decrease. In addition, the second law of thermodynamics states that the viscous energy dissipation is always positive, and thus, the resulting deviatoric stress tensor must fulfill $\nabla \mathbf{v}_k : \boldsymbol{\tau}_k > 0$. A possible, but by no means unique definition of $\mathbf{U}_k$ satisfying the previous constrains is given by,

$$\mathbf{U}_k \approx (\nabla \phi_k \rho_k)\, \mathbf{v}_k \tag{A.14}$$

which yields the final expression for the averaged strain-rate tensor as,

$$\dot{\boldsymbol{\varepsilon}}_k = \frac{1}{2}\left(\nabla \mathbf{v}_k + [\nabla \mathbf{v}_k]^\top\right) \tag{A.15}$$

The definition above is equivalent to Bercovici's form in (Bercovici et al., 2001) section 4.2, and keeps analogy with the true strain rate tensor definition in (A.12), but with gradients of averaged velocities instead.

APPENDIX B: NUMERICAL DETAILS OF THE MECHANICAL MODEL

This appendix extends the numerical details introduced in 4.1, including the complete finite element discretization and its corresponding matrix form, as well as, the stress recovery procedure. Further

explanations on how to solve the energy, reactive transport and thermodynamic problems can be found elsewhere (e.g. Oliveira et al., 2016; Connolly, 2005), and thus are not included here.

B1 FEM discretization

The mechanical problem is a combination of N individual momentum equations (Eq. (18), one for each dynamic phase), $N-1$ pressure difference type equations (Eq. (51), one for each pare of co-existing dynamic phases), and a total mass balance equation (Eq. (14)), complemented with proper boundary conditions. The strong form of the mechanical problem reads as,

$$\begin{aligned}
\nabla\left(\phi_k P_k\right) - \nabla\cdot\left(2\phi_k\mu_k^{eff}\dot{\boldsymbol{\varepsilon}}_k^{'} + \phi_k\chi_k^{\boldsymbol{\tau}}\hat{\boldsymbol{\tau}}_k^0\right) &= \phi_k\rho_k\mathbf{b}_k + \sum_{z\neq k} c_{k,z}\Delta\mathbf{v}_{k,z} + P_\omega\nabla\phi_k + \omega_k\nabla\left(\sigma\alpha\right) && \text{in } \Omega \\
\sum_k \nabla\cdot\left(\phi_k\mathbf{v}_k\right) &= \sum_k\sum_{z>k}\Gamma_{k,z}^m\left(\frac{1}{\rho_k}-\frac{1}{\rho_j}\right) && \text{in } \Omega \\
\Delta P_{k,j} + \Theta_{k,j} &= -\xi_{k,j}^{eff}\left(\omega_k\phi_k\nabla\cdot\mathbf{v}_k - \omega_j\phi_j\nabla\cdot\mathbf{v}_j\right) + \chi_{k,j}^P\Delta P_{k,j}^0 && \\
\mathbf{v}_k &= \mathbf{v}_{k_D} && \text{in } \Gamma_D \\
\mathbf{n}\boldsymbol{\sigma}_k &= \mathbf{t} && \text{in } \Gamma_N
\end{aligned} \tag{B.1}$$

where velocities $\mathbf{v}_k$ and pressures P_k need to be determined. Ω refers to the domain, and Γ_D and Γ_N are portions of the domain boundary $\partial\Omega$ ($\Gamma_D\cup\Gamma_N=\partial\Omega$) where Dirichlet and Neumann boundary conditions are respectively defined. As usual, we obtain the weak formulation from Eqs. (B.1), multiplying the Stokes equations by a velocity test function $\mathbf{w}\in\mathcal{V}$ and integrating them over the domain Ω, where $\mathcal{V}=\{\mathbf{w}\in\mathcal{H}^1(\Omega)\,|\mathbf{w}=0 \text{ on } \Gamma_D\}$. Similarly, we proceed with the pressure difference equations and the total mass conservation equation by multiplying them by the pressure test function $q\in\mathcal{Q}$ and integrating, with $\mathcal{Q}=\{q\in\mathcal{L}^2(\Omega)\}$. Following standard algebraic procedures, we can obtain the weak form of Eqs. (B.1) as,

$$\begin{aligned}
&\int_\Omega \phi_k P_k\nabla\cdot\mathbf{w}d\Omega - \int_\Omega \nabla\mathbf{w} : \left(2\phi_k\mu_k^{eff}\dot{\boldsymbol{\varepsilon}}_k^{'}\right)d\Omega = \int_{\Gamma_N}\mathbf{w}\cdot\mathbf{t}d\Gamma + \int_\Omega \mathbf{w}\cdot\left(\nabla\cdot\phi_k\chi_k^{\boldsymbol{\tau}}\hat{\boldsymbol{\tau}}_k^0\right)d\Omega \\
&+ \int_\Omega \mathbf{w}\cdot\phi_k\rho_k\mathbf{b}_k d\Omega + \int_\Omega \mathbf{w}\cdot\sum_{z\neq k} c_{k,z}\Delta\mathbf{v}_{k,z}d\Omega + \int_\Omega \mathbf{w}\cdot P_\omega\nabla\phi_k d\Omega + \int_\Omega \mathbf{w}\cdot\omega_k\nabla\left(\sigma\alpha\right)d\Omega \\
&\int_\Omega q\phi_k\nabla\cdot\mathbf{v}_k d\Omega + \int_\Omega q\mathbf{v}_k\cdot\nabla\phi_k d\Omega = \sum_k\sum_{z>k}\int_\Omega q\Gamma_{k,z}^m\left(\frac{1}{\rho_k}-\frac{1}{\rho_z}\right)d\Omega \\
&\int_\Omega q\Delta P_{k,j} + \int_\Omega q\Theta_{k,j} = -\int_\Omega q\xi_{k,j}^{eff}\left(\omega_k\phi_k\nabla\cdot\mathbf{v}_k - \omega_j\phi_j\nabla\cdot\mathbf{v}_j\right)d\Omega + \int_\Omega q\chi_{k,j}^P\Delta P_{k,j}^0 d\Omega
\end{aligned} \tag{B.2}$$

The proof of the equivalence of the strong and weak formulation has been omitted here. The Galerkin

formulation of the mechanical problem in terms of both velocities and pressures leads to a mixed finite element approach. We introduce $\mathbf{v}_k^h$, P_k^h, $\mathbf{w}^h$ and q^h as the finite element discretizations of velocities, pressures and their associate weighting functions respectively; we also denote $\mathcal{V}^h$ and $\mathcal{Q}^h$ as the finite dimensional subspaces of $\mathcal{V}$ and $\mathcal{Q}$, where $\mathbf{v}_k^h \in \mathcal{V}^h$, $P_k^h \in \mathcal{Q}^h$ and $(\mathbf{w}^h, q^h) \in \mathcal{V}^h \times \mathcal{Q}^h$. These subspaces are characterized by being a partition of the domain, and are formed by elements and nodes. We denote $\mathcal{N}_\mathbf{v}$ and $\mathcal{N}_P$ the sets of velocity and pressure nodes in the grid. The velocities and pressures can be approximated in terms of shape functions and associated nodal values as,

$$\begin{aligned} \mathbf{v}_k(\mathbf{x}) \simeq \mathbf{v}_k^h(\mathbf{x}) &= \sum_{a \in \mathcal{N}_\mathbf{v}} N_\mathbf{v}^a(\mathbf{x})\, \mathbf{v}_k^a \\ P_k(\mathbf{x}) \simeq P_k^h(\mathbf{x}, t) &= \sum_{a \in \mathcal{N}_P} N_P^a(\mathbf{x})\, P_k^a \end{aligned} \tag{B.3}$$

where $N_\mathbf{v}^a$ is the velocity shape function associated with node a, and $\mathbf{v}_k^a$ is the value of $\mathbf{v}_k^h$ at node a. The pressure P_k^a (with $a \in \mathcal{N}_P$), is interpolated using N_P. We employ the extended Taylor-Hood element (Q2-(Q1+Q0)) with 9-velocity nodes and 5-pressure nodes to guarantee stability of the solution. This velocity-pressure pair satisfies the LBB condition, ensures local mass conservation and incompressibility constraint (Arndt, 2013), and helps preventing shear locking (see section C).
The mechanical problem in Eqs. (B.2) is discretized in space using the interpolation and the Galerkin formulation introduced above. The resulting matrix system assumes the following partitioned form for a general N-phase system,

$$\begin{bmatrix} \mathbf{VV}_1 & \mathbf{VP}_1 & \mathbf{VI}_1^2 & \mathbf{PI}_1^2 & \dots & \mathbf{VI}_1^{N-1} & \mathbf{PI}_1^{N-1} & \mathbf{VI}_1^N & \mathbf{PI}_1^N \\ \mathbf{VI}_2^1 & \mathbf{PI}_2^1 & \mathbf{VV}_2 & \mathbf{VP}_2 & \dots & \mathbf{VI}_2^{N-1} & \mathbf{PI}_2^{N-1} & \mathbf{VI}_2^N & \mathbf{PI}_2^N \\ \dots & \dots & \dots & \dots & \dots & \dots & \dots & \dots & \dots \\ \mathbf{VI}_N^1 & \mathbf{PI}_N^1 & \mathbf{VI}_N^2 & \mathbf{PI}_N^2 & \dots & \mathbf{VV}_{N-1} & \mathbf{VP}_{N-1} & \mathbf{VV}_N & \mathbf{VP}_N \\ \mathbf{MV}_1 & 0 & \mathbf{MV}_2 & 0 & \dots & \mathbf{MV}_{N-1} & 0 & \mathbf{MV}_N & 0 \\ \mathbf{PV}_1^2 & \mathbf{PP} & -\mathbf{PV}_2^1 & -\mathbf{PP} & 0 & 0 & 0 & 0 & 0 \\ \dots & \dots & \dots & \dots & \dots & \dots & \dots & \dots & \dots \\ 0 & 0 & 0 & 0 & 0 & \mathbf{PV}_{N-1}^N & \mathbf{PP} & -\mathbf{PV}_N^{N-1} & -\mathbf{PP} \end{bmatrix} \begin{bmatrix} \mathbf{v}_1 \\ P_1 \\ \mathbf{v}_2 \\ P_2 \\ \dots \\ \mathbf{v}_{N-1} \\ P_{N-1} \\ \mathbf{v}_N \\ P_N \end{bmatrix} = \begin{bmatrix} \mathbf{fV}_1 \\ \mathbf{fV}_2 \\ \dots \\ \mathbf{fV}_{N-1} \\ \mathbf{fV}_N \\ \mathbf{fM} \\ {}^P\mathbf{fP}_1^2 \\ \dots \\ {}^P\mathbf{fP}_{N-1}^N \end{bmatrix}$$

with the matrices defined as,

$$
\begin{aligned}
\mathbf{VV}_k &= -\int_\Omega \mathbf{B}^T \mathbf{D}_k \mathbf{B} \Omega - \int_\Omega \left(\sum_z c_{k,z} \right) \mathbf{N}_\mathbf{v}^T \mathbf{N}_\mathbf{v} d\Omega \\
\mathbf{VP}_k &= -\int_\Omega \phi_k \mathbf{G}_\mathbf{v}^T \mathbf{N}_P d\Omega - \int_\Omega \frac{(1-\omega_k)}{\sum_z (1-\omega_z)} \mathbf{N}_\mathbf{v}^T \nabla \phi_k \mathbf{N}_P d\Omega \\
\mathbf{fV}_k &= \int_\Omega \mathbf{N}_\mathbf{v}^T \phi_k \rho_k \mathbf{g} d\Omega + \int_\Omega \widetilde{\mathbf{N}}_\mathbf{v}^T \otimes \left(\mathbf{B}^T \phi_k \chi_k^\tau \hat{\boldsymbol{\tau}}_k^0 \right) d\Omega + \int_\Omega \mathbf{N}_\mathbf{v}^T \omega_k \nabla \left(\sigma \alpha \right) d\Omega + \int_{\Gamma_N} \mathbf{N}_\mathbf{v}^T \cdot \mathbf{t} d\Gamma \\
\mathbf{VI}_k^j &= \int_\Omega c_{k,j} \mathbf{N}_\mathbf{v}^T \mathbf{N}_\mathbf{v} d\Omega \\
\mathbf{PI}_k^j &= \int_\Omega \frac{(1-\omega_j)}{\sum_l (1-\omega_l)} \mathbf{N}_\mathbf{v}^T \nabla \phi_k \mathbf{N}_P d\Omega \\
\mathbf{MV}_k &= \int_\Omega \mathbf{N}_P^T \left[\nabla \phi_k \right]^T \mathbf{N}_\mathbf{v} d\Omega + \int_\Omega \phi_k \mathbf{N}_P^T \mathbf{G}_\mathbf{v} d\Omega \\
\mathbf{fM} &= \sum_k \sum_{z>k} \int_\Omega \mathbf{N}_P^T \Gamma_{k,z}^m \left(\frac{1}{\rho_k} - \frac{1}{\rho_z} \right) d\Omega \\
\mathbf{PP} &= \int_\Omega \mathbf{N}_P^T \mathbf{N}_P d\Omega \\
\mathbf{PV}_k^j &= \int_\Omega \mathbf{N}_P^T \xi_{k,j}^{eff} \omega_k \phi_k \mathbf{G}_\mathbf{v} d\Omega \\
\mathbf{fP}_k^j &= \int_\Omega \mathbf{N}_P^T \chi_{k,j}^P \Delta P_{k,j}^0 d\Omega + \int_\Omega \mathbf{N}_P^T \Theta_{k,j} d\Omega
\end{aligned}
\tag{B.4}
$$

where,

$$
\begin{aligned}
\mathbf{N}_\mathbf{v} &= \begin{bmatrix} N_\mathbf{v}^1 & 0 & N_\mathbf{v}^2 & 0 & ... & N_\mathbf{v}^9 & 0 \\ 0 & N_\mathbf{v}^1 & 0 & N_\mathbf{v}^2 & ... & 0 & N_\mathbf{v}^9 \end{bmatrix} \\
\widetilde{\mathbf{N}}_\mathbf{v} &= \begin{bmatrix} N_\mathbf{v}^1 & N_\mathbf{v}^1 & N_\mathbf{v}^2 & N_\mathbf{v}^2 & ... & N_\mathbf{v}^9 & N_\mathbf{v}^9 \end{bmatrix} \\
\mathbf{N}_P &= \begin{bmatrix} N_P^1 & N_P^2 & ... & N_P^5 \end{bmatrix} \\
\mathbf{B} &= \begin{bmatrix} \partial_x N_\mathbf{v}^1 & 0 & \partial_x N_\mathbf{v}^2 & 0 & ... & \partial_x N_\mathbf{v}^9 & 0 \\ 0 & \partial_y N_\mathbf{v}^1 & 0 & \partial_y N_\mathbf{v}^2 & ... & 0 & \partial_y N_\mathbf{v}^9 \\ \partial_y N_\mathbf{v}^1 & \partial_x N_\mathbf{v}^1 & \partial_y N_\mathbf{v}^2 & \partial_x N_\mathbf{v}^2 & ... & \partial_y N_\mathbf{v}^9 & \partial_x N_\mathbf{v}^9 \end{bmatrix} \\
\mathbf{G}_\mathbf{v} &= \begin{bmatrix} \partial_x N_\mathbf{v}^1 & \partial_y N_\mathbf{v}^1 & \partial_x N_\mathbf{v}^2 & \partial_y N_\mathbf{v}^2 & ... & \partial_x N_\mathbf{v}^9 & \partial_y N_\mathbf{v}^9 \end{bmatrix}
\end{aligned}
\tag{B.5}
$$

and,

$$
\mathbf{D}_k = \mu_k^{eff} \begin{bmatrix} 4/3 & -2/3 & 0 \\ -2/3 & 4/3 & 0 \\ 0 & 0 & 1 \end{bmatrix}
\tag{B.6}
$$

B2 Stress Recovery

Since our formulation is fully visco-elasto-platic, there is a need to obtain secondary variables such as stresses or strain rates from primary variables solutions (i.e velocity). However, because of the used element shape function, $N_{\mathbf{v}}$ (see Appendix B1), first spatial derivatives of velocities do not possess inter-element continuity, resulting in a discontinuous representation of fluxes. On the other hand, the temporal evolution of stresses/strain-rates need to be accurately tracked with time if elastic stresses are taken into account.

We combine proper flux correction techniques and moving set of particles in order to keep track of continuous stress fields. Details on both, the flux correction scheme and how to compute stresses at the particles are given below.

B2.1 Global Smoothing

Among the many existing flux correction schemes (local/global smoothing, superconvergent patch recovery, etc.), global smoothing (Hinton & Campbell, 1974) perhaps represents the most natural approach of FEM to obtain continuous flux descriptions all over the domain. The idea behind this method is to recover a finite element smoothed flux solution which provides a best-fit in the least-squares sense over the domain.

In two dimensions, a continuous approximation of smoothed velocity derivatives can be given as,

$$v_x^* = \sum_a N_{\mathbf{v}}^a v_x^{a*} \qquad v_y^* = \sum_a N_{\mathbf{v}}^a v_y^{a*} \tag{B.7}$$

where v_x^{a*} and v_y^{a*} represent the unknown nodal vectors of smoothed derivatives. The minimization procedure results in the following system of linear equations to be solved v_x^{a*} and v_y^{a*},

$$\mathbf{M} \cdot \mathbf{v}_x^* = \mathbf{f}_x \qquad \mathbf{M} \cdot \mathbf{v}_y^* = \mathbf{f}_y \tag{B.8}$$

where $\mathbf{M}$ is the mass matrix, $\mathbf{M} = \int_\Omega \mathbf{N}_{\mathbf{v}}^T \mathbf{N}_{\mathbf{v}} d\Omega$, and $\mathbf{f}_x$ and $\mathbf{f}_y$ are the RHS vectors involving the unsmoothed derivatives for each direction (v_x^h and v_y^h) as,

$$\mathbf{f}_x = \int_\Omega \mathbf{N}_{\mathbf{v}}^T v_x^h d\Omega \qquad \mathbf{f}_y = \int_\Omega \mathbf{N}_{\mathbf{v}}^T v_y^h d\Omega \tag{B.9}$$

Both the mass matrix and the RHS vectors are evaluated using numerical integration. Recovering thus a finite element smoothed solution requires the solution of two linear matrix systems (Eqs. (B.8)) for the 2D case. Despite being computationally expensive in some cases, Global Smoothing represents a

robust and easy-to-implement smoothing technique that enables us to evaluate velocity derivatives all over the domain under the FEM framework.

B2.2 Computing stresses at particles

Deviatoric stresses are updated at the particles using Eq. (48), which we recover here,

$$\begin{aligned} \boldsymbol{\tau}_k &= 2\mu_k^{eff}\dot{\boldsymbol{\varepsilon}}_k^{'} + \chi_k^{\boldsymbol{\tau}}\hat{\boldsymbol{\tau}}_k^0 \\ \Delta P_{k,j} + \omega_{k,j}\sigma\Theta_{k,j} &= -\xi_{k,j}^{eff}\left(\omega_k\phi_k\nabla\cdot\mathbf{v}_k - \omega_j\phi_j\nabla\cdot\mathbf{v}_j\right) + \chi_{k,j}^{P}\Delta P_{k,j}^0 \end{aligned} \tag{B.10}$$

Effective viscosities, μ_k^{eff} and $\xi_{k,j}^{eff}$, elastic parameters, $\chi_k^{\boldsymbol{\tau}}$ and $\chi_{k,j}^{P}$, deviatoric strain-rates $\dot{\boldsymbol{\varepsilon}}_k^{'}$, and volumetric strain rates $\nabla\cdot\mathbf{v}_k$ are transferred from the Eulerian grid to the particles using the interpolation scheme in (Oliveira et al., 2016). $\hat{\boldsymbol{\tau}}_k^0$ is the rotated and advected deviatoric stress tensor from the previous time step, and $\Delta P_{k,j}^0$ is the advected pressure difference (including surface tension effects). The advection of both stresses and pressure differences is solved using the RK4 scheme, and the deviatoric stress rotation via the following relations,

$$\begin{aligned} \tau_{x'x'} &= \tau_{xx}\cos^2\theta + \tau_{yy}\sin^2\theta + \tau_{xy}\sin 2\theta \\ \tau_{y'y'} &= \tau_{xx}\sin^2\theta + \tau_{yy}\cos^2\theta - \tau_{xy}\sin 2\theta \\ \tau_{x'y'} &= \frac{1}{2}\left(\tau_{yy} - \tau_{xx}\right)\sin 2\theta + \tau_{xy}\cos 2\theta \end{aligned} \tag{B.11}$$

we follow the convention that stress rotation angles $\theta = w\Delta t$ are positive for counter-clockwise rotations, x-axis is oriented from left to right, and the y-axis from bottom to top. w is the vorticity computed as $w = \frac{1}{2}\left(\frac{\partial v_x}{\partial y} - \frac{\partial v_y}{\partial x}\right)$, and it is obtained through the procedure described in the previous section. Note that the rotation definition in (B.11) is only valid for small angles of rotation.

APPENDIX C: VALIDATION OF THE NUMERICAL CODE

C1 3 Body rotation problem

The three body rotation transport problem is solved for pure advection and advection+diffusion. This benchmark tests the accuracy of both the advection scheme and the particle-to-node-to-particle interpolation strategy. For further details on the initial settings and problem description, the author is referred to Oliveira et al. (2016).

Figure A2 shows the results obtained after 3 revolutions for the pure advection problem (first row), and 1 revolution for the advection+diffusion (second row). As expected, we exactly recover the shape of the three bodies in the first case, whereas in the second our method shows stability and good agreement

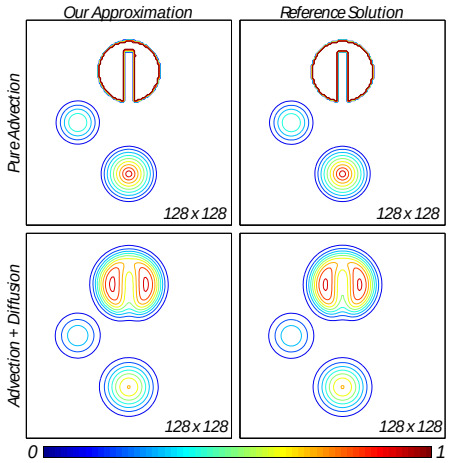

Figure A2. Contour plots for the three body rotation problem. Advection (3 revolutions) and Advection + Diffusion (1 revolution) problems (by rows).

when compared with the reference solution. As shown in Oliveira et al. (2016), our interpolation scheme is proven to handle sharp gradients and local heterogeneities effectively.

C2 Stokes flow with analytical solution

We consider a two-dimensional incompressible problem in the square domain $\Omega = [0,1] \times [0,1]$ with analytical solution (Donea & Huerta, 2003). The problem consists of determining the velocity and pressure fields such that,

$$\begin{aligned} \nabla P - \mu \nabla^2 \mathbf{v} &= \mathbf{b} \quad \text{in } \Omega \\ \nabla \cdot \mathbf{v} &= 0 \quad \text{in } \Omega \\ \mathbf{v} &= 0 \quad \text{on } \Gamma \end{aligned} \tag{C.1}$$

where the viscosity $\mu = 1$ and the components of the body force $\mathbf{b}$ are prescribed as,

$$\begin{aligned} b_x = &(12 - 24y)\, x^4 + (-24 + 48y)\, x^3 + \left(-48y + 72y^2 - 48y^3 + 12\right) x^2 \\ &+ \left(-2 + 24y - 72y^2 + 48y^3\right) x + 1 - 4y + 12y^2 - 8y^3 \\ b_y = &\left(8 - 48y + 48y^2\right) x^3 + \left(-12 + 72y - 72y^2\right) x^2 \\ &+ \left(4 - 24y + 48y^2 - 48y^3 + 24y^4\right) x - 12y^2 + 24y^3 - 12y^4 \end{aligned} \tag{C.2}$$

The exact solution for this problem reads,

$$
\begin{aligned}
v_x =& x^2 \left(1-x\right)^2 \left(2y - 6y^2 + 4y^3\right) \\
v_y =& -y^2 \left(1-y\right)^2 \left(2x - 6x^2 + 4x^3\right) \\
P =& x\left(1-x\right)
\end{aligned}
\tag{C.3}
$$

In order to test our multiphase mechanical solver we adapt the problem above and rewrite the equations in (C.1) for a two-phase problem as,

$$
\begin{aligned}
\nabla\phi P_1 - \nabla\cdot\phi\boldsymbol{\tau}_1 &= \phi\mathbf{b} \\
+c_{1,2}\Delta\mathbf{v}_{1,2} + P_\omega\nabla\phi &\quad \text{in } \Omega \\
\nabla\left(1-\phi\right)P_2 - \nabla\cdot\left(1-\phi\right)\boldsymbol{\tau}_2 &= \left(1-\phi\right)\mathbf{b} \\
+c_{2,1}\Delta\mathbf{v}_{2,1} + P_\omega\nabla\left(1-\phi\right) &\quad \text{in } \Omega \\
\nabla\cdot\phi\mathbf{v}_1 + \nabla\cdot\left(1-\phi\right)\mathbf{v}_2 = 0 &\quad \text{in } \Omega \\
P_2 - P_1 = \phi\omega\nabla\cdot\mathbf{v}_1 - \left(1-\phi\right)\left(1-\omega\right)\nabla\cdot\mathbf{v}_2 &\quad \text{in } \Omega \\
\mathbf{v}_1 = 0 &\quad \text{on } \Gamma \\
\mathbf{v}_2 = 0 &\quad \text{on } \Gamma
\end{aligned}
\tag{C.4}
$$

where $\omega = \phi$ since we assume same viscosities for both phases. This benchmark consists on solving Eqs. (C.4) for different values of ϕ. First, we impose uniform ϕ (uniform porosity,$\nabla\phi = \nabla\left(1-\phi\right) = 0$). As for the second case, we impose a non-zero phase abundance gradient in a similar two-phase problem (constant gradient in porosity). Results for these two cases are shown in Figs. A3 and A4.

As expected, we recover the analytical solution with appropriate convergence rates for the first problem (A and B in Fig. A3 and blue line in A4). However, the results for the second case differ from the predicted ones. The reason behind this difference resides in the interaction term employed to approximate the shear stresses at the interface. In order to recover the analytical solution, the interaction term $c_{1,2}\Delta\mathbf{v}c_{1,2}$ should cancel out the stress jump at the interface $\boldsymbol{\tau_1}\cdot\nabla\phi$, and similarly for the second phase. Whereas for the first problem this is fulfilled since $\nabla\phi = 0$, convergence of the numerical solution can not be expected in the second case, since $c_{1,2}\Delta\mathbf{v}_{1,2} \neq \boldsymbol{\tau_1}\cdot\nabla\phi$. Consequently, some little error occur in both velocity A3-C and pressure fields A3-D. However, if we modify the body source in (C.2) to take into account the term $\boldsymbol{\tau}\cdot\nabla\phi$ in Eqs. (C.4) (here only the correction for the first phase is shown),

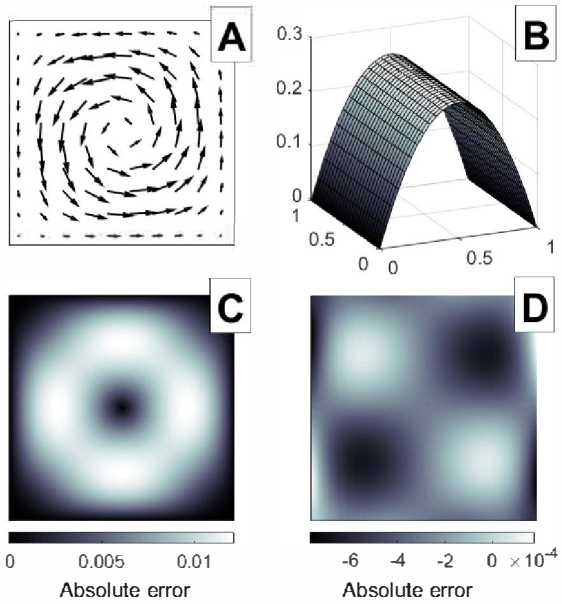

Figure A3. Velocity (A and C) and pressure (B and D) results for uniform (A and B) and non-uniform (C and D) porosity problems. Top panels (A and B) refer to absolute values obtained with 25×25 Q2-(Q1+Q0) elements for the uniform problem, where the discontinuous pressure field has been averaged over the nodes. Lower panels (C and D) show absolute errors (relative to the analytical solution) of the non-uniform model with 25×25 Q2-(Q1+Q0) elements for both, velocity module and pressure fields.

$$
\begin{aligned}
\phi b_x =& \phi\left(12-24y\right)x^4+\phi\left(-24+48y\right)x^3+\phi\left(-48y+72y^2-48y^3+12\right)x^2\\
&+\phi\left(-2+24y-72y^2+48y^3\right)x+\phi\left(1-4y+12y^2-8y^3\right)\\
&-2\frac{\partial\phi}{\partial x}(x^2(2x-2)(4y^3-6y^2+2y)+2x(x-1)^2(4y^3-6y^2+2y))\\
&-\frac{\partial\phi}{\partial y}(x^2(x-1)^2(12y^2-12y+2)-y^2(y-1)^2(12x^2-12x+2))\\
\phi b_y =& \phi\left(8-48y+48y^2\right)x^3+\phi\left(-12+72y-72y^2\right)x^2\\
&+\phi\left(4-24y+48y^2-48y^3+24y^4\right)x-\phi\left(12y^2+24y^3-12y^4\right)\\
&-\frac{\partial\phi}{\partial x}(x^2(x-1)^2(12y^2-12y+2)-y^2(y-1)^2(12x^2-12x+2))\\
&-2\frac{\partial\phi}{\partial y}(-y^2(2y-2)(4x^3-6x^2+2x)-2y(y-1)^2(4x^3-6x^2+2x))
\end{aligned}
\tag{C.5}
$$

we recover both the analytical solution and the expected convergence rates for any possible distribution of phases (Figs. A3-A-B and A4(*)). In any case the results depicted in Figs. A3 and A4 show oscillation-free results, which are in good agreement with the analytical and theoretical predictions.

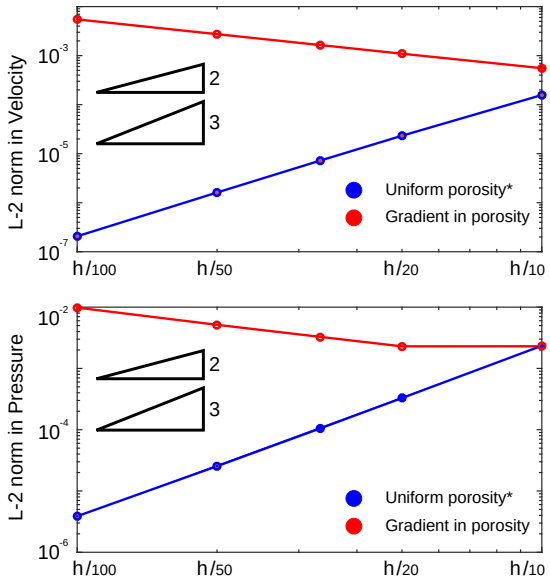

Figure A4. Velocity (top panel) and pressure (lower panel) spatial convergence tests for uniform (blue) and non uniform (red) porosity two-phase problems. The errors are shown in L-2 norm relative to the analytical solution for different element sizes $h = [1/10, 1/20, 1/30, 1/50, 1/100]$. We get high-order in both velocity and pressure fields for the uniform problem, whereas the desired convergency is not reached for the non-uniform case. (*)When the body source is corrected with the interfacial stress term, the results overlap with the uniform porosity case and high-order is obtained.

C3 Rayleigh-Taylor instability

We run a two-layer isothermal compositional Rayleigh-Taylor instability in a box with aspect radio λ (Keken et al., 1997). This benchmark tests the accuracy of our advective scheme, the mechanical model, and the way viscosity jumps are handled by our code. The initial setup is a box with depth $H = 1$, a buoyant layer of thickness 0.2, an aspect radio of $\lambda = 0.9142$, a density contrast of $\Delta\rho = 1$, different rheology ratios $\mu_a/\mu_b = \{1, 10, 100\}$, and an initial deflection of the interface $a = 0.02 \sin \pi/\lambda$.

The results are given in Fig. A5, where the evolution of root-mean-square velocity and the relative entrainment of the light material as a function of time are shown for the three viscosity contrasts. Velocity peaks compare well in value and timing with the methods compared in Keken et al. (1997). Snapshots of the evolution of the isoviscous Rayleigh-Taylor instability are also shown at times $t = 500, 1000, 1500s$. The reader is referred to Keken et al. (1997), for a comparison of these results.

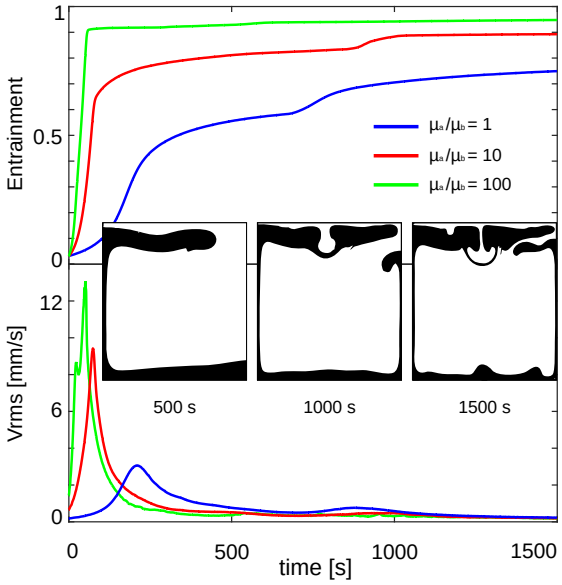

Figure A5. Evolutions of the entrainment of the light material (top) and evolution of the rms velocity for the three viscosity contrasts with time. In the middle, results for the isoviscous case are shown at $t = 500, 1000, 1500s$

C4 Two-phase compaction

We run the classic two-phase compaction problem, where the fluid (f) is allowed to flow across the solid (s) due to the density difference between dynamic phases (McKenzie, 1984). The system is assumed to be one-dimensional, with an impermeable bottom boundary, at $y = 0$, and a stress-free upper boundary at $y = h$. In the case of $\mu_s \gg \mu_f$ and constant uniform phase distribution ($\phi_f = \phi_0$ and $\phi_s = 1 - \phi_0$), the compaction problem has an analytical solution for $t = 0$, which reads

$$\begin{aligned} \mathbf{v}_f &= v_0 \left(1 - \phi_0\right) \left(1 - e^{-y/\delta_c}\right) \\ \mathbf{v}_s &= -v_0 \phi_0 \left(1 - e^{-y/\delta_c}\right) \\ \text{where } v_0 &= \frac{\mathrm{k}_{\phi_0}}{\mu_f} \frac{1 - \phi_0}{\phi_0} \left(\rho_s - \rho_f\right) g \\ \delta_c &= \left(4/3 \left(1 - \phi_0\right) \mu_s \frac{\mathrm{k}_{\phi_0}}{\mu_f}\right)^{0.5} \end{aligned} \tag{C.6}$$

Figure A6 depicts both fluid and solid velocities with depth for a given initial configuration. Our mechanical formulation exactly reproduces the analytical solution.

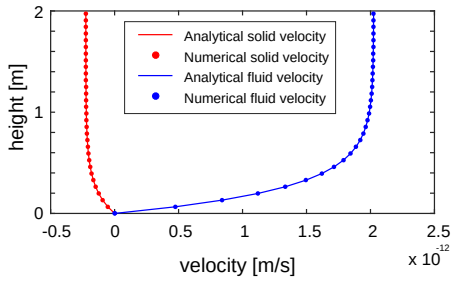

Figure A6. 1-D fluid-solid compaction problem. Fluid (blue) and solid (red) velocities as a function of depth above an impermeable layer at $y = 0$. Boundary condition at $y = 2$ is that both fluid and solid are stress free. As for the material properties, $\mu_f = 10^5$, $\mu_s = 10^{15}$, $\xi_s = 10^{15}$, $\rho_f = 2800$, $\rho_s = 3300$, $\mathrm{k}_{\phi_0} = 5 \cdot 10^{-10}\phi_0^2$, $g = 10$ and $\phi_0 = 0.1$.

C5 Locking and extended Taylor-Hood elements

Finite elements behave poorly when nearly incompressible materials are modeled. It has been shown that under some circumstances finite elements produce stiffer results than expected (Bower, 2009). This problem is commonly referred as "locking". Here, we show how our mixed formulation combined with the extended Taylor-Hood hybrid element overcome the effects of locking. We consider a long hollow cylinder with internal radius $a = 1$ and external radius $b = 4$. As for material properties, we have Poisson's coefficient $\nu = 0.495$ (nearly incompressible) and shear modulus $G = 1$. The cylinder is loaded by an internal pressure $p_a = 1$.

Figure A7 demonstrates how our mixed formulation combined with the extended Taylor-Hood hybrid element prevents locking.

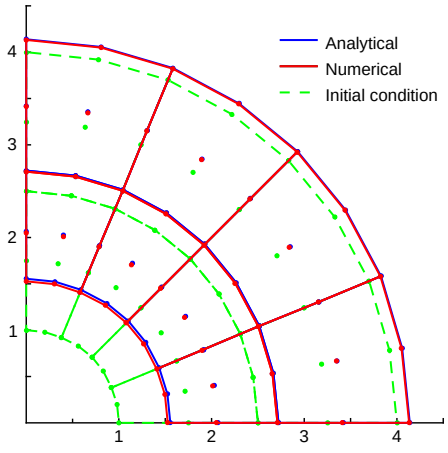

Figure A7. Comparison of the numerical solution (red) to the analytical (blue) solution of the loaded cylinder. The initial condition (dashed green line) is shown for reference and the solution is represented with the finite element mesh, where the circles are the nodes.

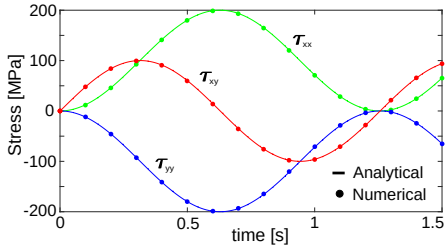

Figure A8. Unit square under simple shear at a rate of 5 s^{-1}, and shear modulus $G = 100$ MPa.

C6 Visco-elasto-plastic Rheology

C6.1 Simple shear to large strain

We verify the correct implementation of the Jaumann stress derivative for large deformations. We compute a simple purely elastic shear stress problem, and allow the strains to become quite large. Under a constant strain rate $\dot{\varepsilon}$, the stresses should evolve according to $\tau_{xy} = G \sin(\dot{\varepsilon} t)$, $\tau_{xx} = -\tau_{yy} = G(1 - \cos(\dot{\varepsilon} t))$. The results and the material properties are shown in Fig. A8. The harmonic behavior corresponds to the rigid body rotation for large deformations. Numerical results overlap with the analytical predictions, which demonstrate the effectiveness of our Jaumann derivative implemenation to compute stress advection and rotations.

C6.2 Visco-elasto-plastic evolution under pure shear

In an homogeneous 2-D incompressible pure shear problem with a constant strain rate, $\dot{\varepsilon}^{'}$, the deviatoric stresses should evolve according to the equation $\tau_{II} = 2\mu\dot{\varepsilon}^{'}\left(1 - e^{-Gt/\mu}\right)$. If plasticity is taking into account, the deviatoric stresses should be limited to the failure criteria $\tau_{II} \leq \tau_y$. The model dimensions and boundary conditions change in every time step in order to ensure a constant strain rate over time (Gerya & Yuen, 2007), and as for the material properties $G = 10^{10}$ Pa, $\mu = 10^{22}$ Pa, and $\tau_y = 100$ MPa. We run two different scenarios with visco-elastic and visvo-elasto-plastic rheologies. Figure A9 shows exact agreement between our numerical results and the analytically predicted stress curve for both the visco-elastic (blue) and visco-elasto-plastic (red) scenarios.

C6.3 Visco-elasto-plastic evolution under volumetric expansion

Analogously, we run a 2-D two-phase volumetric compaction model, where we impose a constant volumetric strain rate $\dot{\nu}$. In this case, the compaction pressure should evolve according to the relation $P_c = (1 - \phi)\,\dot{\nu}\left(1 - e^{-Kt/\xi}\right)$. Again, if plastic failure is taken into account, P_c should be limited by the failure criteria $P_c \geq P_y$ ($P_y = 30$ MPa for this example).

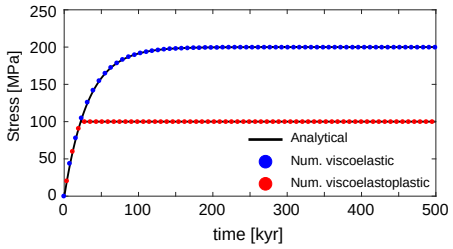

Figure A9. Shear stress evolution in time for the pure shear deformation. Black lines correspond to analytical solutions whereas the circles represent the numerical solutions for both the visco-elastic (blue) and the visco-elasto-plastic rheologies (red).

The numerical results in A10 for both, visco-elastic (blue) and visco-elasto-plastic (red) rheologies depict good agreement with the analytical predictions.

C6.4 Visco-elasto-plastic shear bands

We test the ability of our code to initialize shear bands at characteristic angles when plastic shear failure occurs under pure shear extension or compression. The homogenous 2-D model setup includes a circular weak inclusion (10 m radius) in the middle of our 2000 m wide and 1000 m high rectangular domain and a background strain rate of $\dot{\varepsilon}_{BG} = 10^{-14}$ s^{-1}. As for the material properties, the viscosity is $\mu = 10^{23}$ Pa s, elastic modulus $G = 10^{10}$ Pa, cohesion $C = 5 \cdot 10^{6}$ Pa, and the friction angle is set to $\varphi = 30°$. This set up should form shear bands with an angle around 60° relative to the horizontal axis under extension, whereas angles around 30° should be expected under compression. The shape and direction of these shear bands are dependent on the numerical resolution, effects of rheology, type of element, and iteration strategy (Kaus, 2010). We employ 90x45 Q2-(Q1+Q0) Taylor Hood element mesh, Global Smoothing stress recovery technique and a Picard iteration scheme to solve both the extensional and compression problems. Figure A11 demonstrates the ability of our code to form the shear bands with the characteristic angles under both extension and compression.

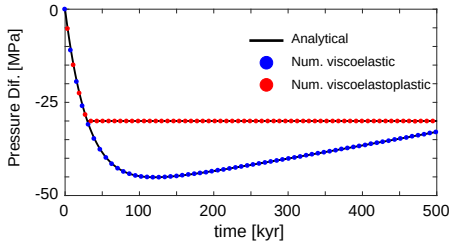

Figure A10. Compaction pressure evolution in time under constant volumetric compaction. Black lines correspond to analytical solutions whereas the circles represent the numerical solutions for both the viscoelastic (blue) and the viscoelastic rheologies (red).

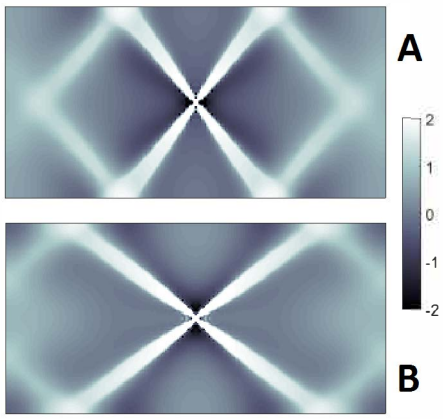

Figure A11. Results of the pure shear extension extension (panel A) and compaction (panel B). Displayed are differential strain rates relative to the background strain rate $\dot{\varepsilon}_{BG} = 10^{-14}$ s^{-1} in logarithmic scale. Both results show good agreement with the expected characteristic angles.

This paper has been produced using the Blackwell Scientific Publications GJI LaTeX2e class file.